Université de Neuchâtel
Institut de Microtechnique

Reciprocal interferometers for fiber optic Faraday current sensors

Thèse

Présentée à la Faculté des sciences
pour obtenir le grade de docteur ès sciences

par

Guido Frosio

IMPRIMATUR POUR LA THÈSE

Reciprocal Interferometers for Fiber Optic Faraday Current Sensors

de Monsieur Guido Frosio

UNIVERSITÉ DE NEUCHÂTEL

FACULTÉ DES SCIENCES

La Faculté des sciences de l'Université de Neuchâtel sur le rapport des membres du jury,

Messieurs R. Dändliker, N. de Rooij, Ph. Robert (EPF-Lausanne) et H. Brändle (Baden)

autorise l'impression de la présente thèse.

Neuchâtel, le 15 juin 1992

Le doyen:

A. Robert

ABSTRACT

In the present work, two types of reciprocal interferometers for the detection of the Faraday effect are theoretically and experimentally investigated and compared. The first one is a Sagnac interferometer and the second one is a reciprocal reflection interferometer. Special emphasis is given to the effects of non-ideal behavior of the different polarization sensitive elements.

An all-fiber Sagnac current sensor has been realized and successfully tested. Fiber optic elements, such as all-fiber quarterwave loops, all-fiber polarizers, polarization maintaining fiber couplers and pigtailed laser sources, have been used. In a first experiment the sensing coil had the form of a helix surrounding the electrical conductor. Another all-fiber Sagnac current sensor, based on a commercial fiber optic gyroscope, has been realized and tested. A 20 turn fiber coil with a diameter of 345 mm was used. The ultra-low birefringence fiber of 80 µm diameter was mechanically twisted at the rate of 10 turns/m. Perfect linearity between the detected Faraday phase shift and the 75 Hz ac current was measured from 10 A to 800 A. The detected phase noise amounts to about 10 µrad/$\sqrt{Hz}$, which is equivalent to a detected current noise of 0.1 A/$\sqrt{Hz}$. Very good stability and temperature behavior have been obtained (relative current error smaller than 2 ‰ between 20 °C and 80 °C). Some problems remain at low temperatures ($\leq 0°$ C) due to technological problems in the realization of the sensing coil. This "gyro-current sensor" shows how the development of fiber optic current sensors can benefit from the well established fiber optic gyroscope technology.

The reflection interferometer looks like one half of a Sagnac interferometer. It uses two co-propagating orthogonal modes which are reflected at the end of the fiber sensing coil, which is connected to the ground level by a polarization maintaining hi-bi fiber. Between the sensing coil and the hi-bi fiber a quarterwave loop transforms the two orthogonal linear polarizations into orthogonal circular polarizations and vice-versa. The combination of the hi-bi fiber, the quarterwave loop, and the mirror results in a perfectly balanced reciprocal interferometer. After a total round trip in the interferometer the only phase shift between the two polarizations is caused by the Faraday effect. The reflected light is detected at the output arm of a fiber coupler. The effects of polarization cross-coupling due to non-ideal elements are eliminated by using a low coherence source. Non-reciprocal phase modulation is necessary to get optimum detection of the Faraday phase shift. This non-reciprocal modulation is performed by an all-fiber birefringence modulator. The reflection interferometer using non-reciprocal phase modulation has been realized and succesfully tested. The sensing element was a piece of straight fiber of ultra-low birefringence type. The magnetic field was produced by a 100 turn solenoid. Perfect linearity between the detected Faraday phase shift and the 75 Hz ac current was measured from 0 A to 40 A. The detected current noise amounts to about 0.015 A/$\sqrt{Hz}$.

From the comparison between the Sagnac and the reflection configuration it appears that, for similar performance, the second needs less fiber optic elements and half the number of splices. This is an important advantage for the industrial production of current sensors. The modulated detector signals are identical for the Sagnac and the reflection configuration. This permits to use the same electronic signal processing for both configurations.

TABLE OF CONTENTS

1. INTRODUCTION 1

2. THE FARADAY EFFECT IN SINGLE MODE FIBERS 3
   2.1. The Faraday effect in a non-birefringent fiber 3
   2.2. Non-reciprocal behavior of the Faraday effect 4
      2.2.1. Linear basis representation 5
      2.2.2. Circular basis representation 5
   2.3 Jones matrices of different fiber configurations 5
      2.3.1. Reciprocal properties of the Jones matrices 6
      2.3.2. Ideal fiber 7
      2.3.3. Twisted fiber 7
      2.3.4. Spun fiber 10
      2.3.5. Helical fiber 11

3. DETECTION OF THE FARADAY EFFECT 13
   3.1. Heterodyne detection of the Faraday effect with helical coil 14
      3.1.1. Realization and birefringence measurement of the helical coil 14
      3.1.2. Heterodyne detection of the Faraday effect 15
      3.1.3. Optical set-up and signal processing 18
      3.1.4. Experimental results 19
   3.2. Reciprocal interferometers for Faraday effect detection 20
      3.2.1. The Sagnac interferometer for Faraday effect detection 20
      3.2.2. The reciprocal reflection interferometer for Faraday effect detection 21

4. THE SAGNAC INTERFEROMETER WITH FARADAY EFFECT 24
   4.1. Jones matrices and detected intensity 24
      4.1.1. Perpendicular and parallel orientation of the quarterwave loops 26
      4.1.2. Ideal fiber coil 30
      4.1.3. Coil with mechanically twisted fiber 30
      4.1.4. Coil with spun or helical fiber 31
   4.2. Faraday phase recovery 31
      4.2.1. Ideal fiber coil 32
      4.2.2. Twisted and spun fiber 32

4.3. Source coherence effects 33
4.4. Temperature effects due to the sensing coil 34
4.5. Effects of non-ideal quarterwave loops 35
4.5.1. Detected Faraday effect 36
4.5.2. Temperature effects 37
4.5.3. Misalignment effects 39
4.6. All-Fiber Sagnac current sensor 42
4.6.1. Summary 42
4.6.2. Principles and signal processing 42
4.6.3. Effects of non-ideal elements 44
4.6.4. Noise limitations 46
4.6.5. Experimental results 48
4.6.6. Conclusions 51
4.7. All-fiber Sagnac current sensor based on a commercial fiber optic gyroscope 52
4.7.1. Summary 52
4.7.2. Experimental set-up and signal processing 52
4.7.3. Measurement of the Faraday effect 53
4.7.4. Measurement of the influence of the temperature 54
4.7.5. Influence of the alignment between the hi-bi fibers and the quarterwave loops 55

5. THE RECIPROCAL REFLECTION INTERFEROMETER WITH FARADAY EFFECT 57
5.1. Detected intensity and effects of the coherence of the source for general fiber configuration 57
5.1.1. Detected intensity 58
5.1.2. Influence of the source coherence 60
5.2. Detected intensity for different fiber configurations 63
5.2.1. Ideal fiber coil 63
5.2.2. Twisted and spun fiber 64
5.2.3. Effects of non-ideal quarterwave loop 65
5.2.4. Effects of non-ideal alignment of the quarterwave loop 66
5.3. The reflection interferometer with non-reciprocal internal phase modulation 66
5.3.1. Detected intensity for different fiber configurations 68
5.3.2. Faraday phase recovery 69
5.4. Temperature effects due to the sensing coil 71
5.5. Effects of non-ideal quarterwave loop 72
5.5.1. Retardation error effects 72
5.5.2. Temperature effects 73
5.5.3. Misalignment effects 75
5.6. Experimental investigations of the unmodulated reflection interferometer 75
5.6.1. High coherence source 76
5.6.2. Low coherence source 80

5.7. Experimental investigations of the non-reciprocally phase modulated reflection interferometer 84
5.7.1. Experimental set-up and signal processing 84
5.7.2. Non-ideal elements and noise limitations 85
5.7.3. Faraday effect measurement 86
5.7.4. Effects of non-ideal quarterwave loop 87
5.7.5. Effects of the polarization cross-coupling 88
5.7.6. Effects of the temperature 88
5.7.7. Conclusions 88

6. COMPARISON OF THE SAGNAC INTERFEROMETER AND THE RECIPROCAL REFLECTION INTERFEROMETER 89
6.1. Principal characteristics 89
6.2. Effects of non-ideal elements and temperature 90

7. CONCLUSIONS 92

ACKNOWLEDGMENTS 95

REFERENCES 96

1. INTRODUCTION

All-fiber current sensors, based on the magneto-optic Faraday effect (rotation of the polarization plane by a longitudinal magnetic field), have been proposed as an alternative to conventional transformers in measurement, fault diagnostic and protection on high voltage lines. The main advantages are: insensitivity to electromagnetic interference, higher dynamic range, wide bandwidth and reduction of insulation problems. Moreover, this type of sensors does not require a power supply for HV-installed parts, are lightweight and well suited for harsh environments.

For years many research groups have been involved in the development of the all-fiber Faraday current sensors. These sensors are today in a research and early development stage. Applications of these sensors have so far been limited to laboratory instruments and plasma current research. Field trials have been carried out only under very carefully controlled conditions.

The major difficulty is bend-induced and intrinsic birefringence in the fiber which is wound around the electrical conductor. This birefringence changes the polarization state and quenches the Faraday effect. Early laboratory types of fiber optic current sensors were made of conventional telecommunication quality single-mode fibers. Linear birefringence in this fiber can be suppressed by twisting the fiber to introduce circular birefringence. Low-birefringence type fibers have been developed, however, the so called spun fiber still suffers from stress induced birefringence, caused by coiling and vibrations. A new type of fibers exhibiting high circular birefringence has been recently developed. However, this fiber, called hi-bi spun fiber, has to be improved, specially for its circular polarization maintaining capability and its thermal sensitivity. Low-birefringence fibers which are subjected to a mechanically twist maintained by the cladding have been developed recently, but their properties have to be improved further. An alternative approach is to remove the bend-induced birefringence by annealing. Coils are wound in the desired form, heated to about 900 °C for approximately 24 hours, and then cooled slowly. With this technique the linear birefringence is nearly eliminated.

The Faraday effect can be detected using polarimetric or interferometric configurations. Basically, the polarimetric method consists of measuring the Faraday rotation by using a polarizing beam splitter at the fiber output. Two balanced signals are obtained and electronically processed in order to obtain the Faraday rotation. Compensation of reciprocal polarimetric effects is obtained by using a sensing fiber coil with a mirror on the far end and detecting the return wave at the input end. In this case the non-reciprocal Faraday effect is doubled and reciprocal birefringence effects are compensated for the most part.

The non-reciprocal Faraday phase shift, obtained between two orthogonal circular polarizations propagating in the same direction or between two counter propagating circular polarizations with the same handedness, can in principle be determined by a variety of interferometric configurations. When both circular polarizations have the same optical frequency, this is referred to as homodyne detection. In this case the Faraday phase shift can be recovered by using classical phase modulation techniques. Heterodyne detection, where the two circular polarizations have different optical frequencies, provides directly the Faraday phase shift,

regardless of fluctuations of the optical power, launching efficiency and detector responsivity. The Faraday signal, which modulates the phase of the carrier oscillating at the beat frequency, is obtained from the detected optical signal using a FM discriminator or, if a reference signal is available, a phasemeter. Reciprocal interferometers, like the Sagnac interferometer and the reflection interferometer, permit to cancel to a large extent the unwanted reciprocal effects due to residual birefringence in the fiber, whereas the non-reciprocal Faraday effect remains.

In the present work, two types of reciprocal interferometers for the detection of the Faraday effect are theoretically and experimentally investigated and compared. The first one is a Sagnac interferometer and the second one is a reciprocal reflection interferometer.

The fiber optic Sagnac interferometer is well known for its application as a gyroscope. It is only sensitive to non-reciprocal effects, such as the Sagnac effect or the Faraday effect. Therefore it is a good candidate for current sensing applications. An all-fiber Sagnac current sensor has been realized and successfully tested. Fiber optic elements, such as all-fiber quarterwave loops, all-fiber polarizers, polarization maintaining fiber couplers and pigtailed laser sources, have been used. In a first experiment the sensing coil had the form of a helix around the electrical conductor. This helical coil had been used previously in a fiber optic current sensor working in transmission and using heterodyne detection. The geometrical torsion of the helix provides an elegant way to compensate the perturbing effects of the bend-induced linear birefringence. Another all-fiber Sagnac current sensor, based on a commercial fiber optic gyroscope, has been realized and tested. This "gyro-current sensor" shows how the development of fiber optic current sensors can benefit from the well established fiber optic gyroscope technology.

To the best of our knowledge, it is for the first time in this work that a truly reciprocal reflection interferometer is reported. This interferometer looks like one half of a Sagnac interferometer. The reflection interferometer uses two co-propagating orthogonal modes which are reflected at the end of the fiber sensing coil, rather than two counter-propagating modes of the same polarization, as in the case of the Sagnac interferometer. The sensing coil is connected to the ground level by a polarization maintaining hi-bi fiber. Between the sensing coil and the hi-bi fiber a quarterwave loop transforms the two orthogonal linear polarizations into orthogonal circular polarizations and vice-versa. The combination of the hi-bi fiber, the quarterwave loop and the mirror results in a perfectly balanced reciprocal interferometer. After a total round trip in the interferometer the only phase shift between the two polarizations is caused by the Faraday effect. The reflected light is detected at the output arm of a fiber coupler. The effects of polarization cross-coupling due to non-ideal elements, such as the sensing coil, the quarterwave loop, the hi-bi fiber, etc, are eliminated by using a low coherence source. Non-reciprocal phase modulation is necessary to get optimum detection of the Faraday phase shift. This non-reciprocal modulation is performed by an all-fiber birefringence modulator. To be independent of the polarization properties of the coupler, the two reflected orthogonal modes are made to interfere before this coupler. This is achieved by inserting a linear polarizer between the coupler and the modulator.

From the comparison between the Sagnac and the reflection configuration it appears that, for similar performance, the second needs less fiber optic elements and half the number of splices. This is an important advantage for the industrial production of current sensors. The modulated detector signals are identical for the Sagnac and the reflection configuration. This permits to use the same electronic signal processing for both configurations.

2. THE FARADAY EFFECT IN SINGLE MODE FIBERS

2.1. The Faraday effect in a non-birefringent fiber

When linearly polarized light passes trough a transparent material of length L located in a magnetic field H the direction of the linear polarization is rotated by the angle

$$\varphi_F = V \int_L H_z \, dz \ , \qquad (2.1.1)$$

via the action of the magneto-optic Faraday effect. H_z is the magnetic field component in the direction of the light beam. The Verdet constant V is determined by the magnetic properdes of the material. In diamagnetic materials V is very small but not function of the temperature, whereas in paramagnetic materials it is usually somewhat larger but always dependent on the temperature. Because of the temperature independence of the Faraday rotation, diamagnetic materials, such as silica, are more suitable for the use as sensor material in current measurement applications. The Verdet constant for diamagnetic materials varies proportionally to λ^{-2} for wavelengths $\lambda >> \lambda_0$ [Ros65], where λ_0 is the wavelength of the absorption resonance. For pure amorphous silica [Pal85] $\lambda_0 = 0.118$ µm and V = 5.54 µrad/A at $\lambda = 850$ nm. Due to the small Verdet constant of these materials, the main problem is to make the light path L long enough to obtain a sufficiently large rotation. As shown in Fig. 2.1 silica single mode optical fibers are well suited to provide a long light path. Typical values of the Verdet constant for a silica fiber are [Don88]: V ≈ 4.4 µrad/A at 633 nm, V ≈ 2.6 µrad/A at 820 nm, V ≈ 1 µrad/A at 1300 nm. In diamagnetic materials, the relaxation time constant of the Faraday effect falls in the sub-nanoseconds range [Voi08].

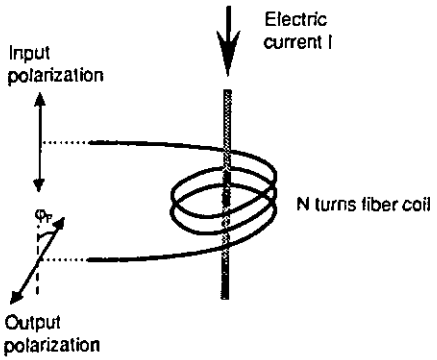

Figure 2.1 Faraday effect in a non-birefringent fiber.

In Fig. 2.1 it is assumed that the fiber exhibits no birefringence, in other words the polarization remains linear along the optical path. Applying Ampere's circuit theorem, the magnitude of the final polarization rotation becomes

$$\varphi_F = VNI, \tag{2.1.2}$$

where I is the current carried by the electrical conductor and N the number of times the fiber loops around the conductor. Equation (2.1.2) is valid regardless of the size or the shape of the loops. The conductor may thus vibrate without affecting the amount of the Faraday rotation.

2.2. Non-reciprocal behavior of the Faraday effect

The Faraday effect is nonreciprocal, this means that if the polarization rotation through an optical element is φ_F, then on passing back through the element the light polarization is rotated another φ_F in the same direction. If the effect were reciprocal, the two rotations would cancel out. The polarization state of a light wave can be represented using the well known Jones vectors [Jon41]. Usually in the literature a linear basis is chosen to describe the Jones vectors, as shown in Fig. 2.2.a. However, depending on the involved phenomena, other polarization basis can be more appropriate. For instance, as shown in Fig.2.2.b, the circular basis is well suited when dealing with polarization rotational effect [Dän92].

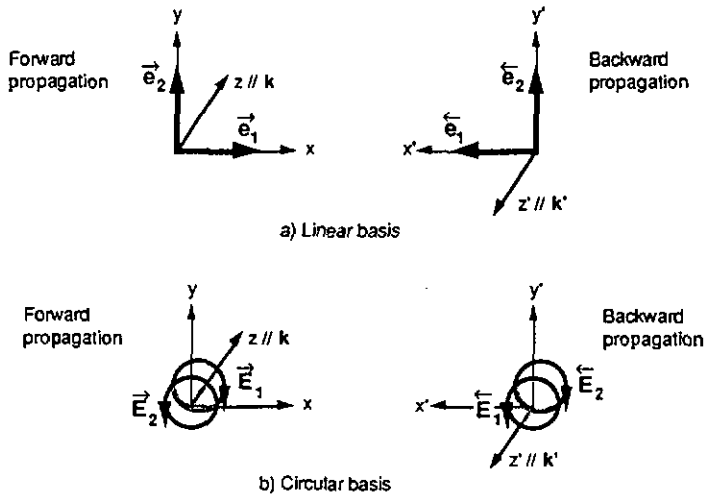

Figure 2.2 a) Linear polarization basis for forward and backward propagations, $\vec{e}_i$ and $\overleftarrow{e}_i$ = basic linear Jones vectors, $\rightarrow$ and $\leftarrow$ indicate propagation in the direction of +z and in –z, respectively. b) Circular polarization basis for forward and backward propagations, $\vec{E}_i$ and $\overleftarrow{E}_i$ = basic circular Jones vectors. k and k' are the propagation vectors for forward and backward propagation, respectively.

2.2.1. Linear basis representation

In this representation the Faraday effect is described by a rotation φ_F of the two basic linear polarizations. Due to the non-reciprocity, the rotation is φ_F for both forward and backward directions.

2.2.2. Circular basis representation

In this representation, a polarization state is represented by a linear combination of the two orthogonal basic circular polarizations. Rotational effects (or optical activity) expressed in a circular basis result in a phase shift $2\varphi_F$ between these two basic polarizations. For reciprocal rotational effects the phase shifts in the forward and backward direction will cancel (total phase amounts to zero), whereas for the Faraday effect they are cumulative (total phase shift = $4\varphi_F$).

2.3. Jones matrices of different fiber configurations

The polarization properties of an optical element can be described by its Jones Matrix [Jon41]. The Jones matrix of a piece of single mode fiber can be derived using coupled-mode theory. This approach is well suited to describe the superposition of different perturbations in single mode fibers, given by their respective dielectric tensors, which will change the polarization properties of the fiber. Jones matrices for forward and backward propagations and for different fiber configurations (twisted, spun, helical) in presence of Faraday effect have been obtained in circular basis representation [Dän92]. This representation is well adapted when dealing with the Faraday effect, which is a rotational effect. However, to describe the polarization properties of complex systems, such as interferometers for current sensors, containing elements which maintain the linear polarization (hi-bi fiber, hi-bi coupler, etc.), the linear basis representation is better suited. Therefore in the following, the Jones matrices given in the circular basis representation will be transformed into the linear one. The Jones vectors are defined as column vectors for both forward and backward propagations which is in agreement with the convention adopted by Birks *et al.* [Bir88]. This results in backward Jones matrices which are different from those obtained by Jones himself [Jon41], who defined column vectors for forward propagation but row vectors for backward propagation. Since all considered perturbations are assumed to be loss-free, the resulting Jones matrices **A** are unitary and take the form

$$\mathbf{A} = \begin{pmatrix} A & -B^* \\ B & A^* \end{pmatrix} \qquad \text{with} \qquad \mathrm{Det}(\mathbf{A}) = |A|^2 + |B|^2 = 1\,. \tag{2.3.1}$$

If **A** represents the Jones matrix in a circular polarization basis, the corresponding matrix **a** in a linear basis is given by

$$\mathbf{a} = \begin{pmatrix} a & -b^* \\ b & a^* \end{pmatrix} = \begin{pmatrix} Re\,\{A\} + i\,Im\,\{B\} & -Im\,\{A\} + i\,Re\,\{B\} \\ Im\,\{A\} + i\,Re\,\{B\} & Re\,\{A\} - i\,Im\,\{B\} \end{pmatrix}, \tag{2.3.2}$$

where $Re\,\{X\}$ and $Im\,\{X\}$ denote the real and imaginary part of X, respectively. Conversely the circular representation is obtained from the linear one by

$$A = \begin{pmatrix} Re\ \{a\}+iRe\ \{b\} & -Im\ \{b\}+iIm\ \{a\} \\ Im\ \{b\}+iIm\ \{a\} & Re\ \{a\}-iRe\ \{b\} \end{pmatrix}. \tag{2.3.3}$$

2.3.1. Reciprocal properties of the Jones matrices

For forward and backward propagation the Jones matrices are noted $\vec{A}$ and $\overleftarrow{A}$, respectively. In circular representation and if there is no Faraday effect, which is non-reciprocal, the Jones matrix in forward and backward propagation are related by [Dän92]

$$\overleftarrow{A} = \vec{A}^T, \tag{2.3.4}$$

where $\vec{A}^T$ is the transposed of $\vec{A}$. Note that $\overleftarrow{A} = \vec{A}^T$ is only true in a circular polarization basis. Equation (2.3.4) represents the condition for reciprocity. In presence of Faraday effect Eq. (2.3.4) no longer holds, however any Jones matrix may be decomposed in its reciprocal and non-reciprocal part in the following way [Ulr82]

$$\vec{A} = \vec{A}_r + \vec{A}_{nr}, \tag{2.3.5}$$

where the reciprocal part $\vec{A}_r$ satisfies Equ. (2.3.4), whereas the non-reciprocal part $\vec{A}_{nr}$ satisfies

$$\overleftarrow{A}_{nr} = -\vec{A}_{nr}^T. \tag{2.3.6}$$

$\vec{A}_r$ and $\vec{A}_{nr}$ can be obtained from $\vec{A}$ and $\overleftarrow{A}$ using

$$\vec{A}_r = \frac{1}{2}(\vec{A} + \overleftarrow{A}^T) \quad \text{and} \quad \vec{A}_{nr} = \frac{1}{2}(\vec{A} - \overleftarrow{A}^T). \tag{2.3.7}$$

$\overleftarrow{A}_r$ and $\overleftarrow{A}_{nr}$ can be obtained from (2.3.7) using Eqs. (2.3.4) and (2.3.6). In linear polarization basis, using Eqs. (2.3.2) and (2.3.3), the reciprocity condition given by Eq. (2.3.4) becomes

$$\overleftarrow{\varepsilon} = \begin{pmatrix} a & -b \\ b^* & a^* \end{pmatrix} = \vec{a}^{\wedge}, \tag{2.3.8}$$

where $\vec{a}^{\wedge}$ is $\vec{a}$ with its off diagonal elements complex conjugated. Equation (2.3.8) represents the reciprocity expressed in the linear polarization basis. Like in circular polarization basis $\vec{a}$ can be decomposed in its reciprocal and non-reciprocal part as

$$\vec{a} = \vec{a}_r + \vec{a}_{nr}, \tag{2.3.9}$$

where $\vec{a}_r$ satisfies Eq. (2.3.8), whereas $\vec{a}_{nr}$ is such that

$$\overleftarrow{a}_{nr} = -\vec{a}_{nr}^{\wedge}. \tag{2.3.10}$$

Again $\vec{a}_r$ and $\vec{a}_{nr}$ may be expressed in terms of $\vec{a}$ and $\overleftarrow{a}$, namely

$$\vec{a}_r = \frac{1}{2}(\vec{a} + \overleftarrow{a}^{\wedge}) \quad \text{and} \quad \vec{a}_{nr} = \frac{1}{2}(\vec{a} - \overleftarrow{a}^{\wedge}) . \tag{2.3.11}$$

$\overleftarrow{a}_r$ and $\overleftarrow{a}_{nr}$ can be obtained from (2.3.11) using Eqs. (2.3.8) and (2.3.10).

2.3.2. Ideal fiber

Here an ideal fiber is thought of as a fiber which exhibits neither linear nor circular birefringence, the only perturbation the fiber undergoes is the Faraday effect. The fiber loops N times around a conductor which carries a current I. Under these conditions, the Jones matrices for forward and backward propagation are, expressed in the circular polarization basis,

$$\vec{C} = \begin{pmatrix} e^{-i\varphi_F} & 0 \\ 0 & e^{i\varphi_F} \end{pmatrix} \quad \text{and} \quad \overleftarrow{C} = \begin{pmatrix} e^{i\varphi_F} & 0 \\ 0 & e^{-i\varphi_F} \end{pmatrix}, \tag{2.3.12}$$

where φ_F is given by Eq. (2.1.2), that is φ_F = VNI. Using Eq. (2.3.2) leads to the representations in the linear polarization basis

$$\vec{c} = \begin{pmatrix} \cos\varphi_F & \sin\varphi_F \\ -\sin\varphi_F & \cos\varphi_F \end{pmatrix} \quad \text{and} \quad \overleftarrow{c} = \begin{pmatrix} \cos\varphi_F & -\sin\varphi_F \\ \sin\varphi_F & \cos\varphi_F \end{pmatrix}. \tag{2.3.13}$$

For this simple case it is worthwhile to evaluate the reciprocal and non-reciprocal parts of the Jones matrices, with the help of the equations given in Section 2.3.1. For the circular polarization basis one gets

$$\vec{C}_r = \overleftarrow{C}_r = \cos\varphi_F \begin{pmatrix} 1 & 0 \\ 0 & 1 \end{pmatrix} \quad \text{and} \quad \vec{C}_{nr} = -\overleftarrow{C}_{nr} = i\sin\varphi_F \begin{pmatrix} -1 & 0 \\ 0 & 1 \end{pmatrix}, \tag{2.3.14}$$

and for the linear one

$$\vec{c}_r = \overleftarrow{c}_r = \cos\varphi_F \begin{pmatrix} 1 & 0 \\ 0 & 1 \end{pmatrix} \quad \text{and} \quad \vec{c}_{nr} = -\overleftarrow{c}_{nr} = \sin\varphi_F \begin{pmatrix} 0 & 1 \\ -1 & 0 \end{pmatrix}. \tag{2.3.15}$$

This example shows that the Jones matrix of the Faraday effect, which is non-reciprocal, has a reciprocal part which differs from zero. On the other hand, reciprocal effects always have Jones matrices with non-reciprocal parts equal to zero.

2.3.3. Twisted fiber

In twisted fibers an optical activity, or circular birefringence, is produced by mechanical torsion. In addition, a linear birefringence, e.g. induced by bending due to coiling, may be present. If the fiber, considered as a curved line in space, lies in a plane, there is no geometrical torsion. It is assumed that the twist, the bending and the magnetic field are constant along the

fiber. In the circular polarization basis the resulting forward and backward Jones matrices in presence of Faraday effect are then [Dän92]

$$\vec{C} = \begin{pmatrix} \cos\gamma d - i\frac{VH_z+\delta}{\gamma}\sin\gamma d & i\frac{\eta}{\gamma}\sin\gamma d \\ i\frac{\eta}{\gamma}\sin\gamma d & \cos\gamma d + i\frac{VH_z+\delta}{\gamma}\sin\gamma d \end{pmatrix} \quad \text{and} \tag{2.3.16}$$

$$\overleftarrow{C} = \begin{pmatrix} \cos\gamma' d + i\frac{VH_z-\delta}{\gamma'}\sin\gamma' d & i\frac{\eta}{\gamma'}\sin\gamma' d \\ i\frac{\eta}{\gamma'}\sin\gamma' d & \cos\gamma' d - i\frac{VH_z-\delta}{\gamma'}\sin\gamma' d \end{pmatrix}, \tag{2.3.17}$$

with

$$\gamma = \sqrt{(VH_z+\delta)^2 + \eta^2} \tag{2.3.18}$$

and

$$\gamma' = \sqrt{(VH_z-\delta)^2 + \eta^2}\ . \tag{2.3.19}$$

Here H_z is the magnetic field along the fiber axis, V the Verdet constant, d the fiber length, δ the twist induced optical activity and η the bending induced linear birefringence. For a circular fiber loop of radius R around the current I, as shown in Fig. 2.3, one gets for the circular birefringence due to the Faraday effect

$$VH_z = VI/2\pi R\ . \tag{2.3.20}$$

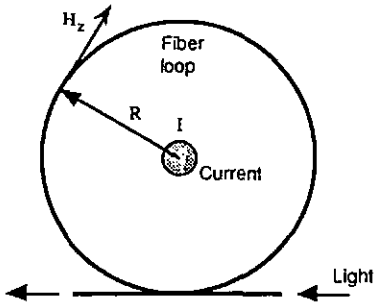

Figure 2.3 Magnetic field produced by a current I on a fiber loop.

In the same geometry δ and η are given by [Ulr79, Ulr80, Dän92]

$$\delta = n_0^2(p_{12} - p_{11})T/4 = gT/2 \tag{2.3.21}$$

and

$$\eta = (\pi n_0^3/4)(q_{12} - q_{11})\frac{E}{\lambda}\frac{r^2}{R^2} = h\frac{1}{\lambda}\frac{r^2}{R^2}\ , \tag{2.3.22}$$

where λ is the wavelength, n_0 is the effective index of refraction of the fundamental mode in the fiber without perturbation, p_{ij} and q_{ij} are the photo-elastic and piezo-optic coefficients, E is the Young's modulus, T is the twist rate (twist angle per unit length), R is the radius of curvature of the bending and 2r is the outer diameter of the fiber. For silica fibers one has typical values of $g = 0.16$ and $h = 0.43$.

From Eqs. (2.3.2), (2.3.16) and (2.3.17) the forward and backward Jones matrices in linear polarization basis are found to be

$$\vec{c} = \begin{pmatrix} \cos\gamma d + i\frac{\eta}{\gamma}\sin\gamma d & \frac{VH_z+\delta}{\gamma}\sin\gamma d \\ -\frac{VH_z+\delta}{\gamma}\sin\gamma d & \cos\gamma d - i\frac{\eta}{\gamma}\sin\gamma d \end{pmatrix} \quad \text{and} \tag{2.3.23}$$

$$\overleftarrow{c} = \begin{pmatrix} \cos\gamma' d + i\frac{\eta}{\gamma'}\sin\gamma' d & \frac{-VH_z+\delta}{\gamma'}\sin\gamma' d \\ -\frac{-VH_z+\delta}{\gamma'}\sin\gamma' d & \cos\gamma' d - i\frac{\eta}{\gamma'}\sin\gamma' d \end{pmatrix}. \tag{2.3.24}$$

For $VH_z = 0$ one gets $\overleftarrow{C} = \vec{C}^T$ and $\overleftarrow{c} = \vec{c}^{\wedge}$, which confirms reciprocity (cf. 2.3.1.).

For $\eta = 0$ the matrices simplify to those of an optical activity with a reciprocal (δ) and a non-reciprocal (VH_z) part, namely

$$\vec{C} = \begin{pmatrix} e^{-i(\delta+VH_z)d} & 0 \\ 0 & e^{i(\delta+VH_z)d} \end{pmatrix} \quad \text{and} \quad \overleftarrow{C} = \begin{pmatrix} e^{-i(\delta-VH_z)d} & 0 \\ 0 & e^{i(\delta-VH_z)d} \end{pmatrix}, \tag{2.3.25}$$

$$\vec{c} = \begin{pmatrix} \cos(\delta+VH_z)d & \sin(\delta+VH_z)d \\ -\sin(\delta+VH_z)d & \cos(\delta+VH_z)d \end{pmatrix} \text{ and } \overleftarrow{c} = \begin{pmatrix} \cos(\delta-VH_z)d & \sin(\delta-VH_z)d \\ -\sin(\delta-VH_z)d & \cos(\delta-VH_z)d \end{pmatrix}. \tag{2.3.26}$$

This also means that a twisted fiber can be considered as a circular polarization maintaining fiber (medium with high optical activity) as long as $\delta >> \eta$, i.e. if the twist induced circular birefringence is larger than the expected linear birefringence due to external perturbations of the fiber, such as bending or squeezing. Typical values for silica fibers at 633 nm are $\delta = 15$ rad/m

and $\eta = 1.21$ rad/m for a fiber outer radius of $r = 40$ µm, a twist rate of $T = 30 \times 2\pi$ rad/m and a bending radius of $R = 30$ mm.

2.3.4. Spun fiber

Spun fibers are produced by spinning birefringent fibers during the drawing process. The local properties are characterized by the linear birefringence and the rotation rate of the principal axis, corresponding to the spin rate. When the local birefringence is small (residual birefringence), the fiber is referred to as an "ultra-low birefringence" fiber [Bar81], whereas when the birefringence is large (voluntary introduced stress- or shape-induced linear birefringence), it is referred to as an "spun high-birefringence" or "cicular-polarization maintaining" fiber [Li87]. In a high-birefringence spun fiber the axes of the birefringence η rotates at a spin rate α. It is assumed that the birefringence, the spin rate and the magnetic field are constant along the fiber. In the circular polarization basis the resulting forward and backward Jones matrices in presence of Faraday effect are then [Dän92]

$$\vec{C} = \begin{pmatrix} (\cos\gamma d - i\frac{VH_z-\alpha}{\gamma}\sin\gamma d)e^{-i\alpha d} & (i\frac{\eta}{\gamma}\sin\gamma d)e^{-i\alpha d} \\ (i\frac{\eta}{\gamma}\sin\gamma d)e^{i\alpha d} & (\cos\gamma d + i\frac{VH_z-\alpha}{\gamma}\sin\gamma d)e^{i\alpha d} \end{pmatrix} \tag{2.3.27}$$

and

$$\overleftarrow{C} = \begin{pmatrix} (\cos\gamma' d + i\frac{VH_z+\alpha}{\gamma'}\sin\gamma' d)e^{-i\alpha d} & (i\frac{\eta}{\gamma'}\sin\gamma' d)e^{i\alpha d} \\ (i\frac{\eta}{\gamma'}\sin\gamma' d)e^{-i\alpha d} & (\cos\gamma' d - i\frac{VH_z+\alpha}{\gamma'}\sin\gamma' d)e^{i\alpha d} \end{pmatrix}, \tag{2.3.28}$$

with

$$\gamma = \sqrt{(VH_z - \alpha)^2 + \eta^2} \tag{2.3.29}$$

and

$$\gamma' = \sqrt{(VH_z + \alpha)^2 + \eta^2}\ . \tag{2.3.30}$$

Setting $VH_z = 0$ leads again to $\overleftarrow{C} = \vec{C}^T$, which confirms reciprocity (cf. 2.3.1.). From Eqs. (2.3.27) and (2.3.28) the forward and backward Jones matrices in linear polarization basis can be found through Eq. (2.3.2).

The Jones matrices for spun fibers are very similar to those for twisted fibers, however there is a fundamental difference: For zero birefringence ($\eta = 0$, $\gamma = VH_z \pm \alpha$) the rotational effects of the fiber, which are purely geometrical, disappear and only the Faraday effect remain. On the

other hand, for $\sin\gamma d = 0$ the above matrices simplify to those of an optical activity equivalent to α.

For slow rotation of the birefringence, i.e. for $\alpha << \eta$, a spun fiber behaves like a linear polarization maintaining fiber. This can be seen from the Jones matrix, for $\alpha << \eta$ and $VH_z << \eta$, applied to the two orthogonal linear input polarizations parallel to the input local birefringence axis. In this case the output polarizations are still linear and orthogonal, but rotated by an angle αd and with an additional phase of $\pm\eta d$, corresponding to the retardation of the fast and the slow axis, respectively. For hi-bi or linear polarization maintaining fibers the value of η is commonly characterized by the beat length $L_b = \pi/\eta$. Typical values are $L_b = 3$ mm, corresponding to a linear birefringence of $\eta = 10^3$ rad/m.

For fast rotation of the birefringence axes, i.e. for $\alpha >> \eta$, a spun fiber behaves rather like a circular polarization maintaining fiber. In this case, and if $\alpha >> VH_z$, the Jones matrices simplify to those of an optical activity with a reciprocal ($\rho = -\eta^2/2\alpha$) and a non-reciprocal (VH_z) part [Dän92], and take the form given by Eqs. (2.3.25) and (2.3.26). However, in practice the equivalent circular birefringence is still very small compared with the local linear birefringence and therefore the circular polarization maintaining properties are achieved only for long fibers. Fibers with $\eta = 0.95\times10^3$ rad/m ($L_b = 3.3$ mm) and $\alpha = 1.2\times10^3$ rad/m have been reported in the literature [Li87].

For small local birefringence η and $VH_z = 0$, the equivalent optical activity $\rho = -\eta^2/2\alpha$ is negligible and the maximum residual birefringence reduces to η/α. One gets an "ultra-low birefringence fiber" [Bar81], which can be used to measure the Faraday effect without perturbation by linear birefringence. Typical values for silica fibers at $\lambda = 633$ nm are $\alpha = 120$ rad/m and $\eta \leq 5$ rad/m. But these fibers are still vulnerable to external perturbations causing birefringence.

2.3.5. Helicel fiber

The curved line in space of a right-handed helix is described in Cartesian coordinates x,y,z as a function of the path length s by

$$x = a\cos(s/s_0)\,, \quad y = a\sin(s/s_0)\,, \quad z = b(s/s_0)\,, \tag{2.3.31}$$

where z is the axis, a the radius and $2\pi b$ the pitch of the helix, and $s_0^2 = a^2 + b^2$.

The curvature κ and the geometrical torsion τ of the helix are

$$\kappa = \frac{a}{s_0^2} = \frac{a}{a^2 + b^2} \quad \text{and} \quad \tau = \frac{b}{s_0^2} = \frac{b}{a^2 + b^2}\,. \tag{2.3.32}$$

The helix angle θ is defined by the relation

$$\mathrm{tg}\theta = b/a\,. \tag{2.3.33}$$

The maximum torsion for a given radius a is obtained for $\theta = 45$ °, i.e. for $b = a$, and has the same value as the curvature, namely $\tau = \kappa = 1/2a$.

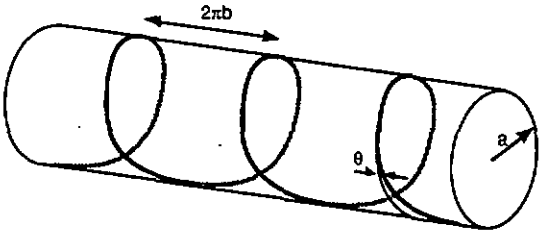

Figure 2.4 Helical fiber.

In a helical fiber, shown in Fig. 2.3, the bending induces a birefringence η with its axes aligned to the normal and the binormal directions of the helix. The value of the bending induced birefringence is obtained from Equ. (2.3.22) with $1/R = \kappa$. It has been shown [May89, Dän92] that a helical fiber and a high-bi spun fiber behave similarly. Therefore, including a constant Faraday effect VH_z, the Jones matrices are exactly the same as those for spun fibers with constant spin rate $\alpha = \tau$ and constant birefringence η, which are given in Eqs. (2.3.27), (2.3.28). The Faraday effect VH_z is given by Eq. (2.3.20) with $R = s_0$. For the case of maximum torsion ($\theta = 45$ °) one gets with the help of Eq. (2.3.22) for silica fibers

$$\eta = 0.43\,\frac{1}{\lambda}\left(\frac{r}{2a}\right)^2 \quad \text{and} \quad \tau = \frac{1}{2a}\ . \tag{2.3.34}$$

This yields for a helix diameter of $2a = 30$ mm and a fiber diameter of $2r = 80$ µm at the wavelength $\lambda = 633$ nm the values $\eta = 1.21$ rad/m and $\alpha = \tau = 33.3$ rad/m.

A helical coil with a sufficiently large geometrical torsion ($\tau = \alpha >> \eta$) is a convenient configuration to overcome the perturbing effects of the bending induced birefringence (cf. 2.3.3). As can be seen from Eq. (2.3.27) the Jones matrix $\vec{C}$ becomes diagonal for $\gamma d = m\pi$, where m is an integer, which means purely circular birefringence. For optimum detection of the Faraday effect one should therefore choose the length d of the fiber so that the above condition is satisfied for $VH_z = 0$, i.e. for $\gamma = \gamma_0 = (\alpha^2 + \eta^2)^{1/2}$. In general, the length of the helix satisfying this condition will not correspond to an integer number of periods, i.e. the projection of the helix onto a plane perpendicular to its axis does not form a closed loop. If the electrical conductor is not precisely positioned in the axis of the helix, this may result in an error for the measured Faraday effect [May89]. It is therefore desirable for a current sensor, that the helical coil satisfies the condition $\gamma_0 d = m\pi$ for an integer number M of periods, i.e. $d = M2\pi s_0$. This can be achieved by choosing the diameter 2a and the pitch $2\pi b$ of the helix appropriately. By using the definitions given above for τ, η, s_0 and θ, the condition $\gamma_0 M2\pi s_0 = m\pi$ yields

$$a/a' = \frac{\cos^3\theta}{[(m/M)^2 - 4\sin^2\theta]^{1/2}}\ , \tag{2.3.35}$$

where $a' = 2hr^2/\lambda$ depends only on the fiber parameters and the wavelength, and with a typical value of $h = 0.43$ for silica fibers. Equation (2.35) permits us to calculate the geometrical parameters of the helix satisfying the condition $\gamma_0 M2\pi s_0 = m\pi$.

3. DETECTION OF THE FARADAY EFFECT

In current sensor applications, the detection of the Faraday effect permits to recover the value of the electrical current to be measured. The Faraday rotation φ_F can be detected using either polarimetric or interferometric optical readout schemes.

In the basic scheme [Pap80, Smi78, Ras79] of polarimetric readout, a linearly polarized wave is launched in the fiber and the output is analyzed by a polarization beamsplitter (e.g. a Wollaston prism) whose principal axes are oriented at 45° with respect to the input polarization. Photodetectors, located at each beamsplitter output, supply two signals from which, after processing, $\sin 2\varphi_F$ is obtained, regardless of fluctuations of the optical power, launching efficiency and detector responsivity [Ras79]. In this basic configuration, the dynamic range and linearity are limited by the $\sin 2\varphi_F$ dependence. A more efficient method [Don88], which ensures an unlimited dynamic range at the expense of some complexity, is to supplement the optical detector section with a second beamsplitter, oriented with an axis parallel to the input polarization. Using the same signal processing as before, an additional signal proportional to $\cos 2\varphi_F$ is obtained. From $\sin 2\varphi_F$ and $\cos 2\varphi_F$ the Faraday rotation φ_F can be retrieved. Balanced polarimetric readout is obtained by using a sensing fiber coil with a mirrored end and reading the return wave at the input end [Don88], so that reciprocal birefringence effects are in a large part compensated whereas the non-reciprocal Faraday effect is doubled.

The non-reciprocal Faraday phase shift $2\varphi_F$ between orthogonal circular polarizations propagating in the same direction or, equivalently, between two counter propagating circular polarizations with the same handedness, can in principle be read by a variety of interferometric configurations. When both circular polarizations have the same optical frequency, this is referred to as homodyne detection. In this case the Faraday phase shift can be recovered by using classical phase modulation techniques. However, to achieve an output signal which is proportional to the Faraday effect, regardless of fluctuations of the optical power, launching efficiency and detector responsivity, complex homodyne detection schemes have to be used [Gia82]. Heterodyne detection, where the two circular polarizations have different optical frequencies, provides directly the Faraday phase shift $2\varphi_F$, regardless of fluctuations of the optical power, launching efficiency and detector responsivity. Typically a Bragg cell is used to shift the optical frequency of one arm of the interferometer with respect to the other [Bus89, May88]. A two frequency Zeeman laser can also be used [Fer82]. The Faraday signal, which modulates the phase of the carrier oscillating at the beat frequency, is obtained from the detected optical signal using a FM discriminator or, if a reference signal is available, a phasemeter. An other form of heterodyne detection is the so called pseudo-heterodyne detection [Ker86]. In this technique, the phase of the interferometer is sinusoidally swept using either a piezoelectric fiber stretcher or by using a sinusoidally frequency swept laser source. Unlike the classical heterodyne detection, which uses bulk elements such as Bragg cells, pseudo-heterodyne detection is well suited for the realization of all-fiber current sensors [Ker89]. Reciprocal interferometers, like the Sagnac interferometer and the reflection interferometer, permit to cancel to a large extent the unwanted reciprocal effects due to residual birefringence in the fiber, whereas the non-reciprocal Faraday effect remains. Several fiber current sensors using Sagnac

interferometer with different detection techniques, such as homodyne or heterodyne detection, have been reported in the literature [Fer82, Lei86, Ann87, Nic88, Fro92].

3.1. Heterodyne detection of the Faraday effect with helical coil

One of the principal problems of the optical fiber current sensor is how to make a fiber coil having low linear birefringence and/or high circular birefringence and being at the same time temperature and vibrations insensitive. Moreover, this coil should be easy to manufacture in a well controlled manner and no problems due to mechanical strain should arise at the fixation of the two fiber ends. Finally, the coil dimensions should be well suited for the considered application of the current sensor. The optical fiber helical coil permits to fulfil most of the above mentioned conditions, in particular the geometrical torsion is much higher (≥ 10times) than the bend induced birefringence, ensuring a good sensitivity to the Faraday effect and a low sensitivity to temperature and vibrations. The geometry of the helix can be perfectly controlled and holding the fiber ends is not a problem, since there is no mechanical twist in the fiber. The increasing length of the helical coil with increasing number of turns could be critical for current sensors on high voltage power lines, however, it is often not necessary to have a large number of turns.

A 10 turn helical coil of 30 mm diameter and 520 mm length has been constructed using a 80 µm ultra low-birefringence spun fiber (York LB 600). The measured total birefringent retardation of the helical coil was lower than 1°, which is an excellent result. This coil has been used as a heterodyne current sensor in transmission, the source was a two frequency He-Ne Zeeman laser. Perfect linearity between the detected Faraday phase shift and the current was measured from 0 A to 50 A. The sensitivity and the accuracy ware essentially limited by the shot-noise, corresponding to about 32 mA/√Hz for 20 µW detected optical power. Measurements of the Faraday effect for different positions of the electrical conductor inside the helical coil resulted in no change of the sensitivity.

3.1.1. Realization and birefringence measurement of the helical coil

Based on Eq. (2.35), the geometrical parameters of the helix are chosen in such a way that $\gamma_0^2 \pi s_0 = n$, which means that M = m (cf. Section 2.3.5). Taking into account these conditions, a 10 turn helical coil has been constructed with the following parameter: ultra-low birefringence fiber (York LB 600), fiber diameter 2r = 80 µm, coil diameter 2a = 29.8 mm, helix pitch $2\pi b$ = 52 mm, helix angle $\theta = \tan^{-1}(b/a) = 29.05°$, number of periods M = 10, helix length $M2\pi b$ = 520 mm, fiber length $d = M2\pi s_0$ = 1071 mm, circular birefringence α = 28.5 rad/m and linear birefringence η = 2.86 rad/m (at λ = 633 nm). These practically realized values differ slightly from the theoretical values satisfying the condition $\gamma_0^2 \pi s_0 = \pi$.

The coating of the fiber induces unwanted birefringence, typically amounting to several degrees; it must therefore be removed. The uncoated fiber is inserted into a teflon capillary filled with liquid paraffin, ensuring minimum mechanical twist. The helix is formed by winding the fiber around a threaded plexiglass cylinder. The linear retardation of the helix was shown to be smaller than 1°, using a high resolution ellipsometer [Bar85] for the measurement.

3.1.2. Heterodyne detection of the Faraday effect

Two orthogonal circular polarizations, frequency shifted by $\Delta\omega/2\pi$, are launched at the input of the helix. At the output, one has two frequency shifted nearly circular orthogonal modes, with a phase difference depending on the Faraday effect. A linear polarizer, placed at the helix output, causes the two frequency shifted modes to interfere. Let E_{i1} and E_{i2}, be the Jones vectors of the two orthogonal input polarizations given in the circular basis, namely

$$E_{i1} = \begin{pmatrix} 1 \\ 0 \end{pmatrix} e^{i\Delta\omega t/2} \quad \text{and} \quad E_{i2} = \begin{pmatrix} 0 \\ 1 \end{pmatrix} e^{-i\Delta\omega t/2} \ . \tag{3.1.1}$$

The output Jones vector is then

$$E_o = \mathbf{P}\,\mathbf{C}\,(E_{i1} + E_{i2}) \ , \tag{3.1.2}$$

where **P** and **C** are the Jones matrices of the linear polarizer and the helical coil, respectively. The Jones matrix **C** of the helix, in the circular polarization basis, is given by Eq. (2.3.27) and is of the form

$$\mathbf{C} = \begin{pmatrix} A & -B^* \\ B & A^* \end{pmatrix} , \tag{3.1.3}$$

where

$$A = (\cos\gamma d + i\,\frac{VH_z - \alpha}{\gamma}\sin\gamma d)e^{i\alpha d} \quad \text{and} \quad B = (i\frac{\eta}{\gamma}\sin\gamma d)e^{-i\alpha d} \ , \tag{3.1.4}$$

with $\gamma = \sqrt{(VH_z - \alpha)^2 + \eta^2}$ and $\alpha = \tau$ (geometrical torsion of the helix). The Jones matrix of the linear polarizer, in the circular polarization basis, with its transmission axis oriented at an angle ψ respect to the horizontal reference axis, is

$$\mathbf{P} = \frac{1}{2}\begin{pmatrix} 1 & e^{-i\psi} \\ e^{i\psi} & 1 \end{pmatrix} . \tag{3.1.5}$$

Starting from Eq. (3.1.2) one finds for the output intensity

$$I_o = E_o^{\dagger}E_o = |A|^2 + |B|^2 + \mathrm{Re}\{(A^2e^{i2\psi} - B^2e^{-i2\psi})e^{i\Delta\omega t}\} \ , \tag{3.1.6}$$

where $X^{\dagger}$ is the hermitian conjugate of the Jones vector **X**.

In the ideal case, where the fiber exhibits no linear birefringence($\eta = 0$), one has, using $VH_z = VI/2\pi s_0$ and $d = N2\pi s_0$ (cf. Section 2.3.5),

$$A = e^{i(\gamma+\alpha)d} = e^{iVH_zd} = e^{iVNI} \quad \text{and} \quad B = 0 \ . \tag{3.1.7}$$

Replacing the actual values of A and B in Eq. (3.1.6), the output intensity becomes

$$I_o = 1 + \cos(\Delta\omega t + 2VNI + 2\psi) = 1 + \cos(\Delta\omega t + \varphi_d) \tag{3.1.8}$$

Therefore in the ideal case (no bending induced birefringence), the detected phase φ_d of the heterodyne signal yields directly the Faraday effect (multiplied by 2). The azimuth ψ of the linear polarizer only induces a constant phase shift.

For the real case, where $\eta \neq 0$ and assuming that $\alpha >> \eta$ and $\alpha >> VH_z$, the helical fiber behaves rather like a circular polarization maintaining fiber (cf. Section 2.3.4). In this case the Jones matrix simplifies to those of an optical activity with a reciprocal ($\rho = -\eta^2/2\alpha$) and a non-reciprocal (VH_z) part. The exact solution for the output intensity is given by Eq. (3.1.6) and can be rewritten in the form

$$\begin{aligned} I_o &= |A|^2 + |B'|^2 + \mathrm{Re}\{|A^2 - B'^2|e^{i(\Delta\omega t + \varphi + 2\psi)}\} \\ &= |A|^2 + |B'|^2 + |A^2 - B'^2|\cos(\Delta\omega t + \varphi + 2\psi), \end{aligned} \tag{3.1.9}$$

where $B' = Be^{-i2\psi}$, and φ is the interference phase given by

$$A^2 - B'^2 = |A^2 - B'^2|e^{\varphi}. \tag{3.1.10}$$

From Eq. (3.1.10) one obtains

$$\varphi = \tan^{-1}\left(2\,\frac{Re\{A\}Im\{A\} - Re\{B'\}Im\{B'\}}{Re^2\{A\} - Im^2\{A\} - Re^2\{B'\} + Im^2\{B'\}}\right). \tag{3.1.11}$$

For $\alpha >> \eta$, Eq. (3.1.11) reduces to

$$\varphi = 2VNI - (\eta^2/\alpha)d. \tag{3.1.12}$$

Finally for the real case the detected phase is given by

$$\varphi_d = 2VNI - (\eta^2/\alpha)d + 2\psi. \tag{3.1.13}$$

If one compares with the ideal case ($\eta = 0$), the detected phase is shifted by $-(\eta^2/\alpha)d$, which is $(\eta^2/\alpha)d = 0.31$ rad for the actual helical coil ($\alpha = 28.5$ radm^{-1}, $\eta = 2.86$ radm^{-1} and $d = 1071$ mm). This phase offset is not negligible and can be an important drawback for dc detection of the Faraday effect. However it can be compensated by adjusting the azimuth of the linear polarizer such that $2\psi = (\eta^2/\alpha)d$. Figure 3.1 shows the theoretical value of the detected phase versus the Faraday phase, as calculated from Eq. (3.1.11), for the actual coil and for $\psi = 0°$.

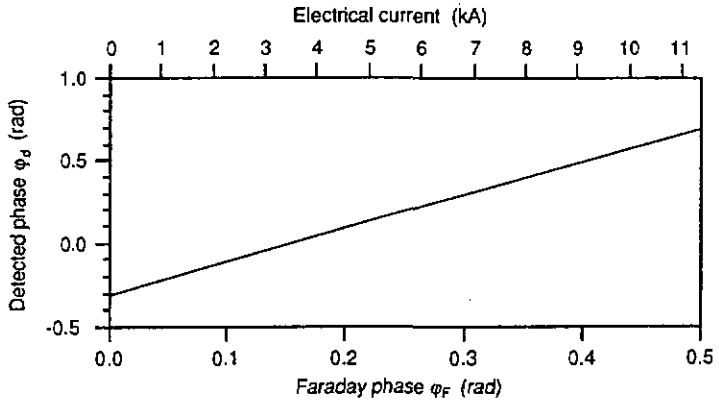

Figure 3.1 Calculated phase for heterodyne detection using the actual 10 turn helical coil at $\lambda = 633$ nm (V $\approx$ 4.4 µrad/A) and for $\psi = 0°$.

The detected phase given by Eq. (3.1.13) depends linearly on the Faraday effect, however the exact behavior predicted by Eq. (3.1.11) will slightly differ from this linear dependence. Figure 3.2 gives the relative error, calculated from Eqs. (3.1.11) and (3.1.12), between the linear approximation and the exact dependence of the detected phase for the parameters of the actual helical coil (cf. 3.1.1) and for $\psi = 0°$. This example shows that the resulting error is approximately ≤ 0.12 %, which is negligible for most current sensor applications.

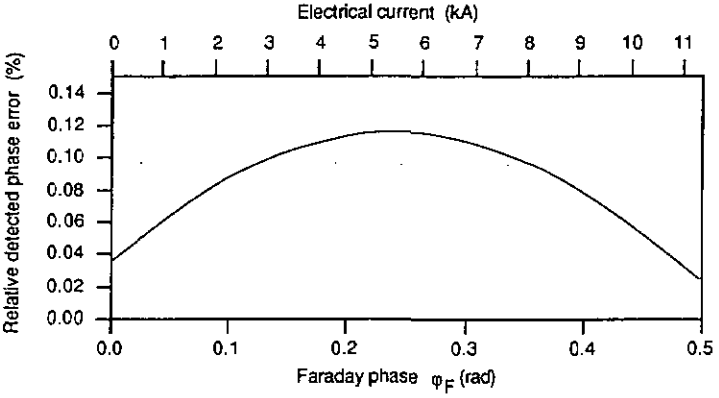

Figure 3.2 Calculated relative error between the detected phase and the linear approximation for heterodyne detection using the actual 10 turn helical coil at $\lambda = 633$ nm (V $\approx$ 4.4 µrad/A) and for $\psi = 0°$.

3.1.3. *Optical set-up and signal processing*

Figure 3.3 shows the experimental set-up used. The Faraday phase shift is obtained by measuring the relative phase between the reference and the detector signal, each varying at the beat frequency of the Zeeman laser (1.8 MHz). The detector signal results from the interference between the two orthogonal circular polarizations after the linear polarizer P (cf.Section 3.1.2).

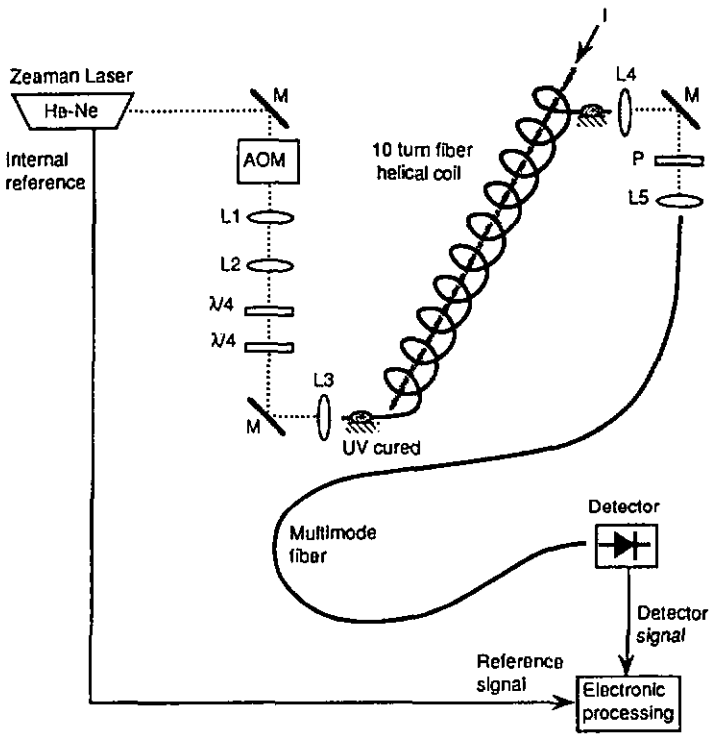

Figure 3.3 Experimental set-up for heterodyne detection.

The beam diameter at the laser output is 5mm, the lenses L_1 (f = 100 mm) and L_2 (f = 20 mm) reduce the beam diameter to 1mm so as to ensure a good behavior of the two retardation plates and an efficient beam injection into the fiber coil. The acousto-optic modulator (AOM) driven at 40 MHz acts as an optical isolator for the reflected light coming back from the input and output ends of the fiber and returning exactly into the laser cavity. The first quarter wave plate compensates the residual birefringence of the lenses and the AOM, the second quarter wave plate transforms the two orthogonal linear polarizations of the Zeeman laser into two orthogonal circular polarizations. L_3, L_4, L_5 are microscope objectives. After the polarizer P the beam intensity varies at 1.8 MHz, which is the beat frequency between the two orthogonal polarizations of the Zeeman laser. The multimode fiber allows remote detection of the

interference signal, this is an efficient means to have good electromagnetic immunity. The 10 turn helical coil forms the sensing element (cf. Section 2.1.3). The current source supplies an ac current with a frequency of 170 Hz. The maximum available current is about 100 A. The signal processing part consists of a coherent phase demodulator [Fro92] providing an output signal proportional to the ac part of the detected phase φ_d. This signal is measured with a FFT spectrum analyzer.

3.1.4. Experimentel results

The power delivered by the laser was 450 µW and the detected power was 20 µW. Therefore only 4.5 % of laser power was available at the output of the optical system. The signal to noise ratio at the detector was measured to be SNR_d = 82 dB for 10 kHz detection bandwidth, which is nearly shot noise limited. The signal to noise ratio of the reference was measured to be SNR_r = 77 dB for 10 kHz detection bandwidth. The resulting error of the ac part of the detected phase φ_d is given by

$$\delta\varphi_{dn} = (1/\sqrt{2})(SNR_d^{-1} + SNR_r^{-1})^{1/2}, \qquad (3.1.14)$$

which yields $\delta\varphi_{dn}$ = 115 µrad. The voltage noise measured at the phase demodulator output, using a FFT spectrum analyzer with a detection bandwidth of 6 Hz, was equivalent to $\delta\varphi_{dn}$ = 4 µrad. Converted to 10 kHz this yields $\delta\varphi_{dn}$ = 163 µrad, which is close to the expected value given above. This corresponds to a phase noise density of 1.63 µrad/√Hz, or a current noise density of 31.6 mA/√Hz. Figure 3.4 shows the detected phase φ_d, measured in 6 Hz bandwidth, versus the electrical current I. Measurements with different positions and orientations of the electrical conductor inside the coil did not show any change of the detected Faraday phase.

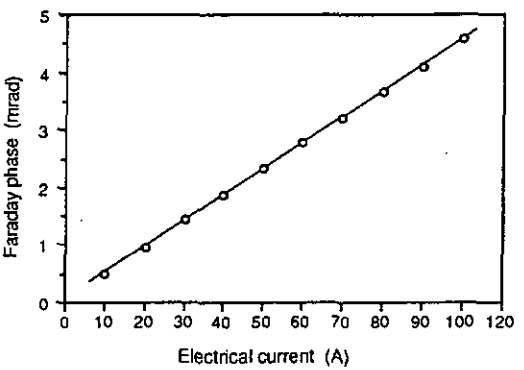

Figure 3.4 Measured Faraday phase versus electrical current I.

A linear fit to the measured values yields for the standard deviation from the mean value $\sigma_{\varphi d}$ = 1.292 mrad and for the correlation coefficient r = 0.9999734. From this one gets with

$$\delta\varphi_d = \sigma_{\varphi d}\sqrt{1 - r^2} \tag{3.1.15}$$

for the rms error of the detected phase $\delta\varphi_d = 9.4$ µrad, which corresponds to $\delta I = 0.2$ A for the current, which is somewhat larger than the measured phase noise of $\delta\varphi_{d\,n} = 4$ µrad. This difference may be attributed to the reading error of the ampere-meter, which has 100 A full scale and 1 % maximum error specified by the manufacturer.

In conclusion, the helical fiber coil used as Faraday current sensor gives excellent results. The fact that the geometrical torsion α (~ 30 rad/m) is large compared to the bend induced birefringence η (~ 3 rad/m) maintains the eigenpolarizations nearly circular for all values of the current within the considered range, which results in a nearly ideal situation for the detection of the Faraday effect. Since the fiber has no mechanical twist, there is no problem to hold its extremities. A practical problem arises from the fact that the coating must be removed in order to avoid additional birefringence. However, this problem could be circumvented with another type of coating, which does not induce birefringence. With 20 µW detected power shot noise limited detection was achieved, resulting in a phase noise density of 1.63 µrad/√Hz which corresponds to a current noise density of 31.6 mA/√Hz.

3.2. Reciprocal interferometers for Faraday effect detection

As mentioned above, reciprocal interferometers, like Sagnac and reflection interferometers, permit to cancel to a large extent the unwanted reciprocal effects due to residual birefringence in the fiber, whereas the Faraday effect remains unaffected. In this section, the basic principles of the Sagnac and the reflection interferometers used to detect Faraday effect will be described. Detailed theoretical and experimental investigations will be given in chapters 4 and 5.

3.2.1. The Sagnac interferometer for Faraday effect detection

The fiber optic Sagnac interferometer is well known for its application as a gyroscope. However, only few contributions [Fer82, Lei86, Don88, Nic88] concerning its application as Faraday current sensor have been reported. It is obvious that the Sagnac interferometer offers several advantages for optical current sensing compared to classical detection schemes. When used in a strictly reciprocal configuration, it is only sensitive to non-reciprocal effects, such as the Sagnac effect or the Faraday effect. The two interfering light waves travel in opposite directions using the same polarization mode of the fibers. Therefore, linear polarization maintaining fibers to and from the sensing head can be included in the interferometer, which allows to place all detection and modulation elements at ground potential. Finally, the Sagnac current sensor could benefit of the well established fiber optic gyroscope technology.

The Sagnac interferometer used to detect the Faraday effect is obtained from the minimum reciprocal configuration of the fiber gyroscope [Eze82]. To detect correctly the Faraday effect one must ensure that the two counter propagating polarizations in the sensing coil are circular and have the same handedness. Figure 3.5 shows the resulting minimum reciprocal configuration of an all-fiber Sagnac interferometer for Faraday effect detection. The detected non-reciprocal phase is $2\varphi_F$, where φ_F is defined by Eq. (2.1.1). Circular polarizations are obtained from linear polarizations by using all-fiber quarter wave retarders ($\lambda/4$). The Faraday

sensing coil can be any classical configuration. In order to maintain the linear polarization emerging from the all-fiber polarizer up to the all-fiber quarter wave retarders in the Sagnac loop, one has to use a polarization maintaining coupler, a polarization maintaining phase modulator and polarization maintaining fiber (hi-bi fiber). The coupler between the light source and the all-fiber polarizer has not to be polarization maintaining. Direct cross-talk arising anywhere in the Sagnac loop will be eliminated by the polarizer P. Low coherence sources have to be used in order to avoid perturbations induced by Rayleigh back-scattering and indirect cross-talk (light returning into initial polarization state after two successive cross-couplings) in the hi-bi fiber.

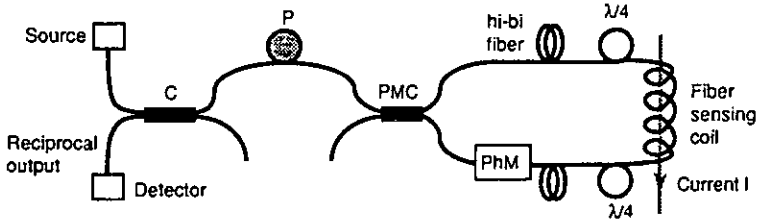

Figure 3.5 Minimum reciprocal configuration of an all-fiber Sagnac interferometer for Faraday effect detection. C: coupler, P: all-fiber polarizer, PMC: polarization maintaining coupler, PhM: polarization maintaining phase modulator.

3.2.2. The reciprocal reflection interferometer for Faraday effect detection

A reciprocal interferometer can also be obtained by using a highly linear birefringent fiber connected to a quarter wave fiber loop which is end mirrored and whose birefringence axes are oriented at 45° respect to those of the hi-bi fiber. If linear polarizations are launched into each birefringence axis of the hi-bi fiber, their accumulated relative phase for one total round trip is zero. Indeed, thanks to the end mirrored quarterwave loop, each linear polarization will use one birefringence axis in forward direction and the orthogonal one in the backward direction, resulting in exactly the same optical path for both polarizations. Each linear polarization coming from the hi-bi fiber is transformed into circular polarization after the quarterwave loop. If some Faraday effect is present between the quarterwave loop and the mirror, the two circular polarizations will be non-reciprocally phase shifted with respect to each other. Therefore, after one total round trip, the two output linear polarizations undergo twice the Faraday effect and will be phase shifted by $4\varphi_F$. Linear birefringence effects in the hi-bi fiber and twist induced optical activity arising in the fiber between the loop and the mirror, are canceled out thanks to the reciprocity of the interferometer. Figure 3.6 shows the principle of the reciprocal reflection interferometer used for Faraday effect detection.

The hi-bi fibers to and from the sensing head allow to place all detection and modulation elements at ground potential. At the interferometer output a polarizer causes the two output linear polarizations to interfere. The interference signal is proportional to $(1+\cos 4\varphi_F)$ and has therefore a vanishing sensitivity for weak Faraday effect. This problem can be overcome if the two linear polarizations are phase shifted by $\pi/2$ (quadrature detection), using a quarterwave plate for example. This phase shift can be achieved at the input of the interferometer before the

coupler, or at the output after the coupler. The different parts of the interferometer, such as the sensing coil, the quarterwave loop and the hi-bi fiber, are not ideal and therefore introduce cross-coupling between the two propagating orthogonal modes. However, unlike the principal propagating modes, reciprocity is not realized for cross-coupled modes. For example, if cross-coupling arises in the sensing coil, the cross-coupled part will use the same polarization mode of the hi-bi fiber for forward and backward propagation; this results in non-zero phase shift at the interferometer output due to the high birefringence of the polarization maintaining fiber. This cross-coupled part will therefore perturb the Faraday phase detection. But, if low coherence sources and sufficiently long hi-bi fibers are used, no interference caused by cross-coupled light will occur, since the imbalance of the optical paths is larger than the coherence length of the source. As a consequence, the cross-talk arising in the interferometer will no longer perturb the detection of the Faraday effect.

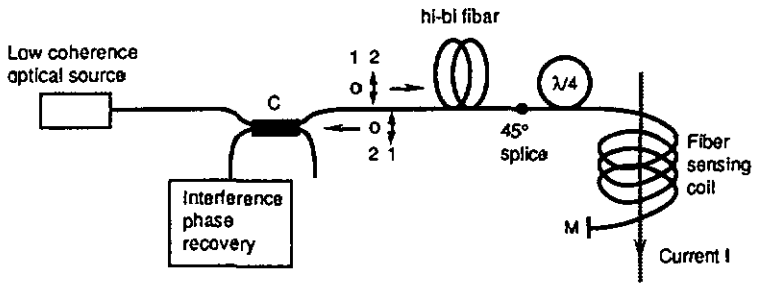

Figure 3.6 Principle of the reciprocal reflection interferometer for Faraday effect detection. C: coupler, M: mirror.

The arrangement depicted by Fig. 3.6 has an important drawback, the coupler C might be birefringent (which is always the case in practice); moreover, the axes of this birefringence are randomly oriented with respect to the hi-bi fiber axes, therefore an uncontrolled additional phase shift will perturb the detected Faraday phase. This phase will vary with environmental conditions, which is not acceptable for current sensor applications. Using a polarization maintaining coupler with axes aligned to those of the hi-bi fiber is not a good remedy, because the output arm of the coupler, due to its high birefringence, will still introduce an unwanted additional phase to the detected Faraday phase. The problem of the birefringence of the coupler can be eliminated if the returning light is made to interfere before the coupler. This is achieved by inserting a polarizer between the coupler an the hi-bi fiber, as shown in Fig. 3.7. As a consequence, the coupler has only to transmit the intensity of the interference which is not affected by the birefringence. However, the sensitivity of the interference signal to the Faraday phase vanishes for weak Faraday effect because the detection is not performed in quadrature. The only way to solve this problem is to introduce a non-reciprocal phase shift inside the interferometer itself. The easiest way to produce an efficient non-reciprocal phase shift is to periodically modulate the relative phase of the two linear polarizations at the hi-bi fiber input with the help of a birefringence modulator. If the modulation period is equal to half the time of flight for a total round trip, an optimum non-reciprocal relative phase modulation is obtained. In practice, such a birefringence modulator can be realized using a hi-bi fiber wound around a

piezoceramic stretcher [Var83]; integrated optic modulators are also good candidates. The resulting interference signal is similar to the one obtained with classical non-reciprocal phase modulation for the fiber gyroscope, therefore the same signal processing can be used.

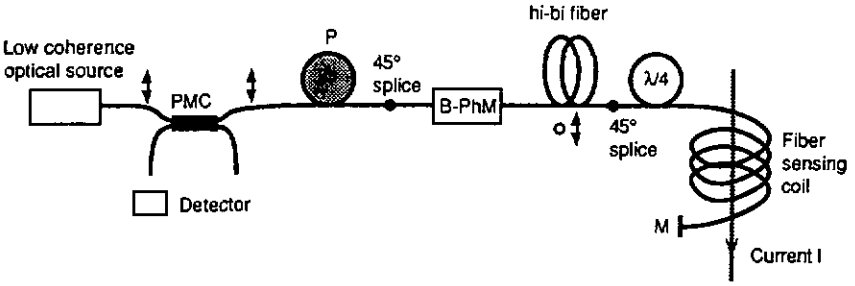

Figure 3.7 Reciprocal reflection interferometer for Faraday effect detection. PMC: polarization maintaining coupler, P: all-fiber polarizer, B-PhM: birefringent phase modulator, M: mirror.

In conclusion, the reflection interferometer is reciprocal, like the Sagnac interferometer. However, to achieve similar performance it requires only one quarterwave loop and half the number of splices; this is very important for practical current sensors realizations. Moreover, its sensitivity to the Faraday effect is twice as much as for the Sagnac interferometer, thus for the same sensitivity a sensing coil with half the number of turns can be used, ensuring better immunity to external perturbations. To become insensitive to non-ideal components (cross-talk in hi-bi fiber, birefringence of coupler) similar tricks as in the all-fiber Sagnac interferometer have to be used: low coherence source, non-reciprocal phase modulation (birefringence).

4. THE SAGNAC INTERFEROMETER WITH FARADAY EFFECT

This chapter reports the detailed theoretical and experimental investigations of the Sagnac interferometer used to detect the Faraday effect. Section 4.1 gives the basic equations of the detected intensity at the reciprocal Sagnac output for different fiber coil configurations. Principles of the Faraday phase recovery and results for different fiber configurations are dealt with in section 4.2. In sections 4.3 to 4.5 the influence of the non-ideal elements is analyzed. Experimental results are reported in Sections 4.6 and 4.7.

4.1. Jones matrices and detected intensity

The minimum reciprocal configuration of the Sagnac interferometer is illustrated in Fig. 3.5. In order to ease the theoretical analysis it is convenient to use a bloc-diagram representation as shown in Fig. 4.1.

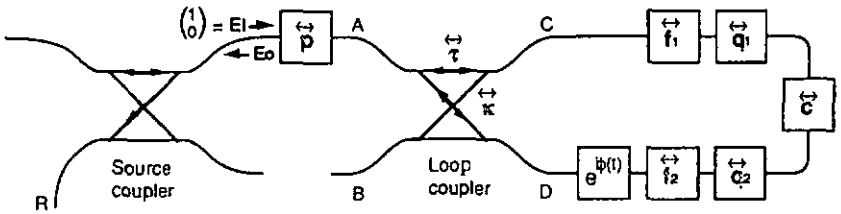

Figure 4.1 Bloc-diagram representation of the minimum reciprocal configuration of the Sagnac interferometer configured for Faraday effect detection.

Each bloc corresponds to a Jones matrix of an individual element constituting the Sagnac interferometer. Except for the sensing coil, which features circular birefringence, the elements of the interferometer are linearly birefringent and have the same orientation of the birefringence axes, exept for the quarterwave loops. Therefore the linear polarization basis is better suited for the calculations. The reference frame (x,y,z) has its x axis parallel to the input linear polarization, which is represented by the Jones vector E_i, and the orientation of the z axis is given by the propagation vector k. The Jones matrices are forward matrices for clockwise propagation and backward matrices for counter-clockwise propagation, namely $\overleftrightarrow{x} = \vec{x}$ and $\overleftrightarrow{x} = \overleftarrow{x}$ for clockwise and counter-clockwise propagations, respectively. The linear polarizer $\overleftrightarrow{p}$ has its transmission axis parallel to the input linear polarization. The loop coupler is polarization maintaining (hi-bi coupler) and one of its axes is parallel to the transmission direction of the linear polarizer, the transmission and the coupling are represented by the Jones matrices $\overleftrightarrow{\tau}$ and $\overleftrightarrow{\kappa}$, respectively. The hi-bi fibers have their birefringence axes parallel to those of the coupler. In the following analysis it is assumed that the hi-bi fibers are ideal, which means that no cross-coupling arises from one birefringence axis to the other, consequently the Jones matrices $\overleftrightarrow{f}_1$ and $\overleftrightarrow{f}_2$ are diagonal. The two quarterwave retarders, represented by the Jones matrices $\overleftrightarrow{q}_1$ and $\overleftrightarrow{q}_2$, have their birefringence axes oriented at 45° with respect to the hi-bi fiber axes. The Jones

matrix $\overleftrightarrow{c}$ of the sensing coil is given in chapter 2, for twisted, spun and helical configurations. Non-reciprocal phase modulation is represented by the phase factor $\exp\{i\phi(t)\}$, the clockwise wave is phase shifted by $\phi(t)$, whereas the counter-clockwise one undergoes a phase shift of $\phi(t+T)$, where T is the time of flight of the light in the Sagnac loop. Truly reciprocal behavior is obtained when the Sagnac loop is configured in reflection, therefore the relevant output of the loop coupler is the port A. Outgoing cross-coupled part, due to the non-ideal elements, is eliminated thanks to the linear polarizer. The interference of the two counter propagating waves is obtained at port A, thus the source coupler has only to couple the intensity of the interference signal toward the reciprocal output port R.

The input Jones vector is parallel to the x reference axis, thus

$$\mathbf{E_i} = \begin{pmatrix} 1 \\ 0 \end{pmatrix}. \tag{4.1.1}$$

The forward and backward Jones matrices of the linear polarizer are

$$\vec{p} = \overleftarrow{p} = p = \begin{pmatrix} 1 & 0 \\ 0 & 0 \end{pmatrix}. \tag{4.1.2}$$

From Fig. 4.1 and taking into account that $\vec{p}\,\mathbf{E_i} = \mathbf{E_i}$ (input linear polarization parallel to the transmission axis of the polarizer), the output Jones vector $\mathbf{E_o}$ becomes

$$\mathbf{E_o} = \overleftarrow{p}[e^{i\phi(t+T)}\vec{\kappa}\,\vec{f}_2\,\vec{q}_2\,\vec{c}\,\vec{q}_1\,\vec{f}_1\,\vec{\tau} + e^{i\phi(t)}\overleftarrow{\tau}\,\overleftarrow{f}_1\,\overleftarrow{q}_1\,\overleftarrow{c}\,\overleftarrow{q}_2\,\overleftarrow{f}_2\,\overleftarrow{\kappa}]\mathbf{E_i}. \tag{4.1.3}$$

The intensity I_o of the output Jones vector is given by

$$I_o = \mathbf{E}_o^{\dagger}\mathbf{E_o}\,, \tag{4.1.4}$$

where $\mathbf{X}^{\dagger}$ is the hermitian conjugate of the Jones vector $\mathbf{X}$. The intensity at the reciprocal output R is half the intensity I_o, due to the source coupler, namely

$$I_R = \frac{1}{2}\mathbf{E}_o^{\dagger}\mathbf{E_o}\,. \tag{4.1.5}$$

The loop coupler is assumed to be loss-free with a coupling ratio of 50 % and to be purely linearly birefringent with no cross-coupling between the two orthogonal birefringence axes, thus

$$\vec{\tau} = \overleftarrow{\tau} = \tau = \frac{1}{\sqrt{2}}\begin{pmatrix} e^{i\phi_\tau/2} & 0 \\ 0 & e^{-i\phi_\tau/2} \end{pmatrix} \quad \text{and} \quad \vec{\kappa} = \overleftarrow{\kappa} = \kappa = \frac{i}{\sqrt{2}}\begin{pmatrix} e^{i\phi_\kappa/2} & 0 \\ 0 & e^{-i\phi_\kappa/2} \end{pmatrix}, \tag{4.1.6}$$

where ϕ_τ and ϕ_κ are the linear retardations of the transmission and the coupling of the coupler, respectively.

The hi-bi fibers, like the coupler, are assumed to present no cross-coupling between the birefringence axes. Their Jones matrices are then

$$\vec{f_j} = \overleftarrow{f_j} = \begin{pmatrix} e^{ik\Delta nL_j/2} & 0 \\ 0 & e^{-ik\Delta nL_j/2} \end{pmatrix} \quad j = 1, 2, \tag{4.1.7}$$

where Δn is the birefringence and L_j the length of the hi-bi fiber.

There are two different possible orientations for the birefringence axes of the quarterwave loops, and therefore two different sets of Jones matrices. This problem is treated in the next section.

4.1.1. Perpendicular and parallel orientation of the quarterwava loops

In the sensing element (fiber coil), the counter-propagating circular polarizations must have the same handedness in order to obtain a cumulative Faraday effect at the Sagnac loop output. This is achieved if the polarization coming from the hi-bi fiber is oriented at 45 ° with respect to the birefringence axes of the quarterwave loop. For ideal quarterwave loops the polarization in the sensing element between them is exactly circular. Therefore the relative rotational orientation of their birefringence axes is not important. This is no longer true if the loops are not ideal, e.g. their linear retardation is different from 90°. In this case the resulting error affecting the Faraday phase recovery depends on the relative orientation of the loops. The effects of non-ideal quarterwave loops will be investigated in Section 4.5 for two different relative orientations of the loops, namely perpendicular and parallel orientation. In this section it will be shown that for perpendicular and parallel orientation the output intensities are the same. This is also true for any other relative orientation of the quarterwave loops.

Perpendicular orientation of the quarterwave loops

Figure 4.2 shows the configuration with perpendicular orientation of the quarterwave loops.

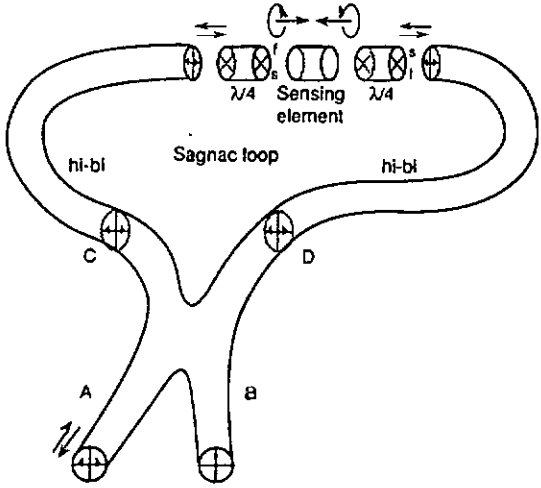

Figure 4.2 Configuration with perpendicular orientation of the quarterwave loops.

In this case the fast axis (f) of one loop is aligned with the slow axis (s) of the other one and conversely. The linear polarizations at the quarterwave loop inputs are aligned in space. In this configuration and in absence of Faraday effect, the two loops are in series and result in a zero birefringence element. The Jones matrices of the coupler and the hi-bi fibers are diagonal. This yields

$$\overleftarrow{p}\,\overrightarrow{\kappa}\,\overrightarrow{f_2} = \frac{i}{\sqrt{2}}\overleftarrow{p}\,e^{i(\phi_\kappa + k\Delta n L_2)/2} \quad , \quad \overleftarrow{p}\,\overleftarrow{\tau}\,\overleftarrow{f_1} = \frac{1}{\sqrt{2}}\overleftarrow{p}\,e^{i(\phi_\tau + k\Delta n L_1)/2} \ ,$$

$$\overrightarrow{f_1}\,\overrightarrow{\tau}\,E_i = \frac{1}{\sqrt{2}}e^{i(\phi_\tau + k\Delta n L_1)/2}E_i \quad \text{and} \quad \overleftarrow{f_2}\,\overleftarrow{\kappa}\,E_i = \frac{i}{\sqrt{2}}e^{i(\phi_\kappa + k\Delta n L_2)/2}E_i \ . \tag{4.1.8}$$

With these conditions Eq. (4.1.3) simplifies to

$$E_o = \frac{i}{2}e^{i[\phi_\tau + \phi_\kappa + k\Delta n(L_1+L_2)]/2}\overleftarrow{p}\,[e^{i\phi(t+T)}\overrightarrow{q_2}\,\overrightarrow{c}\,\overrightarrow{q_1} + e^{i\phi(t)}\overleftarrow{q_1}\,\overleftarrow{c}\,\overleftarrow{q_2}]E_i \ . \tag{4.1.9}$$

This result shows that, thanks to the reciprocity of the Sagnac loop used in reflection, the effects of ideal (no cross-talk) hi-bi fibers and hi-bi coupler result in an isotropic phase factor which will not affect the interference phase (Faraday effect). This clearly appears if one calculates the intensity I_0 based on Eq. (4.1.4) with $|e^{ix}|^2 = 1$. In other words, this phase factor can be omitted, yielding

$$E_o = \frac{1}{2}\overleftarrow{p}\,[e^{i\phi(t+T)}\overrightarrow{q_2}\,\overrightarrow{c}\,\overrightarrow{q_1} + e^{i\phi(t)}\overleftarrow{q_1}\,\overleftarrow{c}\,\overleftarrow{q_2}]E_i \ . \tag{4.1.10}$$

In Eq. (4.1.10) the matrices $\overleftrightarrow{q_j}$ correspond to Jones matrices of quarterwave loops which are not assumed to be ideal, i.e. the retardation is not necessarily 90° and the orientation of the birefringence axes can differ from 45°.

For ideal quarterwave loops, i.e. with 90° of linear retardation and correct orientation, one has

$$\overrightarrow{q_1} = \overleftarrow{q_2} = \frac{1}{\sqrt{2}}\begin{pmatrix} 1 & i \\ i & 1 \end{pmatrix} = q_\perp \quad \text{and} \quad \overleftarrow{q_1} = \overrightarrow{q_2} = \frac{1}{\sqrt{2}}\begin{pmatrix} 1 & -i \\ -i & 1 \end{pmatrix} = q_\perp^{-1} \ . \tag{4.1.11}$$

In this case Eq. (4.1.10) simplifies to

$$E_o = \frac{1}{2}\overleftarrow{p}\,q_\perp^{-1}[e^{i\phi(t+T)}\overrightarrow{c} + e^{i\phi(t)}\overleftarrow{c}\,]\,q_\perp E_i = \frac{1}{2}\overleftarrow{p}\,q_\perp^{-1}\,c(t)\,q_\perp E_i \ , \tag{4.1.12}$$

where the matrix c(t) is defined by

$$c(t) = e^{i\phi(t+T)}\overrightarrow{c} + e^{i\phi(t)}\overleftarrow{c} \ . \tag{4.1.13}$$

c(t) represents the interference of the two counter-propagating waves undergoing Faraday effect in the sensing coil $\overleftrightarrow{c}$ and non-reciprocal phase modulation. In an interference process, the

energy is not conserved if only one output port of the interferometer is considered, therefore the Jones matrix c(t) is not unitary . It can be written as

$$c(t) = \begin{pmatrix} c_{11}(t) & c_{12}(t) \\ c_{21}(t) & c_{22}(t) \end{pmatrix}. \tag{4.1.14}$$

Using Eqs. (4.1.2) and (4.1.11) for $\overleftarrow{p}$ and $q_{\perp}$ respectively, the output Jones vector becomes

$$E_o = \frac{1}{4}\{c_{11}(t) + c_{22}(t) + i[c_{12}(t) - c_{21}(t)]\}\, E_i . \tag{4.1.15}$$

Thus, thanks to the polarizer $\overleftarrow{p}$, the output and the input vectors are colinear.

Parallel orientation of the quarterwave loops

Figure 4.3 shows the configuration with parallel orientation of the quarterwaves loops. In this case the fast/slow axis (f/s) of one loop are aligned to the fast/slow axis (f/s) of the other one. The linear polarizations at the quarterwave loop inputs are perpendicular in space. In this configuration and in absence of Faraday effect, the two loops are in series and are equivalent to a halfwave element.

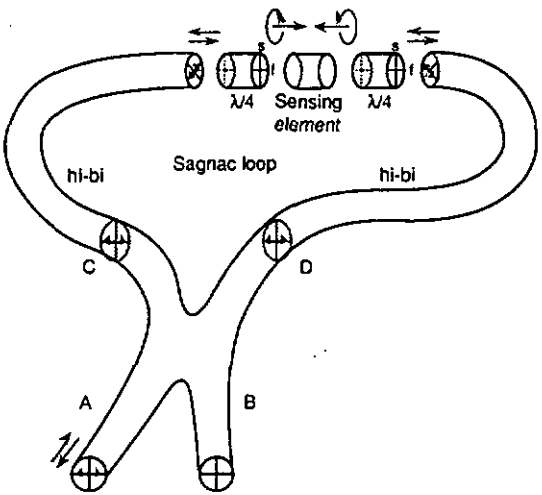

Figure 4.3 Configuration with parallel orientation of the quarterwave loops.

For convenience the birefringence axes of the quarterwave loops are chosen parallel to the directions x and y of the reference frame, as shown in Fig. 4.3. This means that the linear polarizations propagating from ports C and D up to the inputs of the loops must be rotated by 45°. This is achieved by twisting the hi-bi fibers by 45°. Assuming no cross-coupling between the birefringence axes, the Jones matrices of the 45° twisted hi-bi fibers are are given by

$$\vec{f}_1 = \frac{1}{\sqrt{2}}\begin{pmatrix} e^{i\Delta nL_1/2} & -e^{-i\Delta nL_1/2} \\ e^{i\Delta nL_1/2} & e^{-i\Delta nL_1/2} \end{pmatrix} \quad , \quad \overleftarrow{f}_1 = \frac{1}{\sqrt{2}}\begin{pmatrix} e^{i\Delta nL_1/2} & -e^{i\Delta nL_1/2} \\ e^{-i\Delta nL_1/2} & e^{-i\Delta nL_1/2} \end{pmatrix},$$

$$\vec{f}_2 = \frac{1}{\sqrt{2}}\begin{pmatrix} e^{i\Delta nL_2/2} & -e^{i\Delta nL_2/2} \\ e^{-i\Delta nL_2/2} & e^{-i\Delta nL_2/2} \end{pmatrix} \quad \text{and} \quad \overleftarrow{f}_2 = \frac{1}{\sqrt{2}}\begin{pmatrix} e^{i\Delta nL_2/2} & -e^{-i\Delta nL_2/2} \\ e^{i\Delta nL_2/2} & e^{-i\Delta nL_2/2} \end{pmatrix}. \qquad (4.1.16)$$

Taking into account that the Jones matrices of the coupler are diagonal yields

$$\overleftarrow{p}\,\vec{\kappa}\,\vec{f}_2 = \frac{i}{2}e^{i(\phi_\kappa + k\Delta nL_2)/2}\,p' \quad , \quad \overleftarrow{p}\,\overleftarrow{\tau}\,\overleftarrow{f}_1 = \frac{1}{2}e^{i(\phi_\tau + k\Delta nL_1)/2}\,p' \ ,$$

$$\vec{f}_1\,\vec{\tau}\,E_i = \frac{1}{2}e^{i(\phi_\tau + k\Delta nL_1)/2}\,E_i' \quad \text{and} \quad \overleftarrow{f}_2\,\overleftarrow{\kappa}\,E_i = \frac{i}{2}e^{i(\phi_\kappa + k\Delta nL_2)/2}\,E_i' \ , \qquad (4.1.17)$$

where

$$p' = \begin{pmatrix} 1 & -1 \\ 0 & 0 \end{pmatrix} \quad \text{and} \quad E_i' = \begin{pmatrix} 1 \\ 1 \end{pmatrix}. \qquad (4.1.18)$$

With these conditions Eq. (4.1.3) simplifies to

$$E_o = \frac{i}{4}e^{i[\phi_\tau + \phi_\kappa + k\Delta n(L_1+L_2)]/2}\,p'[e^{i\phi(t+T)}\vec{q}_2\,\vec{c}\,\vec{q}_1 + e^{i\phi(t)}\overleftarrow{q}_1\,\overleftarrow{c}\,\overleftarrow{q}_2]E_i' \ . \qquad (4.1.19)$$

Like for the perpendicular configuration, the hi-bi fibers and the coupler introduce an isotropic phase shift which can be omitted, yielding

$$E_o = \frac{1}{4}p'[e^{i\phi(t+T)}\vec{q}_2\,\vec{c}\,\vec{q}_1 + e^{i\phi(t)}\overleftarrow{q}_1\,\overleftarrow{c}\,\overleftarrow{q}_2]E_i' \ . \qquad (4.1.20)$$

In Eq. (4.1.20) the matrices $\overleftrightarrow{q}_j$ correspond to Jones matrices of quarterwave loops which are not assumed to be ideal, i.e. the retardation is not necessarily 90° and the orientation of the birefringence axes with respect to those of the hi-bi fibers can differ from 45°.

For ideal quarterwave loops, i.e. with 90° of linear retardation and correct orientation, one has

$$\vec{q}_j = \overleftarrow{q}_j = \begin{pmatrix} e^{-i\pi/4} & 0 \\ 0 & e^{i\pi/4} \end{pmatrix} = q_{//} \qquad j = 1, 2 \ . \qquad (4.1.21)$$

In this case Eq. (4.1.20) reduces to

$$E_o = \frac{1}{4}p'q_{//}[e^{i\phi(t+T)}\vec{c} + e^{i\phi(t)}\overleftarrow{c}]q_{//}E_i' = \frac{1}{4}p'q_{//}c(t)\,q_{//}E_i' \ , \qquad (4.1.22)$$

where the matrix c(t) is defined by Eq. (4.1.13). Using Eqs. (4.1.18) and (4.1.21) one obtains

$$\mathbf{E_o} = \frac{i}{4}\{c_{11}(t) + c_{22}(t) + i[c_{12}(t) - c_{21}(t)]\}\,\mathbf{E_i}\,. \tag{4.1.23}$$

Equations (4.1.23) and (4.1.15) differ only by a factor i, which means that the output intensities are the same for both parallel and perpendicular configurations. Obviously, this is also true for any other relative orientation of the quarterwave loops.

In conclusion, assuming ideal quarterwave loops, any relative orientation of these loops give rise to the same interference signal I_o, they therefore behave equivalently with respect to the Faraday effect for a given sensing coil configuration.

4.1.2. Ideal fiber coil

An ideal coil is made of fiber which exhibits neither linear nor circular birefringence, the only perturbation the fiber undergoes arises from the Faraday effect. The forward and backward Jones matrices of such a coil are given in section 2.3.2, namely

$$\vec{c} = \begin{pmatrix} \cos\varphi_F & \sin\varphi_F \\ -\sin\varphi_F & \cos\varphi_F \end{pmatrix} \quad \text{and} \quad \overleftarrow{c} = \begin{pmatrix} \cos\varphi_F & -\sin\varphi_F \\ \sin\varphi_F & \cos\varphi_F \end{pmatrix}, \tag{4.1.24}$$

where φ_F = VNI. Using Eq. (4.1.13) one obtains

$$c_{11}(t) = c_{22}(t) = e^{i\bar{\phi}(t)}\,2\cos\varphi_F\cos\frac{\Delta\phi(t)}{2}\,,\quad c_{12}(t) = -c_{21}(t) = ie^{i\bar{\phi}(t)}\,2\sin\varphi_F\sin\frac{\Delta\phi(t)}{2}\,, \tag{4.1.25}$$

where

$$\bar{\phi}(t) = \frac{\phi(t+T) + \phi(t)}{2} \quad \text{and} \quad \Delta\phi(t) = \phi(t+T) - \phi(t)\,. \tag{4.1.26}$$

The output Jones vector is obtained using Eqs. (4.1.15) or (4.1.23), which differ only by a factor i. Further substitution in Eq. (4.1.4) yields the intensity at the reciprocal output, regardless of the configuration type,

$$I_R(t) = \frac{1}{4} + \frac{1}{4}\cos[2\varphi_F + \Delta\phi(t)]\,. \tag{4.1.27}$$

This result is similar to the one obtained for the gyroscope [Eze82], but here the Sagnac phase shift is replaced by the Faraday phase shift. For real fiber coils, the output intensity will no longer correspond to Eq. (4.1.27), as it will be shown in the following.

4.1.3. Coil with mechanically twisted fiber

The Jones matrices in linear polarization basis are given by Eqs. (2.3.23) and (2.3.24). Applying the same procedure as for the ideal fiber coil, one gets for the intensity at the reciprocal output

$$I_R = \frac{1}{8}\cos^2(\gamma d) + \frac{1}{8}\cos^2(\gamma' d) + \frac{1}{8}\left(\frac{VH_z+\delta}{\gamma}\right)^2\sin^2(\gamma d) + \frac{1}{8}\left(\frac{-VH_z+\delta}{\gamma'}\right)^2\sin^2(\gamma' d)$$
$$+\frac{1}{4}\left(\cos(\gamma d)\cos(\gamma' d) + \frac{\delta^2-(VH_z)^2}{\gamma\gamma'}\sin(\gamma d)\sin(\gamma' d)\right)\cos\Delta\phi(t)$$
$$+\frac{1}{4}\left(-\frac{VH_z+\delta}{\gamma}\sin(\gamma d)\cos(\gamma' d) + \frac{-VH_z+\delta}{\gamma'}\sin(\gamma' d)\cos(\gamma d)\right)\sin\Delta\phi(t)\,, \qquad (4.1.28)$$

where $\gamma = [(VH_z+\delta)^2+\eta^2]^{1/2}$ and $\gamma' = [(VH_z-\delta)^2+\eta^2]^{1/2}$. Although Eq. (4.1.28) is more complicated than Eq. (4.1.27), both yield numerical results which are very close to each other as will be shown later. This is the main consequence of the reciprocity of the Sagnac configuration. For large twist rates, i.e. $\delta >> \eta$, Eqs. (4.1.27) and (4.1.28) become identical.

4.1.4. Coil with spun or helical fiber

The Jones matrices in circular polarization basis are given by Eqs. (2.3.27) and (2.3.28). Applying the procedure already used for the ideal fiber coil, one gets for the intensity at the reciprocal output

$$I_R = \frac{1}{8}\cos^2(\gamma d) + \frac{1}{8}\cos^2(\gamma' d) + \frac{1}{8}\left(\frac{VH_z-\alpha}{\gamma}\right)^2\sin^2(\gamma d) + \frac{1}{8}\left(\frac{VH_z+\alpha}{\gamma'}\right)^2\sin^2(\gamma' d)$$
$$+\frac{1}{4}\left(\cos(\gamma d)\cos(\gamma' d) + \frac{\alpha^2-(VH_z)^2}{\gamma\gamma'}\sin(\gamma d)\sin(\gamma' d)\right)\cos\Delta\phi(t)$$
$$+\frac{1}{4}\left(\frac{-VH_z+\alpha}{\gamma}\sin(\gamma d)\cos(\gamma' d) - \frac{VH_z+\delta}{\gamma'}\sin(\gamma' d)\cos(\gamma d)\right)\sin\Delta\phi(t)\,, \qquad (4.1.29)$$

where $\gamma = [(VH_z-\alpha)^2+\eta^2)]^{1/2}$ and $\gamma = [(VH_z+\alpha)^2+\eta^2]^{1/2}$. Like for twisted fiber Eqs. (4.1.27) and (4.1.29) yield numerical results which are very close to each other. For large spin rates, i.e. $\alpha >> \eta$, Eqs. (4.1.27) and (4.1.29) become identical.

4.2. Faraday phase recovery

The Faraday phase shift $2\varphi_F$ is obtained from the detected intensity $I_R(t)$ thanks to the non-reciprocal phase modulation

$$\phi(t) = \phi_0\sin(\omega_m t)\,, \qquad (4.1.30)$$

which yields

$$\Delta\phi(t) = 2\phi_0\sin(\omega_m T/2)\cos[\omega_m(t+T/2)] = \Delta\phi_0\cos[\omega_m(t+T/2)]\,. \qquad (4.1.31)$$

As it will be shown further, ω_m is chosen so that $\omega_m T/2 = \pi/2$; this provides the best immunity to fluctuations of ω_m and T and a minimum for the required amplitude ϕ_0 of the phase modulation.

4.2.1. Ideal fiber coil

In this case the output intensity becomes, using Eqs. (4.1.27) and (4.1.31),

$$I_R(t) = \frac{1}{4}[1 + J_o(\Delta\phi_0)\cos(2\varphi_F)] - \frac{1}{2}\sin(2\varphi_F)\sum_{\mu odd}^{\infty}(-1)^{(\mu+1)/2}J_\mu(\Delta\phi_0)\cos[\mu\omega_m(t+T/2)] + \frac{1}{2}\cos(2\varphi_F)\sum_{\mu even}^{\infty}(-1)^{\mu/2}J_\mu(\Delta\phi_0)\cos[\mu\omega_m(t+T/2)] \; . \tag{4.2.1}$$

To recover the Faraday phase shift, the same signal processing principle as the one used with fiber gyroscopes [Gia82] is applied, namely

$$\varphi_d = \tan^{-1}\left(\frac{J_2(\Delta\phi_0)}{J_1(\Delta\phi_0)}\,\frac{I_R(\omega_m)}{I_R(2\omega_m)}\right), \tag{4.2.2}$$

where φ_d is the detected phase, $I_R(\omega_m)$ and $I_R(2\omega_m)$ are the amplitudes of the components of $I_R(t)$ at ω_m and $2\omega_m$ respectively. For the ideal fiber coil this yields, using Eq. (4.2.1),

$$\varphi_d = 2\varphi_F = 2VNI \; , \tag{4.2.3}$$

which corresponds to an ideal detection of the Faraday effect.

4.2.2. Twisted and spun fiber

The output intensities for mechanically twisted fiber and for spun or helical fiber are given in sections 4.1.3 and 4.1.4. Using Eq. (4.1.31) for $\Delta\phi(t)$ and the definition given above for the detected phase, one gets

$$\varphi_d = \tan^{-1}\left(\frac{\dfrac{VH_z+\xi}{\gamma}\sin(\gamma d)\cos(\gamma' d) + \dfrac{VH_z-\xi}{\gamma'}\sin(\gamma d)\cos(\gamma d)}{\cos(\gamma d)\cos(\gamma' d) + \dfrac{\xi^2-(VH_z)^2}{\gamma\gamma'}\sin(\gamma d)\sin(\gamma' d)}\right), \tag{4.2.4}$$

where $\gamma = [(VH_z+\xi)^2+\eta^2]^{1/2}$ and $\gamma' = [(VH_z-\xi)^2+\eta^2]^{1/2}$, with $\xi = \delta$ for twisted fiber and $\xi = -\alpha$ for spun or helical fiber. For sufficiently large twist or spin rates, i.e. $\delta >> \eta$ or $\alpha >> \eta$, the detection is nearly ideal, namely $\varphi_d \approx 2\varphi_F$. The relative error due to non-ideal fiber coil is defined as

$$\varepsilon_\varphi = \frac{\varphi_d - 2\varphi_F}{2\varphi_F} \; , \tag{4.2.5}$$

where φ_F = VNI. Figure 4.4 shows the relative detected phase error ε_φ versus the Faraday phase φ_F, calculated from Eq. (4.2.4) for a 20 turn twisted fiber coil with a diameter of 2R = 345 mm, a fiber diameter of 2r = 80 μm, a twist rate of T = 10×2π rad/m and a Verdet constant of V = 2.6 μrad/A at λ = 820 nm..

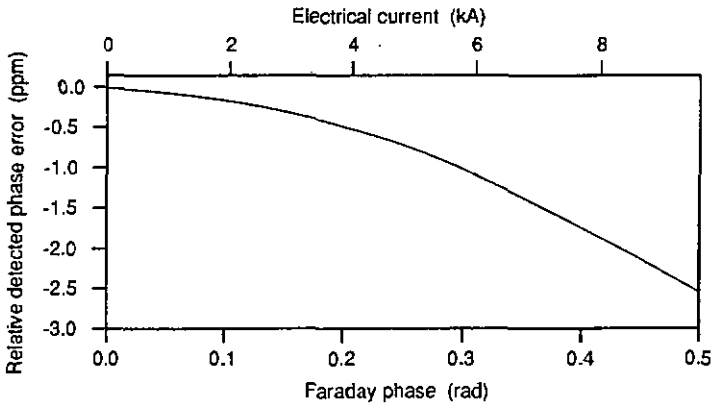

Figure 4.4 Calculated relative phase error versus Faraday phase for the twisted fiber coil.

For this example, the relative detected phase error is smaller than 3 ppm for currents from 0 A up to approximately 10 kA.

In conclusion, the Sagnac configuration used with twisted fiber coil, or with spun or helical fiber coil, permits to measure the Faraday phase shift with negligible error for practical current ranges.

4.3. Source coherence effects

It is well known from the fiber gyroscope, that highly coherent sources are not suited to provide an output signal with high stability. This is in particular due to unavoidable Rayleigh back-scattering, back-reflected light from optical interfaces arising along the optical path, and polarizations cross-coupling in the different elements constituting the Sagnac loop. With a coherent source, all these effects add up coherently at the reciprocal Sagnac interferometer output, resulting in a perturbation of the detected phase.

These effects act similarly when the Sagnac interferometer is used to measure the Faraday effect. However, the problem due to cross-coupled polarizations is more critical in this case, because the Faraday effect, unlike the Sagnac effect, operates on the polarization. Therefore, for stable Faraday effect measurements, it is crucial to use a low coherence source. This results in an incoherent combination of this spurious effects, which does not affect the detected Faraday phase shift. It should be pointed out that perturbing effects due to polarization cross-coupling which result in a balanced optical path for both clockwise and counter-clockwise propagation will not be eliminated by using a low coherence source.

4.4. Temperature effects due to the sensing coil

In practice even high quality silica fibers may contain paramagnetic and ferromagnetic impurities, resulting in a non-zero temperature dependence. Temperature dependance of the Verdet constant for low-birefringence fibers have been reported [Ren89]. It results that some fibers exhibit non-negligible temperature dependence of the Verdet constant, whereas others are not temperature dependent. In the following, the Verdet constant of the fiber is assumed to be temperature independent. The only temperature effects come from the temperature dependence of the bend induced and twist induced linear and circular birefringence. Experimental investigations have shown that the acrilate coating of the fiber has negligible effect in the considered temperature range of –40 °C to 80 °C. In addition it appears that the thermal expansions of the diameter and the length of the fiber can be neglected [Ren88].

The temperature coefficients of bend induced and twist induced birefringences of the LB 600 ultra-low birefringence fiber manufactured by York VSOP (Hampshire, UK), have been measured to be [Ren88]

$$\alpha_\eta = (1/\eta)\frac{d\eta}{dT} = 5.7 \times 10^{-4}\ K^{-1} \quad \text{and} \quad \alpha_\delta = (1/\delta)\frac{d\delta}{dT} = 4.95 \times 10^{-4}\ K^{-1}\ . \tag{4.4.1}$$

The linear and the circular birefringence versus temperature is then

$$\eta(T) = \eta_0[1 + \alpha_\eta(T - T_0)] \quad \text{and} \quad \delta(T) = \delta_0[1 + \alpha_\delta(T - T_0)]\ , \tag{4.4.2}$$

where η_0 and δ_0 are the values of the birefringence at the room temperature $T_0 = 20$ °C. For twisted, and of course bent, fibers ($\xi = \delta$) the detected phase given by Eq. (4.2.4) takes the form

$$\varphi_d(T) = \varphi_d[\eta(T), \delta(T)]\ . \tag{4.4.3}$$

For spun or helical fibers ($\xi = \alpha$) rotational effects are of geometrical type and therefore not temperature dependent. This yields

$$\varphi_d(T) = \varphi_d[\eta(T)]\ . \tag{4.4.4}$$

Here the temperature coefficient α_η depends on the type of the linear birefringence of the considered fiber, e.g. stress induced or form induced birefringence. The relative detected phase error versus temperature is defined as

$$\varepsilon_\varphi(T) = \frac{\varphi_d(T) - 2\varphi_F}{2\varphi_F}\ , \tag{4.4.5}$$

where $\varphi_F = \mathrm{VNI}$. Figure 4.5 shows the relative error $\varepsilon_\varphi(T)$ computed for the same twisted fiber coil as given in section 4.2.2.

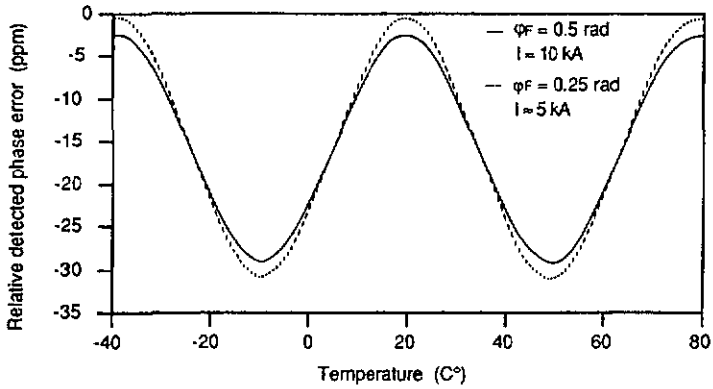

Figure 4.5 Calculated temperature dependence of the relative detected phase error due to the fiber coil. Fiber diameter: $2r = 80$ µm, coil diameter $2R = 345$ mm, twist rate $T = 10 \times 2\pi$ rad/m, number of turns: $N = 20$, Verdet constant = 2.6 µrad/A at $\lambda = 820$ nm.

One sees that $\varepsilon_\varphi(T)$ is almost independent of the Faraday phase shift and is, for this practical example, smaller than 35 ppm. The periodic behavior is due to the terms γd and γd appearing in Eq. (4.2.4), which are approximately equal to $35 \times 2\pi$ and vary by an amount of about $2 \times 2\pi$ between –40 C° and 80 °C. Because γd and γd are arguments of sine and cosine functions in Eq. (4.2.4), $\varepsilon_\varphi(T)$ features a periodic temperature behavior.

It appears from this example that the Sagnac configuration using a twisted fiber coil exhibits temperature variations which are negligible for practical current sensing applications (required minimal error ≤ 0.1 %). This will obviously also be true for spun or helical fiber coils.

4.5. Effects of non-ideal quarterwave loops

The quarterwave loops have to transform the linear polarizations, coming from the hi-bi fibers, into circular polarizations of the same handedness in the sensing coil. Moreover, after having undergone the Faraday effect, the circular polarizations are again transformed into linear polarizations thanks to the quarterwave loops. These transformations of polarization will only be correct if the retardation of the loops is 90° and if the the orientation of their birefringence axes is at 45° with respect to those of the hi-bi fibers. In this section, influences of errors affecting the retardation and the orientation of the quarterwave loops will be theoretically investigated. In the following it is supposed that the only non-ideal elements in the Sagnac interferometer are the quarterwave loops. Cases where the relative orientation of the quarterwave loops is different from 90° (perpendicular configuration) or 0° (parallel configuration) will not be investigated in the following.

4.5.1. Detected Faraday effect

In this section, effects of quarterwave loops with retardation value different from 90° but with correct orientation of the birefringence axes will be studied for both perpendicular and parallel configuration of the quarterwave loops (see section 4.1.1).

Perpendicular orientation of the quarterwave loops

A scheme of this configuration is shown in Fig. 4.2. In this case the Jones matrices of the quarterwave loops, in the linear polarization basis, are

$$\vec{q_1} = \begin{pmatrix} \cos(R_1/2) & i\sin(R_1/2) \\ i\sin(R_1/2) & \cos(R_1/2) \end{pmatrix} \quad , \quad \overleftarrow{q_1} = \begin{pmatrix} \cos(R_1/2) & -i\sin(R_1/2) \\ -i\sin(R_1/2) & \cos(R_1/2) \end{pmatrix},$$

$$\vec{q_2} = \begin{pmatrix} \cos(R_2/2) & -i\sin(R_2/2) \\ -i\sin(R_2/2) & \cos(R_2/2) \end{pmatrix} \quad \text{and} \quad \overleftarrow{q_2} = \begin{pmatrix} \cos(R_2/2) & i\sin(R_2/2) \\ i\sin(R_2/2) & \cos(R_2/2) \end{pmatrix}, \tag{4.5.1}$$

where

$$R_j = \pi/2 + \Delta R_j \qquad j = 1, 2\,. \tag{4.5.2}$$

Replacing into Eq. (4.1.10) one obtains the output Jones vector E_o. The intensity at the reciprocal output is then calculated using Eq. (4.1.5). Finally one gets

$$I_R(t) = [\cos\frac{\Delta\phi(t)}{2}\cos\varphi_F\cos\delta R - \sin\frac{\Delta\phi(t)}{2}\sin\varphi_F\cos\Delta R]^2\,, \tag{4.5.3}$$

where

$$\delta R = \frac{\Delta R_1 - \Delta R_2}{2} \quad \text{and} \quad \Delta R = \frac{\Delta R_1 + \Delta R_2}{2}\,. \tag{4.5.4}$$

δR is representative of the difference between the retardations of the two loops, whereas ΔR represents the mean value of the retardation error. For identical loops one has $\Delta R_1 = \Delta R_2 = \Delta R$ and $\delta R = 0$. The detected phase is obtained from Eq. (4.5.3) using Eqs. (4.1.31) and (4.2.4). This yields

$$\varphi_d = \tan^{-1}\left(\frac{\sin 2\varphi_F\cos\delta R\cos\Delta R}{\cos^2\varphi_F\cos^2\delta R - \sin^2\varphi_F\cos^2\Delta R}\right)\,. \tag{4.5.5}$$

The relative detected phase error is defined as

$$\varepsilon_\varphi = \frac{\varphi_d - 2\varphi_F}{2\varphi_F}\,. \tag{4.5.6}$$

Assuming $\delta R \ll 1$ and $\Delta R \ll 1$ the relative phase error approximates to

$$\varepsilon_\varphi = \frac{\delta R^2 - \Delta R^2}{2} \quad . \tag{4.5.7}$$

For $R_1 = 88°$ and $R_2 = 92°$ this gives $\Delta R = 2° \approx 0.035$ rad, $\delta R = 0°$ and $\varepsilon_\varphi \approx 6.1 \times 10^{-4}$ or 0.61 ‰. This example shows that a retardation error of 2° results in relative detected phase error smaller than 1 ‰, which is acceptable for current sensor applications.

Parallel orientation of the quarterwave loops

A scheme of this configuration is shown in Fig. 4.3. In this case the Jones matrices of the quarterwave loops, in the linear polarization basis, are

$$\vec{q_j} = \overleftarrow{q_j} = \begin{pmatrix} e^{-iR_j/2} & 0 \\ 0 & e^{iR_j/2} \end{pmatrix} \quad j = 1, 2 \,, \tag{4:1.8}$$

where R_j is defined by Eq. (4.5.2). Replacing now into Eq. (4.1.22) and applying the same procedure as for the perpendicular configuration one obtains

$$I_R(t) = [\cos\frac{\Delta\phi(t)}{2}\cos\varphi_F\cos\Delta R - \sin\frac{\Delta\phi(t)}{2}\sin\varphi_F\cos\delta R]^2 \,, \tag{4.5.9}$$

where ΔR and δR are defined in the previous section. If one compares Eqs. (4.5.3) and (4.5.9) it appears that ΔR and δR are reversed.

The detected phase, obtained from Eqs. (4.2.4) and (4.5.9), is

$$\varphi_d = \tan^{-1}\left(\frac{\sin 2\varphi_F \cos\delta R \cos\Delta R}{\cos^2\varphi_F\cos^2\Delta R - \sin^2\varphi_F\cos^2\delta R}\right) . \tag{4.5.10}$$

For $\delta R << 1$ and $\Delta R << 1$ the relative phase error, defined by Eq. (4.5.6), approximates to

$$\varepsilon_\varphi \approx \frac{\Delta R^2 - \delta R^2}{2} \quad . \tag{4.5.11}$$

This relative phase error has the same absolute value as the one obtained for the perpendicular configuration, but with opposite sign. Therefore, regarding the influence of non-ideal quarterwave loops, both perpendicular and parallel configurations behave similarly.

4.5.2. Temperature effects

The quarterwave loops are made of the same ultra-low birefringence fiber type as used for the fiber sensing coil. At a wavelength of $\lambda = 820$ nm, the linear retardation of $R = 90°$ is obtained with a fiber loop diameter of 10 mm for a fiber with a diameter of $2r = 80$ µm. The temperature dependence of the retardation is due only to the bend induced linear birefringence; like for the fiber sensing coil, the coating effects are negligible.

Regardless of the configuration (perpendicular or parallel), the detected phase versus temperature is given by

$$\varphi_d(T) = \varphi_d[\Delta R(T), \delta R(T)] , \tag{4.5.12}$$

where $\varphi_d(\Delta R, \delta R)$ is given by Eqs. (4.5.5) or (4.5.10). $\Delta R(T)$ and $\delta R(T)$ are obtained from the definitions of ΔR and δR and taking into account that the loop retardation is due to the bend induced linear birefringence $\eta(T)$. Thus

$$\Delta R(T) = \Delta R_0 + \frac{R_1 + R_2}{2} \alpha_\eta (T - T_0) \quad \text{and} \quad \delta R(T) = \delta R_0 [1 + \alpha_\eta (T - T_0)] , \tag{4.5.13}$$

where ΔR_0 and δR_0 are the values of $\Delta R(T)$ and $\delta R(T)$ at room temperature T_0 as defined in section 4.5.1. Here R_1 and R_2 are the loop retardations at room temperature. The relative detected phase error $\varepsilon_\varphi(T)$ is obtained from Eq. (4.5.12) and writes

$$\varepsilon_\varphi(T) = [\varphi_d(T) - 2\varphi_F]/2\varphi_F. \tag{4.5.14}$$

Figure 4.6 shows the relative detected phase error versus temperature for the perpendicular configuration, the Faraday phase shift is $\varphi_F = 0.5$ rad corresponding to a current of about 10 kA for a 20 turns fiber coil and a Verdet constant of V = 2.6 μrad/A at λ = 820 nm. One sees that the best temperature behavior, i.e. the smallest relative phase error versus temperature, is achieved for loops with linear retardations of $R_1 = 88°$ and of $R_2 = 92°$, instead of $R_1 = R_2 = 90°$. In this case the maximum error is smaller than 1‰ throughout the considered temperature range. From Fig. 4.6 it also follows that it is important to choose loops having retardations which are *symmetrically distributed about* 90°, e.g. $R_1 = 88°$ and $R_2 = 92°$. *Asymmetrical* distributions of the retardation, e.g. $R_1 = 90°$ and $R_2 = 92°$, give rise to important errors, more than 2 ‰ for the considered example. For the parallel configuration only the sign of the relative error changes compared to the perpendicular configuration.

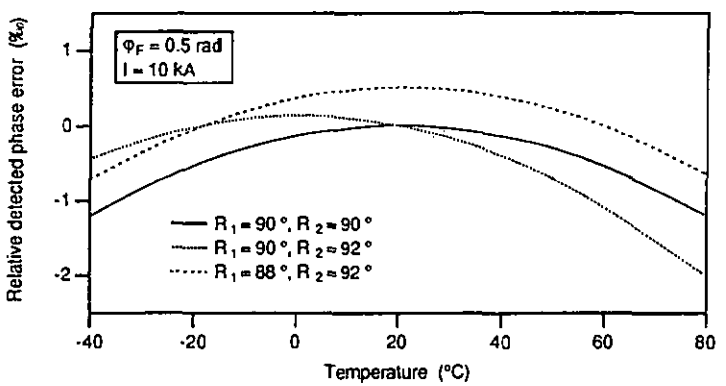

Figure 4.6 Calculated relative detected phase error ε_φ versus temperature, for different values of the loops retardation R_1 and R_2 (given at room temperature) and for a Faraday phase of $\varphi_F = 0.5$ rad *corresponding to a current of about 10 kA for a 20 turns fiber coil and a Verdet constant of* V = 2.6 μrad/A at λ = 820 nm.

The behavior of the relative detected phase error ε_φ versus the Faraday phase is given in Fig. 4.7 for a temperature of T = 80 °C. One sees that ε_φ is approximately independent of the Faraday phase and can be merely evaluated with Eqs. (4.5.7) or (4.5.11).

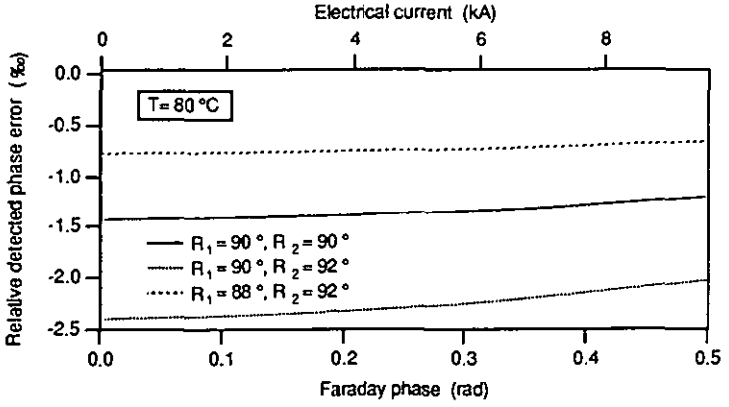

Figure 4.7 Calculated relative detected phase error ε_φ versus Faraday phase at a temperature of T = 80 C° for different values of the loop retardations R_1 and R_2 (given at room temperature).

In conclusion, the use of appropriate quarterwave fiber loops allows to achieve relative detected phase errors smaller than 1 ‰. Therefore, such quarterwave retardation devices are well suited for current sensor applications. Here again, for the parallel configuration only the sign of the relative error changes compared to the perpendicular configuration.

4.5.3. Misalignment effects

In this section the quarterwave loops are assumed to be ideal, i.e. both have a linear retardation of 90°. Moreover, the birefringence axes of both loops are assumed to be perfectly aligned with respect to each other. In practice this condition can be easily fulfilled, because the birefringence axes lie in the planes containing the loop and perpendicular to the loop. Therefore, in the perpendicular configuration both loops are placed in perpendicular planes, whereas in the parallel one they are in the same plane. However, the linear polarizations coming from the hi-bi fibers could have an alignment error which will affect the detected phase. This misalignment is due to a non-correct orientation of the birefringence axes of the hi-bi fibers with respect to those of the quarterwave loops. In this section, the influence of the misalignment of the birefringence axes of the hi-bi fibers will be investigated for both perpendicular and parallel configurations.

Perpendicular orientation of the quarterwave loops

For the ideal case, as shown in Fig. 4.2, the birefringence axes of the hi-bi fiber are aligned with respect to each other and are at 45° with respect to those of the quarterwave loops. Moreover, the birefringence axes of the hi-bi fiber are parallel to the directions x (horizontal) and y (vertical) of the reference frame. For the non-ideal case, the axes of the hi-bi fibers are no longer aligned to the x and y directions, this means that the fibers are now slightly rotated. Let

$\Delta\theta_1$ and $\Delta\theta_2$ be the alignment errors of the birefringence axes at each hi-bi fiber end next to the quarterwave loops. Thus the Jones matrices of the rotated hi-bi fibers are

$$\vec{f}_1 = \begin{pmatrix} \cos\Delta\theta_1 e^{ik\Delta nL_1/2} & -\sin\Delta\theta_1 e^{-ik\Delta nL_1/2} \\ \sin\Delta\theta_1 e^{ik\Delta nL_1/2} & \cos\Delta\theta_1 e^{-ik\Delta nL_1/2} \end{pmatrix} \quad \overleftarrow{f}_1 = \vec{f}_1\wedge,$$

$$\vec{f}_2 = \begin{pmatrix} \cos\Delta\theta_2 e^{ik\Delta nL_2/2} & -\sin\Delta\theta_2 e^{ik\Delta nL_2/2} \\ \sin\Delta\theta_2 e^{-ik\Delta nL_2/2} & \cos\Delta\theta_2 e^{-ik\Delta nL_2/2} \end{pmatrix} \quad \overleftarrow{f}_2 = \vec{f}_2\wedge. \tag{4.5.15}$$

For ideal alignment, i.e. $\Delta\theta_1 = 0$ and $\Delta\theta_2 = 0$, the above matrices reduce to those given by Eq. (4.1.7). To calculate the output Jones vector $\mathbf{E}_0$ one has to start from Eq. (4.1.3). Using the matrices given by (4.5.15) one finds, like in Section 4.1.1, that the linear retardation of the hi-bi fibers amounts to an isotropic phase factor which can be omitted. For the output intensity one gets finally

$$I_R(t) = [\cos\frac{\Delta\phi(t)}{2}\cos\varphi_F\cos\Delta\theta - \sin\frac{\Delta\phi(t)}{2}\sin\varphi_F\cos\delta\theta]^2 , \tag{4.5.16}$$

where

$$\Delta\theta = \Delta\theta_1 + \Delta\theta_2 \quad \text{and} \quad \delta\theta = \Delta\theta_1 - \Delta\theta_2 . \tag{4.5.17}$$

From the definition of the detected phase given by Eq. (4.2.2), one gets

$$\varphi_d = \tan^{-1}\left(\frac{\sin 2\varphi_F\cos\delta\theta\cos\Delta\theta}{\cos^2\varphi_F\cos^2\Delta\theta - \sin^2\varphi_F\cos^2\delta\theta}\right) . \tag{4.5.18}$$

The relative error ε_φ is defined by Eq. (4.5.6). Assuming $\Delta\theta << 1$ and $\delta\theta << 1$ one has

$$\varepsilon_\varphi \approx \frac{\Delta\theta^2 - \delta\theta^2}{2} . \tag{4.5.19}$$

For $\Delta\theta_1 = \Delta\theta_2 = 1°$ this gives $\Delta\theta \approx 2° \approx 0.035$ rad, $\delta\theta \approx 0°$ and $\varepsilon_\varphi \approx 6.1 \times 10^{-4}$ or 0.61 ‰. This example shows that an alignment error of 1° induces a relative detected phase error smaller than 1 ‰, which is acceptable for current sensing applications.

Parallel orientation of the quarterwave loops

For the ideal case, as shown in Fig. 4.3, the birefringence axes of the hi-bi fiber are perpendicular with respect to each other and are at 45° with respect to those of the quarterwave loops. Moreover, for convenience, the birefringence axes of the loops are parallel to the directions x (horizontal) and y (vertical) of the reference frame. For the non-ideal case, the axes of the hi-bi fibers are no longer at 45° with respect to the x and y directions, this means that the hi-bi fibers are now slightly rotated. The angles of the hi-bi fibers axes with respect to the x direction are

$$\theta_1 = 45° + \Delta\theta_1 \quad \text{and} \quad \Delta\theta_2 = 45° + \Delta\theta_2 \,. \tag{4.5.20}$$

For ideal alignment one has $\Delta\theta_1 = \Delta\theta_2 = 0°$, giving $\theta_1 = \theta_2 = 45°$. The Jones matrices of the rotated hi-bi fibers are given by (4.5.15), where $\Delta\theta_i$ is replaced by θ_i. As for the perpendicular configuration, the linear retardation of the hi-bi fibers results in an isotropic phase factor which can be omitted in the expression for the output Jones vector $\mathbf{E}_o$. For the output intensity one gets finally

$$I_R(t) = [\cos\frac{\Delta\phi(t)}{2}\cos\varphi_F\cos\delta\theta - \sin\frac{\Delta\phi(t)}{2}\sin\varphi_F\cos\Delta\theta]^2 \,. \tag{4.5.21}$$

The detected phase is obtained with the same procedure as for the perpendicular configuration. Thus

$$\varphi_d = \tan^{-1}\left(\frac{\sin 2\varphi_F\cos\delta\theta\cos\Delta\theta}{\cos^2\varphi_F\cos^2\delta\theta - \sin^2\varphi_F\cos^2\Delta\theta}\right) \,. \tag{4.5.22}$$

The relative error ε_φ is defined by Eq. (4.5.6). Assuming $\Delta\theta << 1$ and $\delta\theta << 1$ one has

$$\varepsilon_\varphi \approx \frac{\delta\theta^2 - \Delta\theta^2}{2} \,. \tag{4.5.23}$$

This relative phase error has the same absolute value as for the perpendicular configuration, but opposite sign. Therefore, considering the influence of the non-ideal alignment of the quarterwave loops, both perpendicular and parallel configurations may be regarded as equivalent.

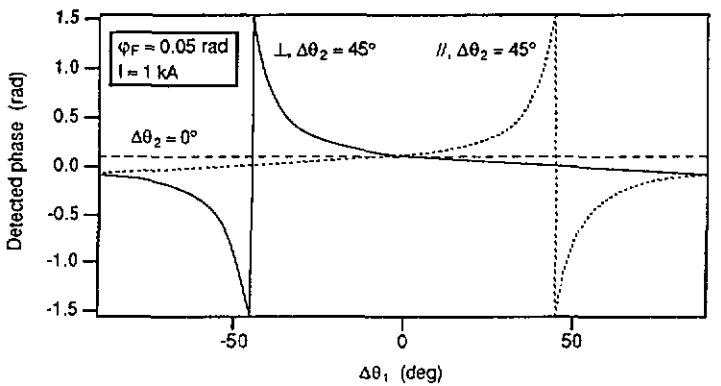

Figure 4.8 Calculated phase error versus alignment error $\Delta\theta_1$ for fixed $\Delta\theta_2$ and for a constant Faraday effect of $\varphi_F = 0.05$ rad, corresponding to a current of about 1 kA for a 20 turn fiber sensing coil with a Verdet constant of V = 2.6 μrad/A at λ = 820 nm.

Figure 4.8 shows the behavior of the detected phase φ_d for a constant Faraday effect of $\varphi_F = 0.05$ rad versus the misalignment error $\Delta\theta_1$, for both perpendicular and parallel configurations. The horizontal line ($\Delta\theta_2 = 0°$) corresponds to the correct value of the detected phase. It appears that if one of the quarterwave loops is correctly aligned ($\Delta\theta_1 = 0°$ or $\Delta\theta_2 = 0°$) the detected phase error is zero independently of the orientation of the other loop. However, for such a case the amplitude of the interference signal drops, which results in a poorer signal to noise ratio and therefore in a higher detected phase noise. The equivalent behavior of the perpendicular and the parallel configuration is clearly evidenced in Fig. 4.8; they are symmetrical with respect to the alignment errors.

4.6. All-Fiber Sagnac current sensor

The purpose of this section is to demonstrate a practical realization of the all-fiber Sagnac current sensor described in Section 3.2.1. Both reciprocal and non-reciprocal outputs will be investigated. For the interpretation of the experimental results, the theory developed in the previous sections of chapter 4 will be used.

4.6.1. Summary

An all-fiber Sagnac current sensor has been realized and successfully tested. All-fiber optical elements have been used throughout, namely pigtailed laser diodes, polarization maintaining fibers, all-fiber retardation plates, etc. The sensing coil is a 10 turn helix of 30 mm diameter and 520 mm length. This coil is connected to the ground, where all the electronic parts of the sensor are located, by two 20 m long linear polarization maintaining fibers. The Faraday phase is measured by using non-reciprocal phase modulation and coherent detection. The current sensor has been investigated using both the reciprocal and the non-reciprocal output of the Sagnac interferometer. Perfect linearity between the detected Faraday phase shift and the 175 Hz ac current was measured from 0.1 A to 100 A. For both outputs the sensitivity and the accuracy were essentially limited by the detector noise. Shot-noise limited detection was not yet achieved due to lack of optical power. At the reciprocal output the detected power was 135 nW and the electronic noise was equivalent to a phase noise of 60 μrad/√Hz or a current noise of 1 A/√Hz for a 10 turn helical coil. At the non-reciprocal output the detected power was 760 nW and the electronic noise was equivalent to a phase noise of 10 μrad/√Hz or a current noise of 0.17 A/√Hz for a 10 turn helical coil.

4.6.2. Principles and signal processing

The minimum reciprocal configuration described in Section 3.2.1 will be used. The sensing coil is a 10 turn helix with the same characteristics as the one described in Section 3.1.1. As already shown from theoretical and experimental results in Section 3.1, the helical coil can be considered as nearly ideal. The other elements constituting the Sagnac interferometer are also assumed to be ideal for a first analysis. The effects of the non-ideal elements will be briefly discussed later.

Taking into account the above assumptions, the non-reciprocal phase induced by the Faraday effect is

$$\varphi(t) = 2\varphi_F(t) = 2VNI(t)\,. \tag{4.6.1}$$

For the ideal fiber coil the detected intensity at the reciprocal output is then given by Eq. (4.1.27), which yields for the detected signal voltage

$$u_r(t) = u_{r0}\{1 + \cos[\varphi(t) + \Delta\phi(t)]\}\,, \tag{4.6.2}$$

where $\Delta\phi(t)$ is the non-reciprocal phase modulation, defined in Section 4.2, namely $\Delta\phi(t) = 2\phi_0\sin(\omega_m T/2)\cos[\omega_m(t + T/2)] = \Delta\phi_0\cos[\omega_m(t + T/2)]$, where $\omega_m/2\pi = f_m$ is the frequency modulation. At the non-reciprocal output the detected signal voltage is [Eze82, Ulr82]

$$u_{nr}(t) = u_{nr0}\{1 - \cos[\varphi(t) + \Delta\phi(t)]\}\,. \tag{4.6.3}$$

The non-reciprocal phase $\varphi(t)$ is retrieved using coherent detection [Hay82]. For that purpose the detected signal is band-pass filtered in order to get the component at ω_m. As a consequence of Eq. (4.2.1) the filtered signal is of the form

$$u(t) = \pm 2u_0 J_1(\Delta\phi_0)\sin\varphi(t)\cos[\omega_m(t + T/2)]\,, \tag{4.6.4}$$

where the plus sign holds for the reciprocal and the minus sign for the non-reciprocal output, respectively. To perform the coherent detection, this signal is multiplied by a reference signal $u_{ref}(t)$ and then low-pass filtered. The reference signal is

$$u_{ref}(t) = u_{ref0}\sin(\omega_m t + \Phi_{ref})\,, \tag{4.6.5}$$

where Φ_{ref} is a constant phase shift. The signal at the low-pass filter output is then

$$U(t) = \pm U_0 J_1(\Delta\phi_0)\sin\varphi(t)\sin(\Phi_{ref} - \omega_m T/2). \tag{4.6.6}$$

Adjusting Φ_F so that $\Phi_{ref} - \omega_m T/2 = \pi/2$, the output signal becomes

$$U(t) = \pm U_0 J_1(\Delta\phi_0)\sin\varphi(t)\,. \tag{4.6.7}$$

For small values of the Faraday effect ($\varphi(t) << 1$, i.e. $I \le 1$kA for a 10 turn helical coil and $\lambda = 780$ nm) one can assume that $\sin\varphi(t) \approx \varphi(t)$. Maximum sensitivity is obtained for $J_1(\Delta\phi_0) = \max$, i.e. for $\Delta\phi_0 = 1.8$ with $J_1(\Delta\phi_0) \approx 0.58$. Moreover, the sensitivity to fluctuations of $\Delta\phi_0 = 2\phi_0\sin(\omega_m T/2)$ vanishes if one works at the maximum of J_1, which provides immunity against variations of ϕ_0, ω_m and T. For $\omega_m T/2 = \pi/2$ the required phase modulation ϕ_0 is minimum and the immunity of the demodulated signal against fluctuations of ω_m and T is even further improved. Using $T = nL/c$ one gets for the optimum length of the Sagnac loop

$$L = c/2nf_m. \tag{4.6.8}$$

In our experiment the modulation frequency imposed by the all-fiber modulator was $f_m = 930$ kHz. With $n = 1.5$ one gets from Eq. (4.6.8) $L = 107$ m for the optimal length. However, for practical reasons the fiber loop length was only 55 m, which yields $\sin(\omega_m T/2) \approx 0.7$. Nevertheless it is always possible to fulfill the condition $\Delta\phi_0 = 1.8$ ($J_1(\Delta\phi_0)$ maximum) by increasing ϕ_0.

4.6.3. Effects of non-ideal elements

The helical coil

An ideal helical coil [May89] has degenerated eigenpolarizations in absence of the Faraday effect. This is no longer true in presence of the Faraday effect. However, for practical values of the current to be measured ($I \leq 20$ kA for a 10 turn helical coil) the eigenpolarizations will remain close to purely circular polarizations, permitting optimum detection of the Faraday effect. For a non-ideal helical coil, coupling between eigenpolarizations (of the ideal helical coil) arises. The coupled part is not transmitted by the polarizer (P) and therefore does not disturb the Faraday effect measurement at the reciprocal output. However, this non-ideal behavior of the helical coil will slightly change the sensitivity to the Faraday effect of the measured non-reciprocal phase shift. In our experiment the helical coil has a total linear retardation which is below 1°. This means that this helical coil is close to an ideal one, leading to negligible perturbation for the measured Faraday effect. This is particularly true for the Sagnac interferometer, where perturbing reciprocal effects are strongly attenuated when detecting the Faraday effect at the reciprocal output.

All-fiber quarterwave plates

The all-fiber quarterwave plates [Fro89] are formed by a fiber loop compressed between two rigid plates, the retardation value can be adjusted by varying the compression force. The aim of these all-fiber quarterwave plates is to convert the two counter propagating linear polarizations from the hi-bi fiber into circular polarizations for the helical coil Faraday sensor. Non-ideal behavior of the quarterwave plates gives rise to not exactly circular polarizations entering the helical coil, resulting in a change of the sensitivity for the Faraday effect measured from the non-reciprocal phase shift. The light leaving the helical coil will not be transformed in a perfectly linear polarization after the non-ideal quarterwave plate. This means that a certain amount of light will be present in the wrong linear polarization of the hi-bi fiber. However, this part is not accepted by the polarizer (P) at the reciprocal Sagnac interferometer output, and therefore does not disturb the Faraday phase measurement. In our experiment it was possible to approach very closely the ideal value of the all-fiber quarterwave plates and thus minimizing the unwanted effects due to non-ideal behavior.

The hi-bi fiber

An ideal hi-bi fiber maintains linear polarization launched parallel to one of the birefringence axes. In real hi-bi fibers [Kam81, Kam82], randomly distributed perturbations along the fiber length give rise to cross-coupling between the two linear eigenpolarizations and therefore the linear input polarization is no longer maintained. In our Sagnac interferometer the light coupled into the wrong linear polarization is not accepted by the polarizer (P) and therefore does not disturb the Faraday phase measurement at the reciprocal output. However, if light in the wrong

polarization is already present at the hi-bi fiber input, due to non-ideal helical coil or quarter-wave plates, it can be cross-coupled during the propagation in the hi-bi fiber. This coupled light, accepted by the polarizer (P), depends also on the Faraday effect and will therefore perturb the measurement at the reciprocal output. For our hi-bi fiber (York HB 750) the average cross-coupled power after 10 m is about 0.1 ‰ of the input power, corresponding to a extinction ratio of –20 dB over 1 km measured with a low coherence source. Each piece of hi-bi fiber is 20 m long and gives therefore 0.2 ‰ of cross-coupled power. For 20 m hi-bi fiber and assuming that the non-ideal helical coil and the quarterwave plates produce about 1 % of the total power in the wrong polarization, only 0.002 ‰ of the total output power will perturb the measurement of the Faraday effect at the reciprocal output. This error may drift slowly with time, following the environmental conditions. In our experiments a low coherence source of about $\Delta\lambda = 3$ nm was used, which yields a coherence length of 200 μm, so that the counter propagating cross-coupled light beams will not interfere. The result is a negligible phase error for the measured Faraday effect.

The polarization maintaining coupler

In an ideal polarization maintaining coupler, linear polarization launched parallel to one of the birefringence axes is maintained. In a real polarization maintaining coupler, the output polarization is no longer the same as the input polarization, it contains a certain amount of the orthogonal component. The effects are essentially the same as those due to the non-ideal hi-bi fiber. However, the cross-coupled power is about two orders of magnitude higher for the polarization maintaining coupler. As already mentioned for the hi-bi fiber, this error drifts slowly with time according to the environmental conditions. If the coherence of the source is low, as in our experiment, the resulting phase error is still negligible for the measured Faraday effect.

The phase modulator

The all-fiber phase modulator consists of 10 turns of hi-bi fiber wound around a piezoceramic (PZT) cylinder of 32 mm diameter. The intrinsic birefringence in the hi-bi fiber is about 400 times larger than the bend induced birefringence. Thus the linear polarizations of the hi-bi fiber are maintained, even if the axis of the bend induced birefringence and the intrinsic birefringence are not aligned. This has been confirmed experimentally.

The non-reciprocal output

There are two contributions to the difference between the reciprocal and the non-reciprocal output, namely the cross-coupled polarization in the Sagnac loop and the non-reciprocal behavior of the polarization maintaining coupler (PMC). The cross-coupled part has undergone the Faraday effect and depends on the environmental conditions and therefore fluctuates with time. Fortunately this cross-coupled part can be eliminated by inserting a linear polarizer at the non-reciprocal output. The polarization maintaining coupler (PMC) produces a dc non-reciprocal optical phase shift at the non-reciprocal output, this phase is small ($\leq$ 10 mrad) and drifts slowly. It is impossible to eliminate this contribution. However, for ac detection this additional dc phase is not relevant.

4.6.4. Noise limitations

The smallest measurable phase depends on the signal-to-noise ratio at the detection. The noise is a combination of shot-noise, due to the optical detection, and electronic noise.

Detection noise

The detected signal voltage is given by Eq. (4.2.1). The electrical power spectrum at the detection consists of the detected signal power and the detection noise, as shown in Fig. 4.9. It is assumed that $\varphi << 1$, i.e. $\sin\varphi \approx \varphi$ and $\cos\varphi \approx 1$.

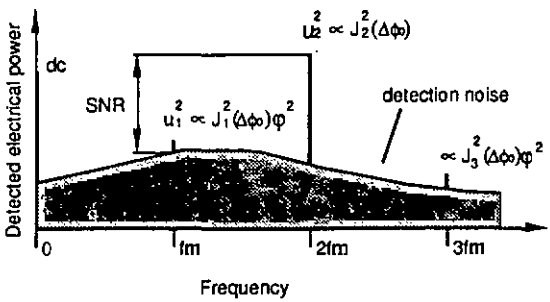

Figure 4.9 Power spectrum at the detection.

The components at ω_m ($\omega_m = 2\pi f_m$) and $2\omega_m$ of the detected signal u(t) ($u_r(t)$ or $u_{nr}(t)$) are given by

$$u(\omega_m) = \pm 2u_0\varphi(t)J_1(\Delta\phi_0)\cos[\omega_m(t+T/2)] \qquad (4.6.9\ a)$$

$$u(2\omega_m) = \mp 2u_0J_2(\Delta\phi_0)\cos[2\omega_m(t+T/2)]\ . \qquad (4.6.9\ b)$$

In our experiment, the current is a harmonic function of time with the frequency $\Omega/2\pi$, which gives for the Faraday phase

$$\varphi(t) = \sqrt{2}\varphi\sin\Omega t, \qquad (4.6.10)$$

where φ is the rms value of $\varphi(t)$ and $\Omega << \omega_m$. Calculating the rms value of $u(\omega_m)$ and $u(2\omega_m)$ one gets

$$u_1 = \sqrt{2}u_0\varphi J_1(\Delta\phi_0) \qquad (4.6.11)$$

and

$$u_2 = \sqrt{2}u_0J_2(\Delta\phi_0)\ . \qquad (4.6.12)$$

Since it is more reliable to determine u_2 from the detected spectrum than to measure u_0 from the dc level under the same conditions as u_1, it is convenient to replace u_0 in Eq. (4.6.11) by Eq. (4.6.12), which yields

$$u_1 = \frac{J_1(\Delta\phi_0)}{J_2(\Delta\phi_0)}\varphi u_2. \tag{4.6.13}$$

The minimum detectable phase φ_{min} corresponds to the case where the component at f_m of the detected signal is equal to the noise at the same frequency f_m, i.e. $u_1 = u_{1n}$. From Eq. (4.6.13) one gets then for the minimum detectable phase

$$\varphi_{min} = \frac{J_2(\Delta\phi_0)}{J_1(\Delta\phi_0)}\frac{u_{1n}}{u_2} = \frac{J_2(\Delta\phi_0)}{J_1(\Delta\phi_0)}\,SNR^{-1/2}, \tag{4.6.14}$$

where $SNR = u_2^2/u_{1n}^2$ is defined as the ratio of the detected electrical power at $2f_m$(independent of φ for $\varphi << 1$) and the electrical noise power at f_m for the relevant detection bandwidth B for the phase measurement. Figure 4.9 shows how u_1, u_2 and the SNR can be measured using a spectrum analyzer.

Shot-noise

The shot-noise u_{sn} is proportional to the average detected optical power P_{opt}, i.e. to the mean value $\langle u\rangle$ of the detected signal. The signal to noise ratio for shot-noise limited detection is given by

$$SNR_{sn} = \frac{\eta P_{opt}}{2B\hbar\nu} = \langle u\rangle^2/u_{sn}^2, \tag{4.6.15}$$

where η is the quantum efficiency of the detector, P_{opt} the mean detected power, B the detection bandwidth and u_{sn}^2 the electrical power of the shot-noise. Using Eq. (4.2.1) and assuming that $\varphi << 1$ one gets

$$\langle u\rangle = u_o[1\pm J_o(\Delta\phi_0)], \tag{4.6.16}$$

From Eqs. (4.6.15) and (4.6.16) one obtains then

$$u_{sn} = u_o[1\pm J_o(\Delta\phi_0)]SNR_{sn}^{-1/2}. \tag{4.6.17}$$

The minimum detectable phase corresponds to the case where $u_1 = u_{sn}$. Combining Eqs. (4.6.11), (4.6.12) and (4.6.16) one gets

$$\varphi_{min} = \frac{1 \pm J_0(\Delta\phi_0)}{\sqrt{2}J_1(\Delta\phi_0)}\,SNR_{sn}^{-1/2}, \tag{4.6.18}$$

where $\pm$ stands for the reciprocal and the non-reciprocal output, respectively.

Residual non-reciprocal phase

As previously stated, non-ideal elements result in an unwanted residual non-reciprocal phase at both reciprocal and non-reciprocal output. This residual phase $\delta\varphi$ can be determined from the measured spectrum for zero current ($H_z = 0$). Assuming that $\delta\varphi << 1$ and that P_1 and P_2 is the electrical power of the detected signal at f_m and $2f_m$, respectively, and using Eq. (4.2.1) one gets

$$\delta\varphi = \frac{J_2(\eta)}{J1(\eta)} \sqrt{\frac{P_1}{P_2}}. \tag{4.6.19}$$

4.6.5. Experimental results

Experimental set-up

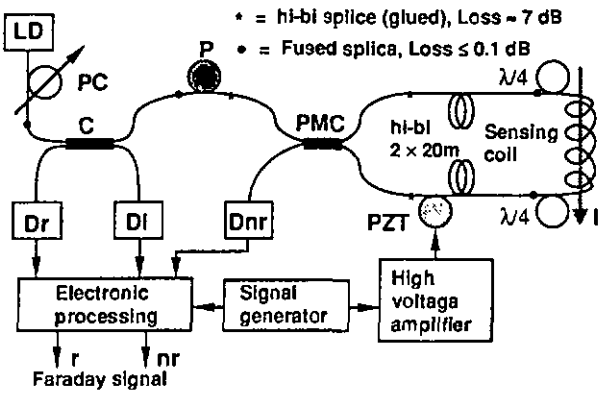

Figure 4.10 Experimental set-up. LD: pigtailed laser diode (λ = 786 nm, multimode), PC: all-fiber polarization controller, C: coupler, P: all-fiber polarizer, PMC: polarization maintaining coupler, D_r: detector at reciprocal output, D_i: optical intensity detector, D_{nr}: detector at non-reciprocal output, PZT: piezoceramic all-fiber phase modulator, $\lambda/4$: all-fiber quarterwave retarder.

Figure 4.10 shows the optical set-up. The Faraday signal at the reciprocal (r) and the non-reciprocal (nr) outputs is proportional to the non-reciprocal phase φ. As explained below, coherent detection is used to recover the phase φ. Both reciprocal and non-reciprocal outputs were measured. The coherent demodulation is achieved by a mixer which is followed by a lock-in amplifier for the low-pass filtering. In order to compensate the fluctuations of the laser intensity, the lock-in amplifier normalizes the output signal to its auxiliary input by the signal supplied by D_i, which is proportional to the laser intensity. The readout and the analog output are proportional to φ.

Faraday effect measurement

The Faraday phase φ was measured at both the reciprocal and the non-reciprocal output. The loss of the glued hi-bi splices is about 50%, thus the opdcal power at the reciprocal output is much lower than at the non-reciprocal output, namely 135 nW versus 760 nW. At both outputs the shot-noise limited condition was not achieved. The electronic noise is composed essendally of the Johnson noise from the feedback resistor (transimpedance amplifier) and the voltage noise from the operadonal amplifier. Table 4.1 gives the minimum detectable phase φ_{min}, deduced from Eq. (4.6.14), and the measured SNR at each output. Theoretical values of φ_{min} corresponding to shot-noise limited detection are also given, using Eq. (4.6.18) with $\Delta\phi_0 = 1.8$ and $\eta = 0.88$ for a silicon photodiode. For each value of φ_{min} the corresponding current has been calculated using $I_{min} = \varphi_{min}/2VN$, with V = 3 μrad/A (λ = 780 nm) and N = 10 turns.

B = 1 Hz	a) Measured	b) Shot-noise limited
Reciprocal output	SNR = 78 dB	SNR_{sn} = 113.7 dB
P_{opt} = 135 nW	φ_{min} = 64 μrad I_{min} = 1.1 A	φ_{min} = 3.3 μrad I_{min} = 0.05 A
Non-reciprocal output	SNR = 91 dB	SNR_{sn} = 121.2 dB
P_{opt} = 760 nW	φ_{min} = 14 μrad I_{min} = 0.24 A	φ_{min} = 0.7 μrad I_{min} = 0.012 A

Table 4.1 Minimum detectable phase φ_{min} and current I_{min} for 1 Hz detection bandwidth. a) Deduced from the measured SNR. b) Deduced from the calculated SNR_{sn} for shot-noise limited detection.

The minimum detectable phase corresponds to the noise level at the demodulated output. Direct measurement of this noise has been performed for both reciprocal and non-reciprocal outputs, a lock-in amplifier with 1 Hz detection bandwidth has been used. Table 4:2 shows the value φ_n of the phase equivalent noise measured at the demodulator output, and the value of φ_{min} obtained from measured SNR. Table 4.2 shows that the values obtained from the SNR are in good agreement with those measured at the demodulator output.

B = 1 Hz	a) Noise measurement	b) Calculated from measured SNR
Reciprocal output P_{opt} = 135 nW	φ_n = 60 μrad I_n = 1 A	φ_{min} = 64 μrad I_{min} = 1.1 A
Non-reciprocal output P_{opt} = 760 nW	φ_n = 10 μrad I_n = 0.17 A	φ_{min} = 14 μrad I_{min} = 0.24 A

Table 4.2 Minimum detectable phase and current for 1 Hz detection bandwidth. a) Noise measured at demodulator output. b) Calculated from the measured SNR.

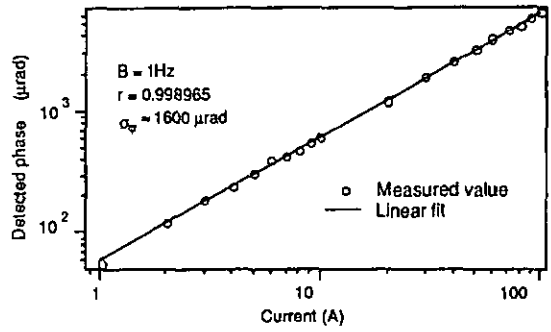

Figure 4.11 Measured Faraday phase versus electrical current at reciprocal output.

Figure 4.11 shows the measured Faraday phase φ versus the ac current I at 175 Hz for a detection bandwidth of B = 1 Hz. A linear fit to the measured values yields the standard deviation σ_φ and the correlation coefficient r. The rms phase error $\delta\varphi$ is obtained from $\delta\varphi = \sigma_\varphi\sqrt{1-r^2}$. Table 4.3 gives the values of the rms phase error $\delta\varphi$ and the measured phase noise φ_n at the demodulator output.

B = 1 Hz	a) rms phase error	b) Noise measurement
Reciprocal output P_{opt} = 135 nW	$\delta\varphi$ = 75 µrad I_n = 1.25 A	φ_n = 60 µrad I_n = 1 A
Non-reciprocal output P_{opt} = 760 nW	$\delta\varphi$ = 8 µrad I_n = 0.13 A	φ_n = 10 µrad I_n = 0.17 A

Table 4.3 Minimum detectable phase φ and current I for 1 Hz detection bandwidth. a) rms phase error obtained from the linear fit, b) Noise measurement at demodulator output.

Table 4.3 shows that the error of the measured phase φ is essentially due to the noise at the demodulator output, i.e. $\delta\varphi \approx \varphi_n$ for both the reciprocal and the non-reciprocal output.

Temperature dependence

A variation of 5 °C around room temperature results in a change of about 25 % of the Faraday signal at both the reciprocal and the non-reciprocal output. The main effect of the temperature is to couple intensity of the principal polarization into the orthogonal one, resulting in a reduction of the Faraday signal. An efficient way to compensate this reduction would be to normalize the Faraday signal to the optical output intensity of the principal polarization. Qualitative investigations of the sensitivity of the Faraday signal to changes of the temperature of individual elements have been performed. One element at a time was heated at a temperature of about 50 °C. The list of the elements in decreasing order of sensitivity to temperature reads: the electronics, in particular the mixers; the PZT phase modulator, the hi-bi fiber and PMC; the all-fiber quarterwave retarder; the helical coil.

Mechanical perturbations

The same type of Sagnac current sensor was previously realized with bulk optical elements. For both the bulk and the all-fiber version, measurements of the sensitivity of the Faraday signal to mechanical perturbations have been performed. The sensor was mechanically perturbed by hitting the hi-bi fiber, the helical coil, etc, and by strongly whistling. For all these perturbations the all-fiber version was about 100 times less sensitive than the bulk one, confirming the absolute necessity to use an all-fiber version for industrial applications.

Long term stability

For constant room temperature, measurements over 15 hours show that the Faraday signal remains perfectly constant for both the reciprocal and the non-reciprocal output.

Simplified all-fiber Sagnac current sensor

As previously stated, the cross-coupled polarization in the Sagnac loop gives rise to a fluctuation of the signal at the non-reciprocal output. We have measured the dc fluctuations of the Faraday signal at the non-reciprocal output for zero current. Without polarizer at the non-reciprocal output, the measured dc fluctuations were about 5 mrad, which corresponds to a dc current of 80 A. With a linear polarizer aligned parallel to the principal polarization, the dc fluctuations drop approximately by a factor 100, corresponding to 50 μrad or 0.8 A. This confirms the necessity of having a linear polarizer aligned to the principal polarization at the non-reciprocal output, particularly for dc detection of the Faraday effect. These results show that for ac measurement of the Faraday effect the non-reciprocal output can be used without loss of accuracy. Therefore the first coupler C in Fig. 4.10 can be removed, resulting in a gain of a factor 2 for the detected optical power.

4.6.6. Conclusions

An all-fiber Sagnac current sensor has been demonstrated. The principal difficulty was to control in a perfect manner the polarization of the light at each point of the interferometer. For this purpose, elements such as polarization maintaining couplers, hi-bi fibers, all-fiber polarization controllers, all-fiber polarizers and a helical fiber sensing coil have been used. The Faraday phase is measured in the same manner as in standard fiber optic gyroscopes, i.e. by non-reciprocal phase modulation and coherent detection. The reported work permits to point out most of the fundamental problems inherent to the Sagnac interferometer used as a Faraday current sensor. As an important result we found that for ac current detection the non-reciprocal output of the Sagnac interferometer can be used without drift problems. This leads to a simplified all-fiber Sagnac current sensor with only one fiber coupler. It has also been demonstrated that the mechanical stability increases approximately by two orders of magnitude for the all-fiber version of the Sagnac current sensor compared to the bulk version. Additional investigations will be necessary to localize and to solve the problems of the stability with respect to temperature.

4.7. All-fiber Sagnac current sensor based on a commercial fiber optic gyroscope

In this section a current sensor based on a modified commercial fiber gyro is described and characterized. Influence of the temperature and of the alignment between the hi-bi fibers and the quarterwave loops will be measured and then compared with the theory previously developed.

4.7.1. Summary

An all-fiber Sagnac current sensor based on a commercial fiber optic gyroscope has been realized and tested. A 20 turn fiber coil with a diameter of 2R = 345 mm is used. The ultra-low birefringence fiber, which has a diameter of 2r = 80 μm, is mechanically twisted at the rate of 10 turns/m. The same fiber was used for the quarterwave loops. The polarization maintaining fiber of the gyroscope, which is 100 m long, was cut in the middle of its length and then spliced at each quarterwave loop. Perfect linearity between the detected Faraday phase shift and the 75 Hz ac current was measured from 10 A to 800 A. The detected phase noise amounts to about 10 μrad/√Hz, which is equivalent to a detected current noise of 0.1 A/√Hz.

4.7.2. Experimantal set-up and signal processing

The experimental set-up of the all-fiber Sagnac current sensor, which consists of a modified fiber gyroscope, is shown in Fig. 4.12.

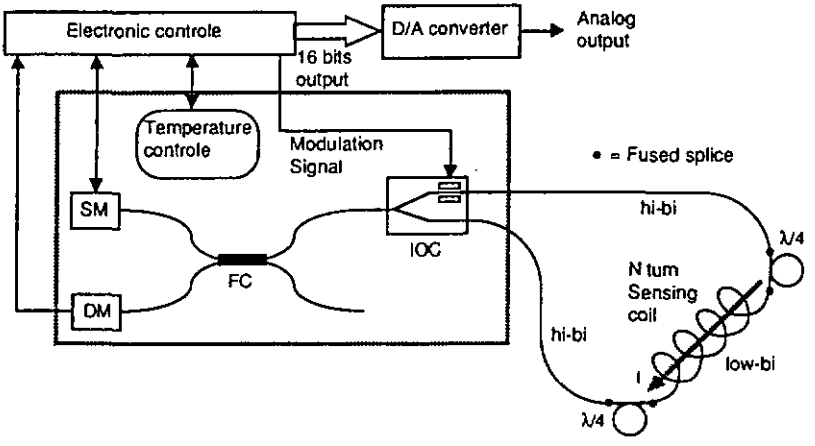

Figure 4.12 Fiber gyroscope converted to an all-fiber Sagnac current sensor. SM: source module, DM: detector module, FC: fused coupler, IOC: integrated optic Y-coupler.

The sensing coil is made of 20 turns of ultra-low birefringence fiber (York LB 800) which is mechanically twisted at the rate of 10 turns/m. The diameter of the fiber is 80 μm. The total length of the fiber constituting the coil is approximately 20 m. The birefringence of the whole fiber coil was measured to be approximately 2°. The quarterwave loops are made of the same fiber type as the one used for the sensing coil. The loop diameter is adjusted so that the retardation is 90° with a precision of about 1 %. The fiber is confined in a 1 mm circular slit in a 15 mm × 15 mm piece of aluminum. The slit filled with a soft UV-curred glue. The parallel configuration has been chosen, this means that the birefringence axes of the quarterwave loops are aligned. The hi-bi fiber of the gyroscope was cut in the middle of its length and then 10 m shortened at each extremity in order to compensate the length of fiber coil to get an optimal non-reciprocal phase modulation. This phase modulation is produced by the integrated optic Y-coupler (IOC) which contains in one of its arms an integrated optic phase modulator. The frequency modulation is about 1 MHz. The total length of the fiber forming the Sagnac loop is 100 m, namely 80 m of hi-bi fiber belonging to the original gyroscope and 20 m of low-bi fiber constituting the quarterwave loops and the sensing coil. The extremities of the hi-bi fibers next to the loops are fixed in such a way that they can be slightly twisted, this permit to adjust precisely the orientation of the hi-bi fiber birefringence axes with respect to those of the quarterwave loops. As a practical consequence, the fused splices between the hi-bi fibers and the loops need no more to be oriented which simplifies the splicing procedure. The electronic control module which is supplied with the gyroscope provides a digital output signal of 16 bits with a sampling rate of 1 kHz. A D/A converter transforms the 16 bit signal into an output voltage which is proportional to the non-reciprocal phase shift in the Sagnac loop. The assumptions concerning the elements of the sensor are the same as those given in Section 4.6. Therefore the detected phase induced by the Faraday effect is given by Eq. (4.6.1), namely $\varphi(t) = 2VNI(t)$. The detected interference signal is given by Eq. (4.6.2). The detected phase retrieval is performed by the digital signal processing unit in the electronic control module and is given by Eq. (4.2.2), namely $\varphi_d = \tan^{-1}\{J_2(\Delta\phi_0)I_R(\omega_m)/J_1(\Delta\phi_0)I_R(2\omega_m)\}$. The effects related to non-ideal elements have also been developed in Section 4.6.

4.7.3. Measurement of the Faraday effect

According to the data sheet, the principal characteristics of the fiber gyroscope are:

Sensitivity:	50 $degh^{-1}$/LSB (at the 16 bit digital output),
Output noise:	10 $degh^{-1}/\sqrt{Hz}$ or 0.2 LSB/$\sqrt{Hz}$,

where LSB stands for least significant bit in the digital output. Other parameters of the original gyroscope are 100 m fiber length, 68 mm coil diameter, 820 nm wavelength and about 20 μW optical power output. Experimental investigations have confirmed the above data for the sensitivity and the noise. The manufacturer indicates that the detection is rather limited by electronic noise than by the shot-noise.

The characteristics of the D/A converter module are 91.6 μV/LSB convertion ratio and a frequency response of 200 Hz at –3 dB. The additional noise due the D/A module is negligible. The sensitivity to the rotation rate at the D/A output was measured to be $S_\Omega = 6.68$ mV/deg·s^{-1}. This sensitivity can be converted into current sensitivity via the Faraday effect; for a 20 turn sensing coil and a Verdet constant of V = 2.6 μrad/A at 820 nm this yields $S_I = 0.234$ mV/A.

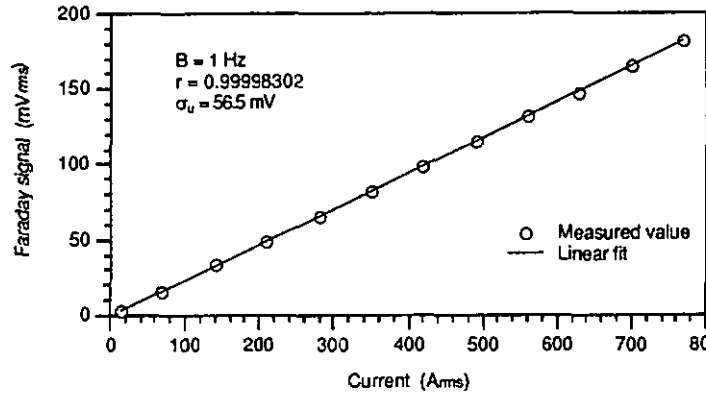

Figure 4.13 Output voltage, proportional to the Faraday effect, versus electrical current.

Figure 4.13 shows the measured Faraday signal versus the 75 Hz ac electrical current, measured with a FFT spectrum analyzer at 1 Hz detection bandwidth. The detected optical power at the output is approximately 7 μW, which means that the losses due to the four splices amount approximately to 5 dB. The output noise is now about 0.4 LSB/√Hz, which corresponds to approximately 0.1 A/√Hz for a 20 turn coil and a Verdet constant of V = 2.6 μrad/A at a wavelength of λ = 820 nm. Therefore, the additional losses due to the modifications of the gyroscope result in an increase of the equivalent output phase noise by a factor of 2. The measured slope, or the sensitivity, is measured to be $S_I = 0.236$ mV/A, which is in good agreement with the expected value of $S_I = 0.234$ mV/A. A linear fit to the measured values yields the standard deviation σ_u and the correlation coefficient r. The rms voltage error δu is obtained from $\delta u = \sigma_u\sqrt{1-r^2}$. From the measured values one gets $\delta u \approx 0.33$ mV, which corresponds to a rms current error of $\delta I \approx 1.4$ A. This is much larger than the equivalent current noise of 0.1 A for 1 Hz detection bandwidth. This discrepancy may be attributed to the reading error of the amperemeter, which has 1500 A full scale and 1 % maximum error specified by the manufacturer.

4.7.4. Measurement of the influence of the temperature

The retardation and the position of the birefringence axes of the quarterwave loops have been measured between 0 C° and 80°C. The results are shown in Fig. 4.14. From the linear fit one obtains the temperature sensitivity of the retardation for the loops, namely $\Delta R/\Delta T = 0.0035°/°C$ for the first loop and $\Delta R/\Delta T = 0.0061°/°C$ for the second one. The temperature coefficient is given by $\alpha_R = (\Delta R/\Delta T)/R$. With $R = 90°$ this yields $\alpha_{R1} = 3.9 \times 10^{-4}\ K^{-1}$ and $\alpha_{R2} = 6.8 \times 10^{-4}\ K^{-1}$, which is in good agreement with the value given for purely bend induced birefringence, namely $\alpha_\eta = 5.7 \times 10^{-4}\ K^{-1}$ (see Section 4.4). The differences are probably due to uncontrolled influence of the fiber coating and the glue in the loops. In Section 4.5.2 it has been established that for quarterwave loop retardation errors $\leq 2°$ the resulting detected phase error in the considered temperature range (-40 °C to 80 °C) does not exceed 2 ‰. Moreover,

one sees from Fig. 4.14 that the orientation of the birefringence axes can vary up to 1°, this results, as it has been shown in Section 4.5.3, in detected phase errors in the order of 0.5 ‰.

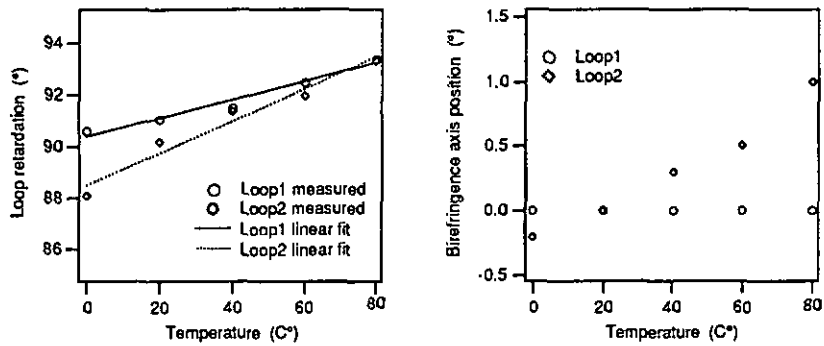

Figure 4.14 Loop retardation and birefringence axes position versus temperature.

In Section 4.4 the detected error due to the fiber sensing coil was shown to be smaller than 0.035 ‰ for the same temperature range. In the worst case the above errors add up, this gives a theoretically estimated detected phase error of less than 2.5 ‰. The measured relative phase error versus temperature is shown in Table 4.4. From 20 °C to 80 °C it is smaller than 2 ‰, which is in agreement with the theoretical prediction. However, for temperatures smaller than 20 °C the relative error becomes much larger (10 times) than theoretically expected. Experimental investigations have shown that the glue points used for the construction of the fiber coil can introduce unwanted and uncontrolled birefringent retardations larger than 10°. Moreover, the fiber coating can be an important source of additional birefringence at low temperature.

Temperature	0 °C	20 °C	40 °C	60 °C	80 °C
Relative phase error	2.3 %	≤ 2 ‰	≤ 2 ‰	≤ 2 ‰	≤ 2 ‰

Table 4.4 Relative detected phase error versus temperature.

4.7.5. Influence of the alignment between the hi-bi fibers and the quarter-wave loops

The influence of the alignment error of the birefringence axes of the hi-bi fiber has been theoretically investigated in Section 4.5.3. For the parallel configuration the detected phase is given by Eq. (4.5.22). The output voltage, which is proportional to the detected phase, versus the alignment error $\Delta\theta_1$ of one of the hi-bi fiber ends has been measured for constant orientation $\Delta\theta_2$ of the other fiber extremity. The experimental results and the theoretical values obtained from Eq. (4.5.22) are compared in Fig. 4.16. Two situations are investigated. First, one of the two loops is correctly oriented ($\Delta\theta_2 = 0°$). In this case the theory predicts that the

detected phase is independent of the orientation error $\Delta\theta_1$ and corresponds exactly to twice the Faraday phase shift ($2\varphi_F$). This is confirmed by the experimental results. The small discrepancy between the theory and the measurements may be attributed to a non-ideal alignment of the fixed extremity, i.e. $\Delta\theta_2$ differs slightly from zero. Second, the fixed hi-bi fiber extremity has a misalignment error of $\Delta\theta_2 = 45°$. Figure 4.16 confirms the good agreement between the theory and the measurements.

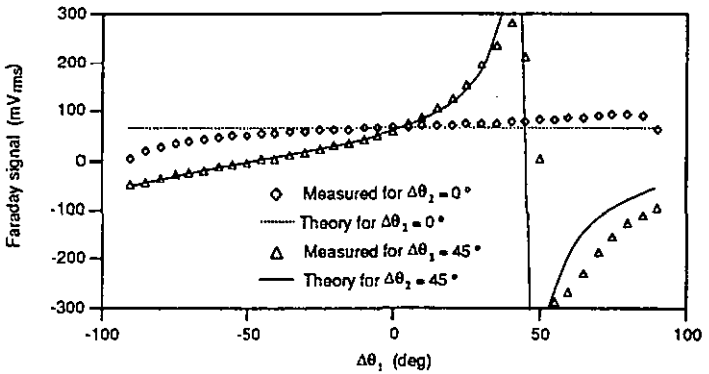

Figure 4.16 Output voltage versus hi-bi fiber alignment error $\Delta\theta_1$ (extremity next to the first loop) for constant $\Delta\theta_2$ (extremity next to the second loop) and for a Faraday phase shift of $\varphi_F = 0.0206$ rad (280 A_{rms} for a 20 turn fiber coil and V = 2.6 µrad/A at λ = 820 nm).

5. THE RECIPROCAL REFLECTION INTERFEROMETER WITH FARADAY EFFECT

This chapter reports the detailed theoretical and experimental investigations of the reflection interferometer used to detect the Faraday effect. In Section 5.1 the detected intensity will be derived for the general case, i.e. regardless to the used fiber configuration for the sensing coil. The influence of the source coherence is taken into account in this analysis. In Section 5.2 these results will be applied to the different fiber configurations, namely the mechanically twisted fiber, the spun fiber and the helical fiber. The effects of non-ideal quarterwave loop are also analyzed. The reflection interferometer with internal non-reciprocal phase modulation is reported in Section 5.3. The analysis of the effects of the non-ideal elements and of the temperature are presented in Sections 5.4 and 5.5. Experimental results are reported in Section 5.6 and 5.7.

5.1. Detected intensity and effects of the coherence of the source for general fiber configuration

The principle of the reciprocal reflection interferometer for the Faraday effect detection is shown in Fig. 3.6. For convenience a bloc-diagram representation will be used for the theoretical analysis, as shown in Fig. 5.1.

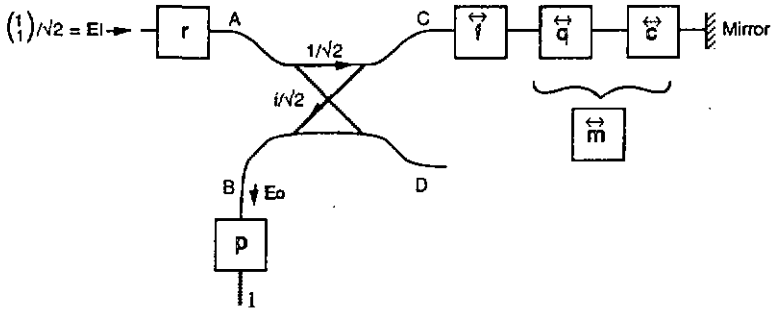

Figure 5.1 Bloc-diagram representation of the reflection interferometer used to detect the Faraday effect.

Each bloc corresponds to a Jones matrix of an individual element constituting the reflection interferometer. Except for the sensing coil, which has circular birefringence, the elements of the interferometer are linearly birefringent, thus the linear polarization basis is more suited for the calculation. The input linear polarization, which is represented by the Jones vector $\mathbf{E}_i$, is oriented at 45° with respect to the reference frame (x,y,z) defined in Section 2.2. As explained in Section 3.2.2 the 45° linear input polarization has to be seen rather like the superposition of two in phase linear polarizations parallel to the x (horizontal) and y (vertical) reference axes.

The notation used for forward and backward propagation has been defined in Section 4.1. The input linear retarder r has its birefringence axes aligned to the x and y directions. As will be shown later, this linear retarder is necessary to obtain the quadrature condition for the output interference signal. The coupler is assumed not to affect the polarization, this means that the transmission and the coupling are given by the factors $1/\sqrt{2}$ and $i/\sqrt{2}$, respectively. However, in practice this condition is only partially fulfilled. The hi-bi fiber has its birefringence axes parallel to the x and y reference axes. In the following analysis it is assumed that the hi-bi fiber is ideal, this means that no cross-coupling arises from one birefringence axis to the other, thus its Jones matrix $\overleftrightarrow{f}$ is diagonal. The quarterwave retarder, represented by the Jones matrix $\overleftrightarrow{q}$, has its birefringence axes oriented at 45° with respect to the hi-bi fibers axes. The Jones matrix $\overleftrightarrow{c}$ of the sensing coil is given in Chapter 2 for twisted, spun and helical configurations. The mirror is characterized by its reflection Jones matrix s. The output Jones vector $\mathbf{E}_0$ can also be seen as the superposition of two nearly linear orthogonal polarizations, each corresponding to the horizontal and vertical input polarizations. Therefore, a linear polarizer has to be used in order to obtain the interference between them. This interference can also be achieved using a Wollaston prism. This permits to obtain an output signal which is insensitive to the variations of the optical power, launching efficiency, etc. In the following analysis, only detection with a linear polarizer (p) will be investigated. This is sufficient to point out the most interesting properties of the reflection interferometer.

5.1.1. Detected Intensity

The input Jones vector, corresponding to a linear polarization at 45° with respect the x and y axes, writes

$$\mathbf{E}_i = \frac{1}{\sqrt{2}}\begin{pmatrix}1\\1\end{pmatrix}. \tag{5.1.1}$$

To compare the backward travelling output wave with the forward travelling input wave correctly, a second reflection matrix s has to be introduced [Dän92]. Based on Fig. 5.1, the resulting output Jones vector is then

$$\mathbf{E}_0 = \frac{i}{2}\, s\, \overleftarrow{f}\, \overleftarrow{m}\, s\, \overrightarrow{m}\, \overrightarrow{f}\, r\, \mathbf{E}_i\,, \tag{5.1.2}$$

where

$$\overrightarrow{m} = \overrightarrow{c}\,\overrightarrow{q} \quad \text{and} \quad \overleftarrow{m} = \overleftarrow{q}\,\overleftarrow{c}\,. \tag{5.1.3}$$

The reflection matrix, expressed in the linear polarization basis, is of the form

$$s = \begin{pmatrix}-1 & 0\\ 0 & 1\end{pmatrix}. \tag{5.1.4}$$

The forward and backward Jones matrices of the hi-bi fiber are

$$\vec{f} = \overleftarrow{f} = f = \begin{pmatrix} e^{ik\Delta nL/2} & 0 \\ 0 & e^{-ik\Delta nL/2} \end{pmatrix}, \tag{5.1.5}$$

where Δn is the birefringence and L the length of the hi-bi fiber. Taking into account that s and f are diagonal, Eq. (5.1.2) modifies to

$$E_o = \frac{i}{2} f s \overleftarrow{m} s \vec{m} f r E_i = \frac{i}{2} f m f r E_i , \tag{5.1.6}$$

with

$$m = s \overleftarrow{m} s \vec{m} = \begin{pmatrix} m_a & -m_b^* \\ m_b & m_a^* \end{pmatrix}. \tag{5.1.7}$$

The matrix m contains the effects of the sensing coil $\overleftrightarrow{c}$ and the quarterwave loop $\overleftrightarrow{q}$. As it will be shown further, for ideal optical elements m_a vanishes and $m_b = ie^{i2\varphi_F}$. This means that m_a represents the polarization coupling due to non-ideal optical elements. The Jones matrix of the linear retarder, which has its birefringence axes aligned to the directions x and y, is given by

$$r = \begin{pmatrix} e^{i\phi_r/2} & 0 \\ 0 & e^{-i\phi_r/2} \end{pmatrix}, \tag{5.1.8}$$

where ϕ_r is the linear retardation. Using Eq. (5.1.6) and the explicit expressions for the matrices quoted above, the output Jones vector writes

$$E_o = \frac{i}{2\sqrt{2}} \begin{pmatrix} m_a e^{i(k\Delta nL+\phi_r/2)} - m_b^* e^{-i\phi_r/2} \\ m_a^* e^{-i(k\Delta nL+\phi_r/2)} + m_b e^{i\phi_r/2} \end{pmatrix}. \tag{5.1.9}$$

For ideal elements, namely non-birefringent fiber sensing coil (see Eq. (2.3.13)) and ideal quarterwave loop (see Eq. (4.1.11), the matrix element m_a vanishes and the output Jones vector becomes

$$E_o = \begin{pmatrix} -m_b^* e^{-i\phi_r/2} \\ m_b e^{i\phi_r/2} \end{pmatrix} = -m_b^* e^{-i\phi_r/2} \begin{pmatrix} 1 \\ 0 \end{pmatrix} + m_b e^{i\phi_r/2} \begin{pmatrix} 0 \\ 1 \end{pmatrix}. \tag{5.1.10}$$

This particular case shows clearly that the two input linear orthogonal polarizations result into two output linear orthogonal polarizations. Thus, in order to recover the Faraday effect, which is contained in the matrix element m_b, it is necessary that these two orthogonal output polarizations interfere. That can be obtained by a linear polarizer.

This linear polarizer has its transmission axis aligned at 45° with respect to the x reference axis, thus its Jones matrix is

$$p = \frac{1}{2}\begin{pmatrix} 1 & 1 \\ 1 & 1 \end{pmatrix}. \tag{5.1.11}$$

Using Eq. (5.1.9) one has for the Jones vector E after the polarizer

$$E = p\,E_o = \frac{i}{2}\left[Re\left\{m_a e^{i(k\Delta nL+\phi_r/2)}\right\} + i\,Im\left\{m_b e^{i\phi_r/2}\right\}\right]E_i = VE_i\,. \tag{5.1.12}$$

One sees that the output polarization is parallel to the input polarization, owing to the polarizer, but with a complex amplitude V resulting from the interference of the two output orthogonal polarizations, as explained above. This complex amplitude V depends on the optical path difference $k\Delta nL$ of the hi-bi fiber and contains information about the Faraday effect through the matrix elements m_a and m_b.

Taking into account that $I_i = E_i^{\dagger}E_i = 1$, the detected intensity I of the Jones vector E is given by

$$I = E^{\dagger}E = \frac{1}{4}\left[Re^{\,2}\left\{m_a e^{i(k\Delta nL+\phi_r/2)}\right\} + Im^{\,2}\left\{m_b e^{i\phi_r/2}\right\}\right]. \tag{5.1.13}$$

For ideal optical elements the matrix element m_a vanishes and the detected intensity becomes

$$I = \frac{1}{4}Im^{\,2}\left\{m_b e^{i\phi_r/2}\right\}. \tag{5.1.14}$$

For non-ideal optical elements m_a, which represent the unwanted cross-coupling, is different from zero. It appears then clearly from Eq. (5.1.13) that the optical path difference ΔnL of the hi-bi fiber will be a perturbing term. Generally, $k\Delta nL$ is larger than $1000 \times 2\pi$ rad and is strongly dependent of the external conditions, e.g. temperature. This cross-coupled part will therefore perturb the Faraday phase detection. The interference of the cross-coupled light is eliminated when the coherence length of the light is shorter than the path difference of the two polarization modes in the hi-bi fiber. For this reason, the influence of the source coherence will be investigated in the next chapter.

5.1.2. Influence of the source coherence

The source is now non-monochromatic, however it is assumed that we are still in a quasi-monochromatic situation. Therefore the power spectrum of the source covers a frequency range $\Delta\nu$ which is small compared with the mean frequency ν_0 [Bor59]. From Eq. (5.1.12) and using the relation $k\Delta nL = 2\pi\nu(\tau_x - \tau_y) = -2\pi\nu\tau$, where τ_x and τ_y are the group delays for the two polarization modes of the hi-bi fiber and ν is the optical frequency, the Jones vector E at the frequency ν becomes

$$E = \frac{i}{2}\left[Re\left\{m_a(\nu)e^{i(-2\pi\nu\tau+\phi_r(\nu)/2)}\right\} + i\,Im\left\{m_b(\nu)e^{i\phi_r(\nu)/2}\right\}\right]E_i\,. \tag{5.1.15}$$

where $m_a(\nu)$, $m_b(\nu)$ and $\phi_r(\nu)$ represent the matrix elements m_a, m_b and the retardation ϕ_r at the optical frequency ν. For non-monochromatic light, the input Jones vector E_i has to be replaced by

$$\mathbf{E_i}(t) = V(t)\mathbf{E_i}\,, \tag{5.1.16}$$

where $V(t)$ is the analytic signal associated to the real input wave $V_r(t)$ [Bor59]. That is

$$V(t) = V_r(t) + iV_i(t) = 2\int_0^\infty \hat{V}(\nu)\, e^{-i2\pi\nu t}\, d\nu\,, \tag{5.1.17}$$

where $\hat{V}(\nu)$ the Fourier transform of the real amplitude $V_r(t) = Re\,\{V(t)\}$, namely

$$\hat{V}(\nu) = \int_{-\infty}^{\infty} V_r(t)\, e^{i2\pi\nu t}\, dt\,. \tag{5.1.18}$$

The real part $V_r(t)$ and the imaginary part $V_i(t) = Im\,\{V(t)\}$ may be shown to be Hilbert transforms of each other [Bor59]. For the time averaged intensity of $E_i(t)$ one has

$$< I_i(t) > = < \mathbf{E_i^\dagger}(t)\,\mathbf{E_i}(t) > = 1\,, \tag{5.1.19}$$

where $< x(t) >$ denotes the time average of $x(t)$. Thus, the analytic signal satisfies

$$< |V(t)|^2 > = 1. \tag{5.1.20}$$

The Jones vector $E(t)$ for non-monochromatic light is then obtained from Eq. (5.1.15) in the form of

$$\mathbf{E}(t) = U(t)\mathbf{E_i}\,, \tag{5.1.21}$$

where $U(t)$ is the analytic signal associated to the output wave (after the polarizer). Using Eqs. (5.1.15) and (5.1.17) the output analytic signal becomes

$$U(t) = 2\int_0^\infty \frac{i}{2}\left[Re\,\{m_a(\nu)e^{i(-2\pi\nu\tau+\phi_r(\nu)/2)}\} + iIm\,\{m_b(\nu)e^{i\phi_r(\nu)/2}\}\right]\hat{V}(\nu)\, e^{-i2\pi\nu t}\, d\nu\,. \tag{5.1.22}$$

The loop retardation, the birefringence properties and the Verdet constant of the sensing coil remain approximately constant for wavelength variations of a few nanometers. Therefore, for quasi-monochromatic light, i.e. for a spectral bandwidth of a few nanometers, the approximations $m_a(\nu) \approx m_a(\nu_0)$, $m_b(\nu) \approx m_b(\nu_0)$ and $\phi_r(\nu) \approx \phi_r(\nu_0)$ can be used. Thus, using $Re\,\{x\} = (x + x^*)/2$, Eq. (5.1.22) modifies to

$$U(t) = \frac{i}{4} m_a(\nu_0) e^{i\phi_r(\nu_0)/2} 2\int_0^\infty \hat{V}(\nu) e^{-i2\pi\nu(t+\tau)} d\nu$$

$$+ \frac{i}{4} m_a^*(\nu_0) e^{-i\phi_r(\nu_0)/2} 2\int_0^\infty \hat{V}(\nu) e^{-i2\pi\nu(t-\tau)} d\nu$$

$$+ \frac{i}{2} Im\{m_b(\nu_0) e^{i\phi_r(\nu_0)/2}\} 2\int_0^\infty \hat{V}(\nu) e^{-i2\pi\nu t} d\nu . \qquad (5.1.23)$$

Finally one gets

$$U(t) = \frac{i}{4} m_a(\nu_0) e^{i\phi_r(\nu_0)/2} V(t+\tau) + \frac{i}{4} m_a^*(\nu_0) e^{-i\phi_r(\nu_0)/2} V(t-\tau)$$

$$- \frac{1}{2} Im\{m_b(\nu_0) e^{i\phi_r(\nu_0)/2}\} V(t) . \qquad (5.1.24)$$

The time averaged output intensity is obtained using Eq. (5.1.21) as

$$< I(t) > = < E^\dagger(t) E(t) > = < U(t)^* U(t) E_i^\dagger(t)\, E_i(t) > = < U(t)^* U(t) > . \qquad (5.1.25)$$

This result depends on the coherence of the light. The complex degree of coherence is defined as [Bor59]

$$\gamma(T) = \frac{< V(t+T) V^*(t) >}{< V(t) V^*(t) >} = |\gamma(T)| e^{-i2\pi\nu_0 T} . \qquad (5.1.26)$$

Using Eqs. (5.1.24) to (5.1.26) one gets

$$I = \frac{1}{8} |m_a(\nu_0)|^2 + \frac{1}{4} Im^2\{m_b(\nu_0) e^{i\phi_r(\nu_0)/2}\}$$

$$+ \frac{1}{8} |\gamma(2\tau)| Re\{m_a^2(\nu_0) e^{i[\phi_r(\nu_0) - 2\pi\nu_0 2\tau]}\} . \qquad (5.1.27)$$

For partially polarized light one has $0 < |\gamma(2\tau)| < 1$, if $|\gamma(2\tau)| = 1$ the light is coherent, and if $|\gamma(2\tau)| = 0$ the light is incoherent. For coherent light the output intensity becomes

$$I_{coh} = \frac{1}{4} Re^2\{m_a(\nu_0) e^{i[\phi_r(\nu_0)/2 - 2\pi\nu_0\tau]}\} + \frac{1}{4} Im^2\{m_b(\nu_0) e^{i\phi_r(\nu_0)/2}\} , \qquad (5.1.28)$$

which is identical to Eq. (5.1.13). As already explained in Section 5.1.1 the optical path difference ΔnL depends strongly on the environmental conditions. This is of course also true for the time delay difference τ. As a consequence, the first term of the right hand side in Eq. (5.1.28) fluctuates, resulting in a random drift at the detection, which affects the measured Faraday phase. It is therefore obvious that the detection with coherent light is of no practical use. For incoherent light, i.e. $\gamma(2\tau)| = 0$, the output intensity becomes

$$I_{incoh} = \frac{1}{8}|m_a(\nu_0)|^2 + \frac{1}{4} Im^2\{m_b(\nu_0)e^{i\phi_r(\nu_0)/2}\} . \qquad (5.1.29)$$

The term depending on the time delay difference τ has disappeared, thus no random drift occurs in this case. From the above considerations it follows that the reflection interferometer is of practical use only with incoherent light.

5.2. Detected intensity for different fiber configurations

It is assumed in this section that the only non-ideal optical element is the fiber coil. The theory developed in Section 5.1 is applied to different cases of fiber configurations. The first case treated is the ideal fiber coil. Then the twisted and spun (or helical) fiber configuration will be investigated and compared with the ideal fiber coil.

5.2.1. Ideal fiber coil

The forward and backward Jones matrices of the ideal coil undergoing the Faraday effect are given in Section 2.3.2. The matrices for the ideal quarterwave oriented at 45° with respect to the x axis are defined in Section (4.1.1). It follows then, using Eq. (5.1.7), that the Jones matrix **m** is given by

$$\mathbf{m} = \begin{pmatrix} m_a & -m_b^* \\ m_b & m_a^* \end{pmatrix} = \begin{pmatrix} 0 & i2e^{-i\varphi_F} \\ ie^{i2\varphi_F} & 0 \end{pmatrix} . \qquad (5.2.1)$$

Thus one has

$$m_a = 0 \quad \text{and} \quad m_b = ie^{i2\varphi_F} . \qquad (5.2.2)$$

It is clear that for the ideal case, i.e. all the optical elements are ideal, the matrix element m_a vanishes. Since the effects of the coherence are proportional to $|m_a(\nu_0)|^2$, this means that for the ideal case the coherence has no influence on the detected intensity. Using Eq. (5.1.27) for the detected intensity and the results above for the matrix elements, this yields

$$I = \frac{1}{4} Im^2\{ie^{i2\varphi_F}e^{i\phi_r(\nu_0)/2}\} = \frac{1}{8}\{1 + \cos[4\varphi_F + \phi_r(\nu_0)]\} . \qquad (5.2.3)$$

The Faraday phase φ_F is generally much smaller than 1, therefore the maximum sensitivity is obtained for $\phi_r(\nu_0) = -\pi/2$, which is the quadrature condition. In this case the detected intensity becomes

$$I = \frac{1}{8}[1 + \sin(4\varphi_F)] . \qquad (5.2.4)$$

For small values of the Faraday effect, i.e. $4\varphi_F \leq 0.1$ rad, one gets

$$I = \frac{1}{8} + \frac{1}{2}\varphi_F \,. \tag{5.2.5}$$

For ac detection of a small Faraday effect the detected signal is proportional to the Faraday phase.

5.2.2. Twisted and spun fiber

Proceeding in the same way as for the ideal coil, but using now the Jones matrices for the twist and spun fibers given in Sections 2.3.3 and 2.3.4, the matrix elements of m are

$$m_a = -2\frac{\eta\xi}{\gamma\gamma'}\sin(\gamma d)\sin(\gamma' d) + i\frac{\eta}{\gamma'}\sin(\gamma' d)\cos(\gamma d) + i\frac{\eta}{\gamma}\sin(\gamma d)\cos(\gamma' d) \tag{5.2.6}$$

and

$$m_b = -\frac{VH_z+\xi}{\gamma}\sin(\gamma d)\cos(\gamma' d) - \frac{VH_z-\xi}{\gamma'}\sin(\gamma' d)\cos(\gamma d)$$
$$- i\frac{(VH_z)^2-\xi^2+\eta^2}{\gamma\gamma'}\sin(\gamma d)\sin(\gamma' d) + i\cos(\gamma d)\cos(\gamma' d)\,, \tag{5.2.7}$$

where $\xi = \delta$ for twisted fibers and $\xi = -\alpha$ for spun or helical fibers. The exact solution for the detected intensity can be obtained introducing m_a and m_b, given by Eqs. (5.2.6) and (5.2.7), into Eq. (5.1.27). In order to get a better feeling for the behavior, it is worth-while to look at approximations for m_a and m_b. If $\xi >> \eta$ one has $(VH_z \pm \xi)/\gamma \approx 1$, $((VH_z)^2-\xi^2+\eta^2)/\gamma\gamma' \approx 1$, $\eta\xi/\gamma\gamma' \approx \eta/\gamma \approx \eta/\gamma \approx \eta/\xi$ and $\gamma \approx \gamma' \approx \xi$. This yields

$$m_a \approx i2\frac{\eta}{\xi}\sin(\gamma d)e^{i\gamma d} \quad \text{and} \quad m_b \approx ie^{i2\varphi_F}. \tag{5.2.8}$$

Only the approximate solutions will be investigated in the following. Introducing the expressions of Eq. (5.2.8) into Eq. (5.1.27) and assuming that the quadrature condition is satisfied, i.e. $\phi_r(\nu_0) = -\pi/2$, one gets

$$I \approx \frac{1}{8}[1 + \sin(4\varphi_F)] + \frac{1}{2}\left(\frac{\eta}{\xi}\right)^2\sin^2(\gamma d)$$
$$+ |\gamma(2\tau)|\frac{1}{2}\left(\frac{\eta}{\xi}\right)^2\sin^2(\gamma d)\cos(2\gamma d - 2\pi\nu_0 2\tau)\,. \tag{5.2.9}$$

The first term of the right hand side of Eq. (5.2.9) corresponds to the ideal case treated in Section 5.2.1. The second and the third terms result from the non-ideal fiber coil, however the third one disappears when incoherent light is used. Here again for $\varphi_F \leq 0.1$ the detected signal is essentially proportional to the Faraday phase φ_F. As a numerical example, the coil used in Section 4.7, which has a diameter of 345 mm and is formed of 20 turns twisted fiber with a

diameter of 80 μm, has a ratio of $\eta/\xi \approx 0.006$ at $\lambda = 780$ nm. Thus the maximum value $(\eta/\xi)^2$ of the second term is approximately 3.6×10^{-5}.

5.2.3. Effects of non-ideal quarterwave loop

Effects of quarterwave loop with a retardation R different from 90°, but with the correct orientation of the birefringence axes, will be analyzed. The forward and backward Jones matrices of the non-ideal quarterwave loop are

$$\vec{\mathbf{q}} = \begin{pmatrix} \cos(R/2) & i\sin(R/2) \\ i\sin(R/2) & \cos(R/2) \end{pmatrix} \quad , \quad \overleftarrow{\mathbf{q}} = \begin{pmatrix} \cos(R/2) & -i\sin(R/2) \\ -i\sin(R/2) & \cos(R/2) \end{pmatrix}, \tag{5.2.10}$$

where

$$R = \pi/2 + \Delta R \, . \tag{5.2.11}$$

The matrix **m** is obtained using Eq. (5.1.7), this yields for the matrix elements

$$m_a = -\sin(\Delta R)\cos(2\varphi_F) \tag{5.2.12}$$

and

$$m_b = -\sin(2\varphi_F) + i\cos(\Delta R)\cos(2\varphi_F) \, . \tag{5.2.13}$$

The output intensity is obtained applying Eq. (5.1.27). One gets

$$I = \frac{1}{8}[1+\sin(4\varphi_F)] - \frac{1}{4}\sin^2(\Delta R/2)\sin(4\varphi_F) + \frac{1}{8}|\gamma(2\tau)|\sin^2(\Delta R)\cos^2(2\varphi_F)\sin(2\pi\nu_0 2\tau) \, . \tag{5.2.14}$$

The first term of the right hand side of Eq. (5.2.14) corresponds to the ideal case treated in Section 5.2.1, the second and the third terms result from the non-ideal quarterwave loop, however the third one depends on the degree of coherence and fluctuates due to the random variations of the time delay difference τ. For small Faraday phase, i.e. $\varphi_F \leq 0.1$, the detected signal reduces to

$$I \approx \frac{1}{8}[1 + (1 - \Delta R^2/2)4\varphi_F] + \frac{1}{8}|\gamma(2\tau)|\Delta R^2\sin(2\pi\nu_0 2\tau) \, . \tag{5.2.15}$$

Assuming incoherent light, i.e. $|\gamma(2\tau)| = 0$, the detected intensity is proportional to the Faraday phase. The relative error of the slope $(dI/d\varphi_F)$, with respect to the ideal case ($\Delta R = 0$), is then

$$\varepsilon = -\Delta R^2/2 \, . \tag{5.2.16}$$

For $\Delta R = 1°$as an example one gets $|\varepsilon| = 0.3$ ‰.

5.2.4. Effects of non-ideal alignment of the quarterwave loop

In this section the quarterwave loop is assumed to be ideal, i.e. its linear retardation is 90°. Let $\Delta\theta$ be the misalignment error of the loop birefringence axes. The forward and backward Jones matrices of the quarterwave loop oriented at 45° with respect to the x reference axis are then

$$\vec{q} = \frac{1}{\sqrt{2}}\begin{pmatrix} 1-i\sin(2\Delta\theta) & i\cos(2\Delta\theta) \\ i\cos(2\Delta\theta) & 1+i\sin(2\Delta\theta) \end{pmatrix} \quad , \quad \overleftarrow{q} = \frac{1}{\sqrt{2}}\begin{pmatrix} 1-i\sin(2\Delta\theta) & -i\cos(2\Delta\theta) \\ -i\cos(2\Delta\theta) & 1+i\sin(2\Delta\theta) \end{pmatrix}. \quad (5.2.17)$$

The matrix **m** is obtained using Eq. (5.1.7), this yields for the matrix elements

$$m_a = -i\sin(2\Delta\theta)\cos(2\varphi_F) \quad (5.2.18)$$

and

$$m_b = -\sin(2\varphi_F) + i\cos(2\Delta\theta)\cos(2\varphi_F)\,. \quad (5.2.19)$$

The output intensity is obtained applying Eq. (5.1.27). One gets

$$I = \frac{1}{8}[1+\sin(4\varphi_F)] - \frac{1}{4}\sin^2(\Delta\theta)\sin(4\varphi_F)$$
$$-\frac{1}{8}|\gamma(2\tau)|\sin^2(2\Delta\theta)\cos^2(2\varphi_F)\sin(2\pi\nu_0 2\tau)\,. \quad (5.2.20)$$

The first term of the right hand side of Eq. (5.2.20) corresponds to the ideal case treated in Section 5.2.1, the second and the third terms result from the misalignment of the loop birefringence axes, however the third one depends on the degree of coherence and fluctuates due to the random variations of the time delay difference τ. For small Faraday phase, i.e. $\varphi_F \leq 0.1$, the detected signal reduces to

$$I \approx \frac{1}{8}[1 + (1-2\Delta\theta^2)4\varphi_F] + \frac{1}{2}|\gamma(2\tau)|\Delta\theta^2\sin(2\pi\nu_0 2\tau)\,. \quad (5.2.21)$$

Assuming incoherent light, i.e. $|\gamma(2\tau)| = 0$, the detected intensity is proportional to the Faraday phase. The relative error of the slope ($dI/d\varphi_F$), with respect to the ideal case ($\Delta\theta = 0$), is then

$$\varepsilon = -2\Delta\theta^2\,. \quad (5.2.22)$$

For $\Delta\theta = 1° \approx 0.0175$ rad as an example one gets $|\varepsilon| \approx 0.61$ ‰.

5.3. *The reflection interferometer with non-reciprocal internal phase modulation*

The principles of this set-up are given in Section 3.2.2 and its optical scheme is shown in Fig. 3.7. Figure 5.2 shows the corresponding bloc-diagram.

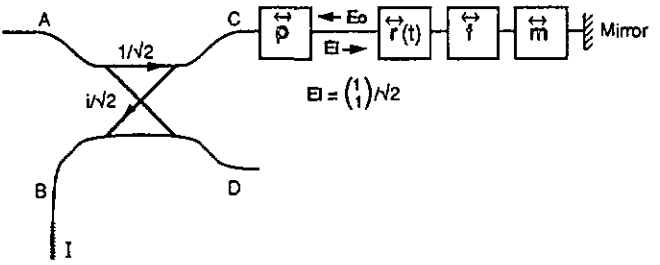

Figure 5.2 *Bloc-diagram representation of the reflection interferometer using internal non-reciprocal phase modulation* $\overleftrightarrow{r}(t)$.

The conventions adopted for the reference frame and the polarization basis are the same as in Section 5.1, this means that the Jones matrices $\overleftrightarrow{f}$ and $\overleftrightarrow{m}$ are unchanged. The linear polarizer is now inside the interferometer and has the same orientation as in Section 5.1, therefore $\overleftrightarrow{p} = p$ is unchanged too. The linear retardation $\overleftrightarrow{r}(t)$ is now also inside the interferometer and varies periodically with time at the frequency $\omega_m/2\pi$. As shown in Fig. 5.2, the input Jones vector E_i is the same as in Section 5.1, however it is now located after the polarizer inside the interferometer. The output Jones vector E_o is located before the polarizer in backward propagation. The polarization properties of the coupler have no influence on the detected signal any more.

Using the above definitions and remembering that a second reflection matrix has to be introduced, one gets for the output Jones vector

$$E_o = s\ \overleftarrow{r}(t)\ \overleftarrow{f}\ \overleftarrow{m}\ s\ \overrightarrow{m}\ \overrightarrow{f}\ \overrightarrow{r}(t)\ E_i\ . \tag{5.3.1}$$

The backward and forward Jones matrices of the linear retardation are

$$\overrightarrow{r}(t) = \begin{pmatrix} e^{i\phi_r(t)/2} & 0 \\ 0 & e^{-i\phi_r(t)/2} \end{pmatrix} \quad \text{and} \quad \overleftarrow{r}(t) = \begin{pmatrix} e^{i\phi_r(t+T)/2} & 0 \\ 0 & e^{-i\phi_r(t+T)/2} \end{pmatrix}, \tag{5.3.2}$$

where T is the propagation time for a total round trip in the interferometer. If the linear retardation varies rapidly with respect to T, one has $\phi_r(t) \neq \phi_r(t+T)$, therefore $\overleftarrow{r}(t) \neq \overrightarrow{r}(t)^{\wedge}$. This means that the rapidly time varying linear retarder is a non-reciprocal device and can be considered as a non-reciprocal birefringent phase modulator. From Eq. (5.3.2) one can write

$$\overrightarrow{r}(t) = r(t) \quad \text{and} \quad \overleftarrow{r}(t) = r(t+T)\ . \tag{5.3.3}$$

Taking into account that s, f, r(t) and r(t+T) are diagonal and that $\overrightarrow{f} = \overleftarrow{f} = f$, Eq. (5.3.1) simplifies to

$$E_o = r(t+T)\ f\ m\ f\ r(t)\ E_i\ , \tag{5.3.4}$$

where $\mathbf{m}$ is defined in Section 5.1. Using the explicit expressions for the above matrices and Eq. (5.1.1) for $\mathbf{E_i}$ the output Jones vector is found to be

$$\mathbf{E_o} = \frac{1}{\sqrt{2}} \begin{pmatrix} m_a e^{i(k\Delta nL+\bar{\phi}(t))} - m_b^* e^{-i\Delta\phi(t)/2} \\ m_a^* e^{-i(k\Delta nL+\bar{\phi}(t))} + m_b e^{i\Delta\phi(t)/2} \end{pmatrix}, \tag{5.3.5}$$

where

$$\bar{\phi}(t) = \frac{\phi_r(t+T) + \phi_r(t)}{2} \quad \text{and} \quad \Delta\phi(t) = \phi_r(t+T) - \phi_r(t) . \tag{5.3.6}$$

This result is very similar to the one obtained in Section 5.1.1 for $\mathbf{E_o}$, the only difference appears in the phase terms, that is $\bar{\phi}(t)$ and $\Delta\phi(t)$. It is therefore not necessary to apply again the procedure used in Section 5.1.2 to get the output intensity with coherence source effects. Equation (5.1.27) can be used after introduction of the relevant modifications for the phase ϕ. Assuming that the integration time is shorter than the period $2\pi/\omega_m$ of the phase modulation, i.e. $< \cos(\omega_m t) > = \cos(\omega_m t)$, and taking into account that the output intensity is half the intensity emerging from the polarizer, this yields

$$I(t) = \frac{1}{4}|m_a(\nu_0)|^2 + \frac{1}{2} Im^2\{m_b(\nu_0)e^{i\Delta\phi(t)/2}\}$$
$$+ \frac{1}{4}|\gamma(2\tau)| Re\{m_a^2(\nu_0)e^{i[2\bar{\phi}(t)-2\pi\nu_0 2\tau]}\} . \tag{5.3.7}$$

In Section 5.1 $\mathbf{E_i}$ was located before the coupler (side A), whereas now it is located after the coupler (side C), this introduces a difference of a factor two between Eqs. (5.1.27) and (5.3.7). If incoherent light is used, i.e. $|\gamma(2\tau)| = 0$, one gets

$$I(t) = \frac{1}{4}|m_a(\nu_0)|^2 + \frac{1}{2} Im^2\{m_b(\nu_0)e^{i\Delta\phi(t)/2}\} . \tag{5.3.8}$$

In the following, only the case of incoherent light will be treated, because coherent light is not useful for practical applications.

5.3.1. Detected intensity for different fiber configurations

Ideal fiber coil

From Section 5.2.1 one has $m_a = 0$ and $m_b = ie^{i2\varphi_F}$. Introducing into (5.3.8) one obtains

$$I(t) = \frac{1}{4} + \frac{1}{4}\cos[4\varphi_F + \Delta\phi(t)] . \tag{5.3.9}$$

This result is similar to the one obtained for the Sagnac interferometer (see Eq. (4.1.27)) but now the Faraday phase φ_F is multiplied by a factor four instead of two, therefore the sensitivity to the Faraday effect is doubled compared with the Sagnac interferometer.

Twisted and spun fiber

The matrix elements are given by Eqs. (5.2.6) and (5.2.7). As shown in Eq. (5.3.8) only m_b combines with the phase modulation $\Delta\phi(t)$. In order to get a better readable expression for I(t) it is worthwhile to rewrite m_b in a more condensed form, namely

$$m_b = Re\{m_b\} + iIm\{m_b\} = A + iB\,. \tag{5.3.10}$$

Introducing into Eq. (5.3.8), the output intensity becomes

$$I(t) = \frac{1}{4}|m_a(v_0)|^2 + \frac{A^2+B^2}{4} + \frac{A^2-B^2}{4}\cos\Delta\phi(t) + \frac{AB}{2}\sin\Delta\phi(t)\,. \tag{5.3.11}$$

This result is general and can be use with any Jones matrix m.

5.3.2. Faraday phase recovery

Like for the Sagnac interferometer the Faraday phase shift $4\varphi_F$ is obtained from the detected intensity I(t) thanks to the non-reciprocal phase modulation $\phi_r(t)$, which is of the form

$$\phi_r(t) = \phi_0\sin(\omega_m t)\,, \tag{5.3.12}$$

using Eq. (5.3.6) this yields

$$\Delta\phi(t) = 2\phi_0\sin(\omega_m T/2)\cos[\omega_m(t+T/2)] = \Delta\phi_0\cos[\omega_m(t+T/2)]\,. \tag{5.3.13}$$

In the next chapter, the Sagnac and the reflection interferometers will be compared. The latter having a sensitivity two times larger than the former. It is therefore necessary, in order to get a realistic comparison, that the coil of the reflection interferometer has half the number of turns compared to the one of the Sagnac interferometer. Thus, in the following numerical simulations a coil with 10 turns will be used.

Ideal fiber coil

Replacing Eq. (5.3.13) into Eq. (5.3.9) one gets for the detected intensity

$$\begin{aligned} I(t) = \frac{1}{4}[1 + J_0(\Delta\phi_0)\cos(4\varphi_F)] \\ - \frac{1}{2}\sin(4\varphi_F)\sum_{\mu\text{odd}}^{\infty}(-1)^{(\mu+1)/2}J_\mu(\Delta\phi_0)\cos[\mu\omega_m(t+T/2)] \\ + \frac{1}{2}\cos(4\varphi_F)\sum_{\mu\text{even}}^{\infty}(-1)^{\mu/2}J_\mu(\Delta\phi_0)\cos[\mu\omega_m(t+T/2)]\,, \end{aligned} \tag{5.3.14}$$

where $J_\mu(\Delta\phi_0)$ denotes the μth-order Bessel function. To recover the Faraday phase shift, the same signal processing principle as for the Sagnac interferometer is applied, namely

$$\varphi_d = \tan^{-1}\left(\frac{J_2(\Delta\phi_0)}{J_1(\Delta\phi_0)}\,\frac{I(\omega_m)}{I(2\omega_m)}\right), \tag{5.3.15}$$

where φ_d is the detected phase, and $I_R(\omega_m)$ and $I_R(2\omega_m)$ are the amplitudes of the components of I(t) at ω_m and $2\omega_m$, respectively. For the ideal fiber coil this yields, using (5.3.14),

$$\varphi_d = 4\varphi_F = 4VNI\,, \tag{5.3.16}$$

which corresponds to an ideal detection of the Faraday effect.

Twisted and spun fiber

The output intensity for mechanically twisted fiber and for spun or helical fiber is given in Section 5.3.1. Using Eq. (5.3.13) for $\Delta\phi(t)$ and the definition given above for the detected phase, one gets

$$\varphi_d = \tan^{-1}\left(\frac{2AB}{A^2-B^2}\right). \tag{5.3.17}$$

For sufficiently large twist or spin rates, i.e. $\delta >> \eta$ or $\alpha >> \eta$, the detection is nearly ideal, namely $\varphi_d \approx 4\varphi_F$. The relative error due to non-ideal fiber coil is defined as

$$\varepsilon_\varphi = \frac{\varphi_d - 4\varphi_F}{4\varphi_F}\,, \tag{5.3.18}$$

where $\varphi_F = VNI$. Figure 5.3 shows the relative detected phase error ε_φ versus the Faraday phase φ_F, calculated from Eq. (5.3.17) for a 10 turns twisted fiber coil with a diameter of 2R = 345 mm, a fiber diameter of 2r = 80 μm, a twist rate of $T = 10\times 2\pi$ rad/m and a Verdet constant of V = 2.6 μrad/A at λ = 820 nm.

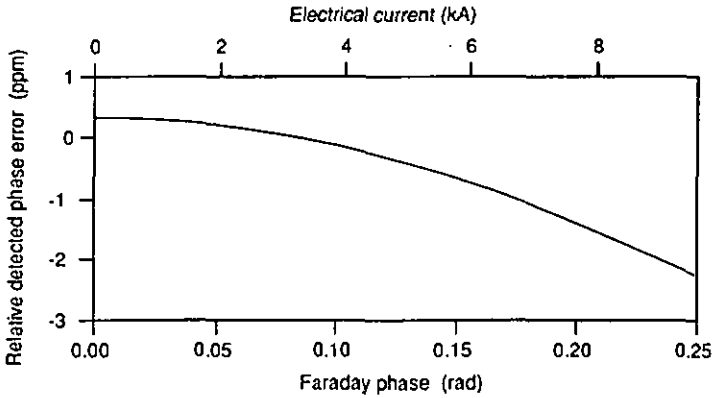

Figure 5.3 Calculated relative phase error versus Faraday effect for the twisted fiber coil.

For this example, the relative detected phase error is smaller than 3 ppm for currents from 0 A to approximately 10 kA.

In conclusion, the reflection configuration used with a twisted fiber coil, or with a spun or helical fiber coil, permits to measure the Faraday phase shift with negligible error, at least for most practical current ranges.

5.4. Temperature effects due to the sensing coil

Like for the Sagnac interferometer, the Verdet constant is assumed to be temperature independent. Thus only the temperature effects of the bending, stress (hi-bi spun fibers) and twist induced birefringences are taken into account in the following. The case of the twisted fiber is treated here, this means that the fiber undergoes mechanical twist end bending. The temperature coefficient α_η and α_δ of the bend and the twist induced birefringences, respectively, are in given in Section 4.4.

For twisted fibers ($\xi = \delta$) the detected phase defined by Eq. (5.3.17) takes the form

$$\varphi_d(T) = \varphi_d[\eta(T),\delta(T)] , \tag{5.4.1}$$

where $\eta(T)$ and $\delta(T)$ are defined in Section 4.4. For spun or helical fibers ($\xi = \alpha$) rotational effects are of geometrical type and therefore not temperature dependent, this yields

$$\varphi_d(T) = \varphi_d[\eta(T)] . \tag{5.4.2}$$

The relative detected phase error versus temperature is defined as

$$\varepsilon_\varphi(T) = \frac{\varphi_d(T) - 4\varphi_F}{4\varphi_F} , \tag{5.4.3}$$

where $\varphi_F = 4VNI$. Figure 5.4 shows the relative error $\varepsilon_\varphi(T)$ computed for the same twisted fiber coil given in Section 5.3.2. One sees that $\varepsilon_\varphi(T)$ is approximately independent of the Faraday phase shift and is, for this practical example, smaller than 35 ppm. The periodic behavior, like for the Sagnac interferometer, is due to the terms γd and $\gamma' d$ in Eq. (5.3.17), these terms are approximately equal to $17 \times 2\pi$ and vary by an amount of about 2π between -40 C° and 80 °C. Because γd and $\gamma' d$ are arguments of sine and cosine functions in Eq. (5.3.17), this results in a periodic behavior of $\varepsilon_\varphi(T)$.

It appears from this example that the reflection configuration using a twisted fiber coil, exhibits temperature variations which are negligible for practical current sensing applications (required minimal error ≥ 0.1 %). This is obviously also true for spun or helical fiber coils.

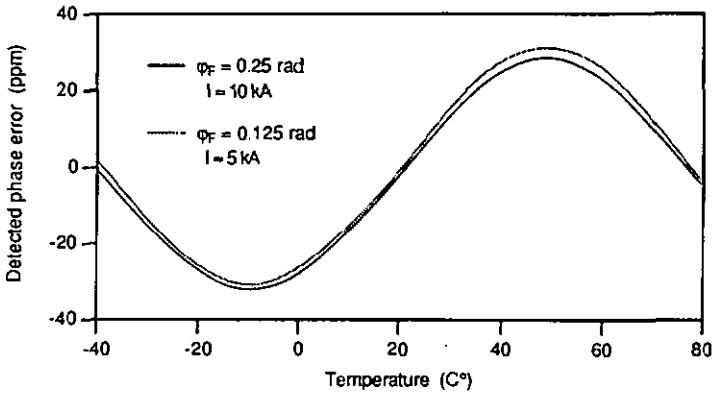

Figure 5.4 Calculated temperature dependance of the relative phase error due to the fiber coil. Fiber diameter $2r$ = 80 μm, coil diameter $2R$ = 345 mm, twist rate $T = 10 \times 2\pi$ rad/m, number of turns N = 10, Verdet constant = 2.6 μrad/A at λ = 820 nm.

5.5. Effects of non-ideal quarterwave loop

The quarterwave loop has to transform the orthogonal linear polarizations, coming from each birefringence axis of the hi-bi fibers, into circular orthogonal polarizations. Moreover, after having undergone the Faraday effect, the circular polarizations are again transformed in linear polarizations thanks to the quarterwave loop. These transformations of polarizations will be correctly performed only if the retardation of the loop is 90° and if the orientation of its birefringence axes is at 45° with respect to those of the hi-bi fibers. In this section, influences of errors affecting the retardation and the orientation of the quarterwave loop will be theoretically investigated. In the following it is supposed that the only non-ideal element in the reflection interferometer is the quarterwave loop.

5.5.1. Retardation error effects

In this section, effects of quarterwave loop with a retardation R different from 90°, but with correct orientation of birefringence axes, will be studied.

The matrix elements m_a and m_b for a quarterwave loop with a retardation error ΔR are given in Section 5.2.3, that is

$$m_a = -\sin(\Delta R)\cos(2\varphi_F) \quad \text{and} \quad m_b = -\sin(2\varphi_F) + i\cos(\Delta R)\cos(2\varphi_F) = A + iB\,. \qquad (5.4.4)$$

Introducing m_a, A and B into Eq. (5.3.11) one gets for the detected intensity

$$I(t) = \frac{1}{4} - \frac{1}{4}(\sin^2 2\varphi_F - \cos^2\Delta R\cos^2 2\varphi_F)\cos\Delta\phi(t) - \frac{1}{4}\sin 4\varphi_F\cos\Delta R\sin\Delta\phi(t)\,. \qquad (5.4.5)$$

The detected phase is obtained introducing A and B into Eq. (5.3.17). This yields

$$\varphi_d = \tan^{-1}\left(\frac{\sin 4\varphi_F \cos\Delta R}{\cos^2 2\varphi_F \cos^2\Delta R - \sin^2 2\varphi_F}\right) . \tag{5.4.6}$$

This results are very similar to the ones obtained for the Sagnac interferometer. The relative detected phase error is defined as

$$\varepsilon_\varphi = \frac{\varphi_d - 4\varphi_F}{4\varphi_F} . \tag{5.4.7}$$

Assuming $\Delta R << 1$ the relative phase error approximates to

$$\varepsilon_\varphi \approx \frac{\Delta R^2}{2} . \tag{5.4.8}$$

For $R = 88°$ or $R = 92°$ this gives $\Delta R = \pm 2° \approx \pm 0.035$ rad and thus $\varepsilon_\varphi \approx 6.1 \times 10^{-4}$ or 0.61 ‰, which is the same result as for the Sagnac interferometer. This example shows that a retardation error of 2° results in a relative detected phase error smaller than 1 ‰. This is acceptable for current sensor applications.

5.5.2. Temperature effects

The quarterwave loop is made of the same ultra-low birefringence fiber type as the fiber sensing coil. At a wavelength of $\lambda = 820$ nm, the linear retardation of $R = 90°$ is obtained with a fiber loop diameter of 10 mm for a fiber of diameter $2r = 80$ µm. The temperature dependance of the retardation is only due to the bend induced linear birefringence, because, like for the fiber sensing coil, the coating effects are negligible.

The detected phase versus temperature is given by

$$\varphi_d(T) = \varphi_d[\Delta R(T)] , \tag{5.4.9}$$

where $\varphi_d(\Delta R)$ is given by Eqs. (5.4.6). $\Delta R(T)$ is obtained from the definitions of ΔR and taking into account that the loop retardation is due to the bend induced linear birefringence $\eta(T)$. Thus

$$\Delta R(T) = \Delta R_0 + R\alpha_\eta(T - T_0) , \tag{5.4.10}$$

where ΔR_0 is the value of $\Delta R(T)$ at room temperature T_0 and is defined in Section 5.2.3, whereas R is the loop retardation at the room temperature, i.e. $R = \pi/2 + \Delta R_0$. The relative detected phase error $\varepsilon_\varphi(T)$ is obtained from Eq. (5.4.9) using

$$\varepsilon_\varphi(T) = [\varphi_d(T) - 4\varphi_F]/4\varphi_F. \tag{5.4.11}$$

Figure 5.5 shows the relative detected phase error versus temperature for a Faraday phase shift of $\varphi_F = 0.25$ rad corresponding to a current of about 10 kA for a 10 turns fiber coil and a Verdet constant of V = 2.6 µrad/A at λ = 820 nm. One sees that the best temperature behavior, i.e. the smaller relative phase error versus temperature, is obtained using a loop with a linear retardations of R = 90°. In this case the maximum error is smaller than 1.3 ‰ in the considered temperature range.

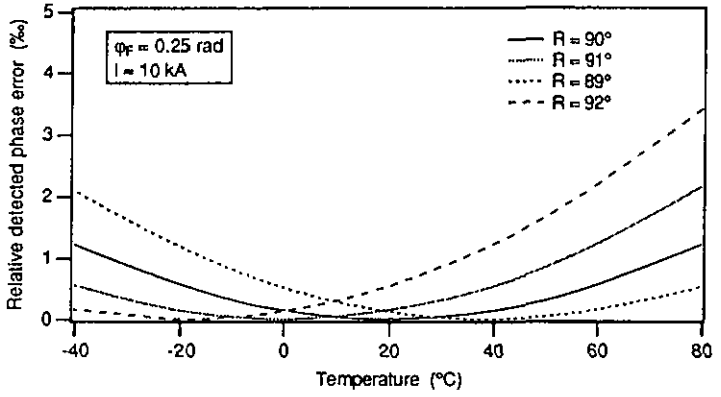

Figure 5.5 Calculated relative phase error ε_φ versus temperature, for different values of the loop retardation R (given at room temperature) and for a Faraday phase of $\varphi_F = 0.25$ rad corresponding to about 10 kA for a 10 turns fiber coil and a Verdet constant of V = 2.6 µrad/A at λ = 820 nm.

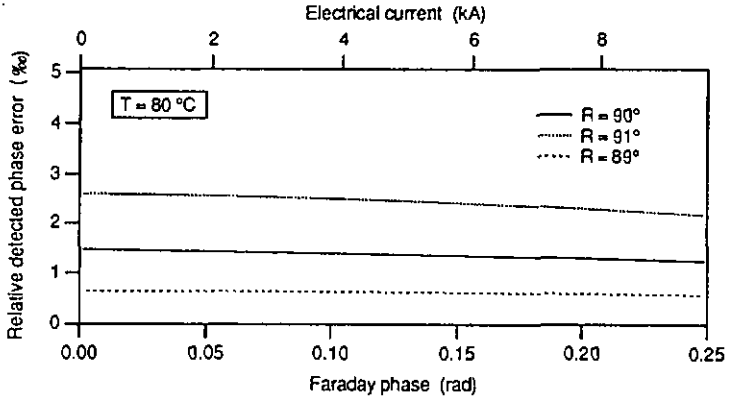

Figure 5.6 Calculated relative phase error ε_φ versus Faraday phase at the temperature T = 80 C° for different values of the loop retardation R (given at room temperature).

From Fig. 5.5 one sees also that a retardation error of ±1° at room temperature gives rise to a relative phase error larger than 2 ‰. Therefore in order to get a relative detected phase error smaller than 2 ‰, which is often required for current sensing applications, a retardation precision of ±0.5° is necessary for the quarterwave loop at the room temperature. The behavior of the relative detected phase error ε_φ versus the Faraday phase is given in Fig. 5.6 for a temperature of T = 80 °C. One sees that ε_φ is approximately independent of the Faraday phase and can be merely evaluated using Eq. (5.4.7).

In conclusion, using appropriate quarterwave fiber loops, relative detected phase errors smaller than 2 ‰ are obtained. This is acceptable for most current sensing applications.

5.5.3. Misalignment effects

The quarterwave loop is assumed to be ideal, i.e. its linear retardation is 90°.

The matrix elements m_a and m_b for a quarterwave loop with an alignment error $\Delta\theta$ are given in Section 5.2.4, that is

$$m_a = -i\sin(\Delta\theta)\cos(2\varphi_F) \quad \text{and} \quad m_b = -\sin(2\varphi_F) + i\cos(2\Delta\theta)\cos(2\varphi_F) = A + iB\,. \tag{5.4.12}$$

Introducing m_a, A and B into Eq. (5.3.11) one gets for the detected intensity

$$I(t) = \frac{1}{4} + \frac{1}{4}(\sin^2 2\varphi_F - \cos^2 2\Delta\theta\cos^2 2\varphi_F)\cos\Delta\phi(t) - \frac{1}{4}\sin 4\varphi_F\cos 2\Delta\theta\sin\Delta\phi(t)\,. \tag{5.4.13}$$

The detected phase is obtained introducing A and B into Eq. (5.3.17), this yields

$$\varphi_d = \tan^{-1}\left(\frac{\sin 4\varphi_F\cos 2\Delta\theta}{\cos^2 2\varphi_F\cos^2 2\Delta\theta - \sin^2 2\varphi_F}\right). \tag{5.4.14}$$

Again, this results are very similar to the ones obtained for the Sagnac interferometer. The relative error ε_φ is defined by Eq. (5.4.11). Assuming $\Delta\theta \ll 1$ one has

$$\varepsilon_\varphi \approx 2\Delta\theta^2\,. \tag{5.4.15}$$

For $\Delta\theta = 1° \approx 0.0175$ rad this gives $\varepsilon_\varphi \approx 6.1 \times 10^{-4}$ or 0.61 ‰. This example shows that an alignment error of 1° results in a relative detected phase error smaller than 1 ‰, which is acceptable for current sensing applications.

5.6. Experimental investigations of the unmodulated reflection interferometer

The purpose of this section is to demonstrate experimentally the principles of the reflexion interferometer developed in Sections 5.1 and 5.2. The basic optical arrangement of the reflection interferometer is in given in Fig. 3.6. In the following the fiber coupler was replaced

by a bulk beam splitter which do not perturb the polarization state. The reflection interferometer with internal non-reciprocal phase modulation will be investigated in Section 5.7.

5.6.1. High coherence source

In this experiment the degree of coherence $|\gamma(2\tau)|$ of the light source is nearly equal to one, this will permit to point out the perturbing effects of coherent cross-coupling arising in the interferometer.

Experimental set-up and signal processing

The experimental set-up and the signal processing are shown in Fig. 5.7.

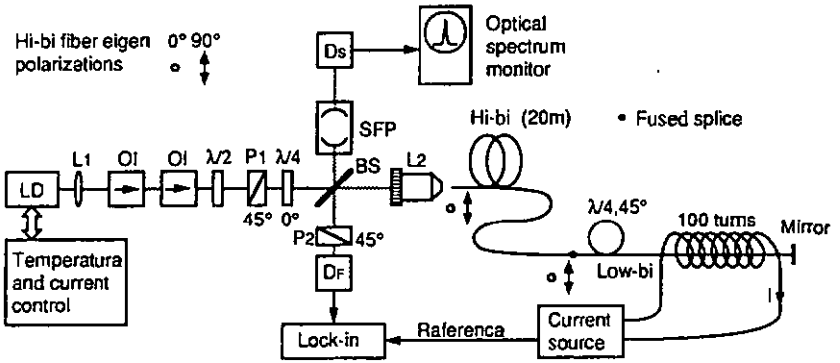

Figure 5.7 Experimental set-up. LD: single-mode laser-diode (λ = 780 nm), L_1: antireflection coated lens, OI: optical isolator, $P_{1,2}$: Glan Thomson polarizers, BS: beam splitter cube, SFP: scanned Fabry-Perot analyser, $D_{S,F}$: silicon photodiode detectors, L_2: low-bi microscope objective, I: electrical current.

A single mode laser-diode emitting at a wavelength of λ = 780 nm with an antireflection coated collimating lens (L_1) is used. The laser-diode is current and temperature stabilized. To ensure a pure single mode behavior two Faraday isolators are placed after the collimating lens. The spectrum of the laser source is monitored using a scanned Fabry-Perot analyser (SFP), this allows to get an optimal adjustment of the two isolators and to be sure that the source remains coherent during the measurements. The halfwave retardation plate serves to adjust the linear polarization at 45 ° respect to the birefringence axes of the hi-bi fiber. The Glan-Thomson polarizer (P_1) is necessary to guarantee a perfect linear polarization state. The quarterwave retardation plate permits to get the quadrature condition for optimum detection of the Faraday effect, as explained in Section 3.2.2. The bulk beam splitter (BS) is nearly polarization independent. The characteristics of the hi-bi polarization maintaining fiber (York HB 800, 125 µm) and of the adjustable quarterwave fiber loop (York LB 800, 125 µm) are given in Section 4.6.3. The sensing element is formed of a piece of straight fiber of ultra low birefringence type (York LB 800, 125 µm) which is end mirrored (glued 100 % reflecting dielectric mirror). The magnetic field is produced by a 100 turn solenoid. After the output Glan-Thomson polarizer (P_2), the interference signal is detected and analyzed using a lock-in amplifier. The current

source supplies an ac current at 75 Hz, a TTL output provides the reference signal for the lock-in amplifier.

Faraday effect measurement

The straight sensing fiber represents an ideal sensing coil without birefringence. Assuming that the orientation of the different polarizing elements are correct, it results that we are nearly in the ideal case described in Section 5.2.1. Thus the effects of the coherence of the source should be negligible. The maximum available electrical current is 40 A (rms). This results in a Faraday phase of $\varphi_F = 12$ mrad for a 100 turn current coil and for $V \approx 3$ µrad/A at $\lambda = 780$ nm. Therefore $\sin(4\varphi_F) \approx 4\varphi_F$ in the considered current range and Eq. (5.2.5) can be used. The detected voltage U(t) is proportional to the detected intensity. Using Eq. (5.2.5) one gets

$$U(t) = U_0[1 + 4\varphi_F(t)] = U_0[1 + 4VNI(t)], \tag{5.6.1}$$

where I(t) is the electrical current, N the number of turns of the current coil and U_0 is the dc component of the detected voltage. The ac component is then given by

$$U_{ac}(t) = 4U_0VNI(t), \tag{5.6.2}$$

which is proportional to the electrical current.

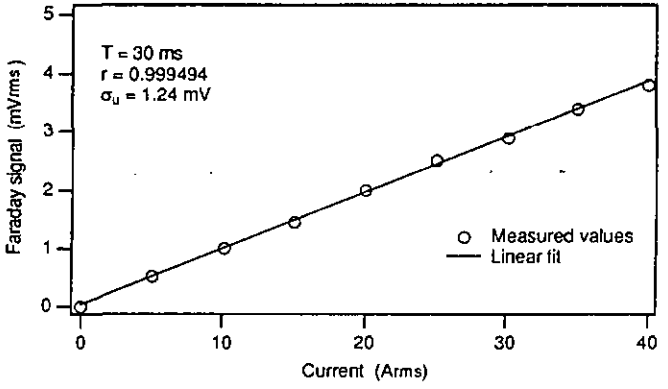

Figure 5.8 Measured output voltage versus electrical current.

The measured dc component was $U_0 \approx 100$ mV. From Eq. (5.6.2) this gives a slope, or sensitivity, of $S_I = 0.12$ mV/A for $V \approx 3$ µrad/A ($\lambda = 780$ nm) and N = 100. The measured ac output voltage (Faraday signal) versus the electrical current I is shown in Fig. 5.8. The integration time of the lock-in amplifier was T = 30 ms. The detected optical power is approximately 10 µW. The measured slope was $S_I = 0.096$ mV/A, this is in good agreement with the expected theoretical value of 0.12 mV/A, taking into account that the Verdet constant is not precisely known. The output noise voltage for the integration time of 30 ms was approximately 1 µV; this correspond to a current noise of 0.01 A. A linear fit to the measured values yields the standard deviation σ_u and the correlation coefficient r. The rms voltage error is

obtained using $\delta U = \sigma_u\sqrt{1-r^2}$. From the measured values one gets $\delta u \approx 0.04$ mV, which corresponds to a rms current error of $\delta I \approx 0.42$ A. The expected error due to the measured noise is 40 times smaller than the actual error of 0.42 A. This is mainly due to coherent polarization cross-coupling produced by the non-ideal elements constituting the interferometer, to fluctuations of the optical power, and to voltage and current reading errors.

In theory the dc component U_0 should be stable, however, neither the fiber elements (quarterwave loop, sensing fiber, bi-bi fiber, etc) nor their orientation with respect to each other (orientation of the birefringence axes) are perfect. Therefore, in practice the ideal case of the Section 5.2.1 is not perfectly achieved and the matrix element m_a (see Eq. (5.1.27) is not zero. This results in an additional term in the detected voltage which depends on the time delay difference τ of the hi-bi fiber. The fluctuations of the dc component U_0 have been measured to be about ± 10 % around a mean value of $U_0 \approx 100$ mV. The typical time constant of these fluctuations corresponds to a few seconds.

Effect of the polarization cross-coupling

To point out the effects of coherent polarization cross-coupling we modified in a well controlled way the retardation or the orientation of the birefringence axes of the quarterwave loop. This produces a large polarization cross-coupling, resulting in fluctuations of the detected signal due to the drift of the time delay difference τ of the hi-bi fiber. If the retardation of the loop is varied by ΔR, the resulting detected intensity is given by Eq. (5.2.14). The detected intensity I contains a term I_0 which is independent of τ and an other one ΔI which is proportional to $\sin(2\pi\nu_0 2\tau)$. For a coherent source, i.e. $|\gamma(T)| = 1$, ΔI varies between $\pm\Delta I_0 = \pm\sin^2(\Delta R)$. The relative fluctuations are found to be

$$\frac{\Delta I_0}{I_0} = \frac{\sin^2\Delta R}{1 - 2\sin^2\Delta R/2} \quad . \tag{5.6.3}$$

When the orientation of the birefringence axes of the loop is varied by $\Delta\theta$, the resulting detected intensity is given by Eq. (5.2.20). With the same assumptions as above and applying the same procedure one gets

$$\frac{\Delta I_0}{I_0} = \frac{\sin^2 2\Delta\theta}{1 - 2\sin^2\Delta\theta} \quad . \tag{5.6.4}$$

The quarterwave fiber element is formed by a loop which is compressed between two rigid plates [Fro88]. The retardation R can be varied by changing the compression force, which is adjustable with a screw acting on a spring. The alignment of the birefringence axes is given by the angular position of the loop plane, which can be varied between –45° up to 45°. Figure 5.9 shows the detected voltage U(t) for zero Faraday phase and for different values of the retardation error ΔR in the case of correct alignment ($\Delta\theta = 0°$). At the time t = 0 s the hi-bi fiber was heated over a length of about 1 cm until the temperature had increased by about 15 °C. This produces a variation of the time delay difference τ. After about 25 s the heating is removed and the fiber temperature decreases down to the room temperature producing again a variation of τ, but with the opposite sign. These variations of τ results in fluctuations ΔU of the the detected voltage around a mean value U_0 as explained above, ΔU and U are proportional to ΔI and I_0, respectively.

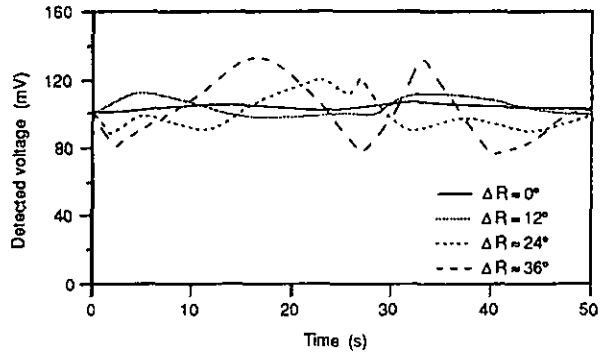

Figure 5.9 Detected voltage versus time for zero Faraday effect and for different values of the quarterwave loop retardation error ΔR.

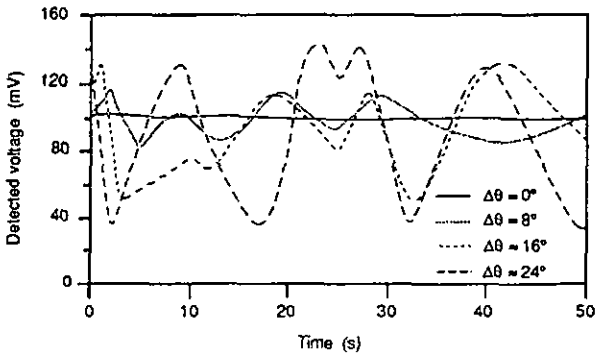

Figure 5.10 Detected voltage versus time for zero Faraday effect and for different values of the quarterwave loop misalignement $\Delta\theta$.

The same measurements have been performed for different values of the misalignment $\Delta\theta$ in the case of correct loop retardation ($\Delta R = 0°$). The results are shown in Fig. 5.10.

Measurements of $\Delta I_0/I_0 = \Delta U_0/U_0$ versus the retardation and alignment errors ΔR and $\Delta\theta$, respectively, have been performed with the set-up of Fig. 5.7. These results are reported in Figs. 5.11 and 5.12 together the theoretical predictions given by Eqs. (5.6.3) and (5.6.4). The values of ΔU_0 and U_0 are obtained from Figs. 5.9 and 5.10 with a precision of about 20%. In practice it is difficult to know the exact values of ΔR, because the mechanical device producing the variation of the loop retardation is not calibrated and is not always the same for the same screw position. The error affecting the evaluated value of ΔR was estimated at about $\pm 5°$, whereas the error of the alignment of the loop birefringence axes was estimated at about $\pm 2°$.

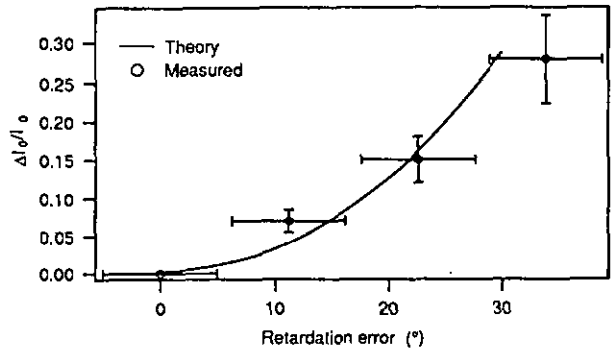

Figure 5.11 Relative fluctuation of the detected voltage versus the loop retardation error ΔR.

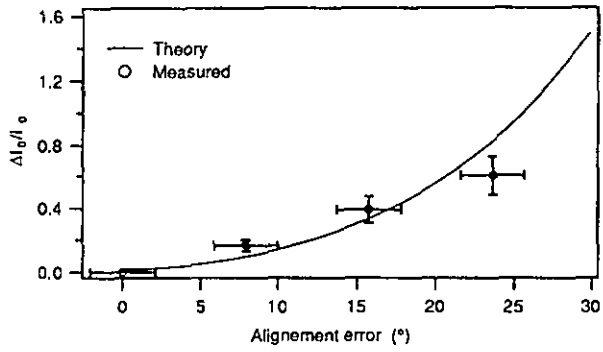

Figure 5.12 Relative fluctuation of the detected voltage versus the loop misalignment error $\Delta\theta$.

These results show good agreement between the theoretical model and the measurements. This confirms that the reflection interferometer with a coherent source suffers from severe fluctuations. Even if the loop retardation is close to 90° and its orientation is correct, coherent polarization cross-coupling arises in the hi-bi fiber and in the other non-ideal elements, which results in fluctuations of the detected signal and perturbs the Faraday phase measurement.

5.6.2. Low coherence source

In this experiment the degree of coherence $|\gamma(2\tau)|$ of the source was nearly equal to zero. This means that there should be no coherent polarization cross-coupling affecting the detected signal.

Experimental set-up and signal processing

The experimental set-up and the signal processing is shown in Fig. 5.13.

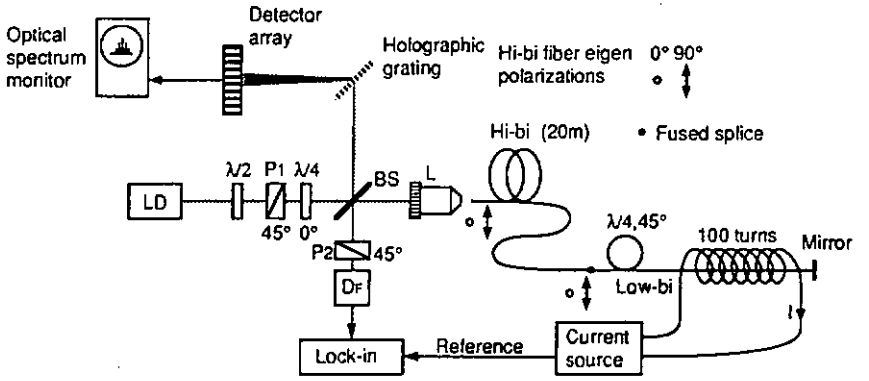

Figure 5.13 Experimental set-up. LD: multimode laser-diode (λ = 780 nm, $\Delta\lambda \approx$ 3 nm), $P_{1,2}$: Glan-Thomson polarizers, BS: beam splitter cube, D_F: silicon photodiode detector, L: low-bi microscope objective, I: electrical current.

The multimode laser-diode emits at a wavelength of λ = 780 nm with a spectral bandwidth of $\Delta\lambda \approx$ 3 nm, corresponding to a coherence length of $L_c \approx \lambda^2/\Delta\lambda \approx$ 200 μm. The spectrum of the source is monitored during the measurements, using a spectrometer which consist of a holographic grating and a detector array. This control is necessary to make sure that the source remains multimode in spite of the light reflected back from the interferometer. The beat length L_b of the hi-bi fiber is approximately 2 mm. One beat length corresponds to an optical path unbalance of λ = 780 nm. The length of the hi-bi fiber is L ≈ 20 m, which is equivalent to 10^4 beat lengths. Therefore, after a total round trip in the hi-bi fiber the resulting optical path unbalance is $2\Delta L = 2 \times 10^4 \times 780$ nm = 15.6 mm, and thus $2\Delta L \approx 80 L_c$, which means that $|\gamma(2\tau)| \approx 0$. The interferometer itself and the signal processing are the same as for the high coherence source.

Faraday effect measurement

The measured ac output voltage (Faraday signal) versus the electrical current I is shown in Fig. 5.14. The experimental conditions are the same as in Section 5.6.1 and therefore the ac component of the detected voltage is also given by Eq. (5.6.2). The measured dc component was $U_0 \approx$ 33 mV. From Eq. (5.6.2) this gives a slope, or sensitivity, of $S_I \approx$ 0.04 mV/A for V ≈ 3 μrad/A (λ= 780 nm) and N = 100. The integration time of the lock-in amplifier was T = 30 ms. The detected optical power was approximately 3.3 μW. The measured slope was $S_I \approx$ 0.034 mV/A, this is in good agreement with the expected theoretical value of 0.04 mV/A, taking into account that the Verdet constant is not precisely known. The output noise voltage, for the integration time of 30 ms, was approximately 1 μV. This corresponds to a current noise of 0.019 A. A linear fit to the measured values yields the standard deviation σ_u and the correlation coefficient r. The rms voltage error is obtained using $\delta U = \sigma_u\sqrt{1-r^2}$. From the measured values one gets $\delta U \approx$ 0.011 mV, which corresponds to a rms current error of $\delta I \approx$ 0.32 A. The expected error due to the measured noise is 17 times smaller than the actual

error of 0.32 A. This is mainly due to fluctuations of the optical power, and to voltage and current the reading errors.

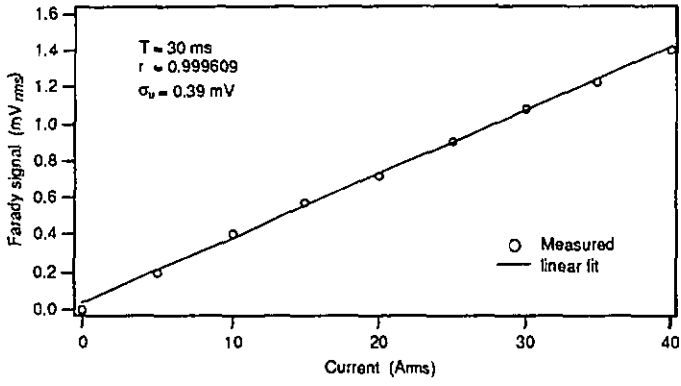

Figure 4.14 Measured output voltage versus electrical current.

In contrast to the case whith the coherent source, the dc component U_0 did not fluctuate with time, which confirms that the cross-coupled polarizations do not interfere any more.

Effects of quarterwave loop retardation error

Assuming correct alignment of the quarterwave loop ($\Delta\theta = 0°$), the detected intensity in presence of a retardation error ΔR is given by Eq. (5.2.14), where $|\gamma(2\tau)| = 0$ for the low coherence source. For small Faraday effect ($4\varphi_F < 0.1$ rad) the detected voltage is

$$U(t) = U_0\{1 + [1 - 2\sin^2(\Delta R/2)]4\varphi_F(t)\} = U_0[1 + 4VNI(t)\cos\Delta R], \qquad (5.6.5)$$

where U_0 is the dc component of the detected voltage. The ac component is then given by

$$U_{ac}(t) = U_0 4VNI(t)\cos\Delta R = U_0'(t)\cos\Delta R\ . \qquad (5.6.6)$$

The relative rms Faraday signal U_{ac}/U_0' has been measured for different values of the retardation error ΔR and for a constant current of I = 20 A ($\varphi_F \approx 6$ mrad), the results are reported in Fig. 5.15 together with the theoretical prediction obtained from Eq. (5.6.6). This confirms the good agreement between the theoretical model and the measurements. The error for the determination of ΔR is ±5°, as already explained in Section 5.6.1. One sees that a retardation error of the quarterwave loop results in a reduction of the sensitivity to the Faraday effect. This decrease in sensitivity is not really a problem by itself, however, if ΔR changes with temperature undesirable drift of the sensitivity occurs. Therefore ΔR has to be as small as possible in order to get a Faraday signal which is nearly temperature independent.

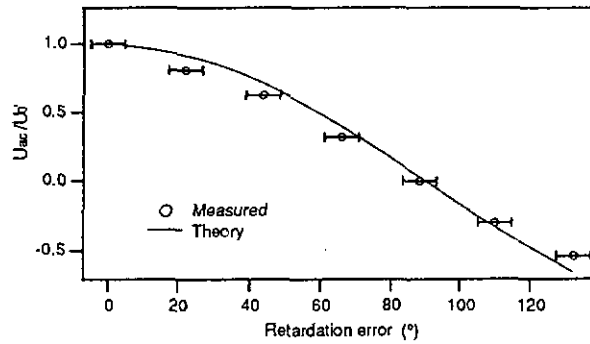

Figure 5.15 Measured relative ac voltage U_{ac}/U_0' versus loop retardation error ΔR.

Effects of non-ideal alignment of the quarterwave loop

Assuming no retardation error ($\Delta R = 0°$), the detected intensity in presence of an alignment error $\Delta\theta$ is given by Eq. (5.2.20), where $|\gamma(2\tau)| = 0$ for the low coherence source. For small Faraday effect ($4\varphi_F < 0.1$ rad) the detected voltage is

$$U(t) = U_0\{1 + [1 - 2\sin^2(\Delta\theta)]4\varphi_F(t)\} = U_0[1 + 4VNI(t)\cos 2\Delta\theta] , \qquad (5.6.7)$$

where U_0 is the dc component of the detected voltage. The ac component is then given by

$$U_{ac}(t) = U_0 4VNI(t)\cos 2\Delta\theta = U_0'(t)\cos 2\Delta\theta . \qquad (5.6.8)$$

The relative rms Faraday signal U_{ac}/U_0' has been measured for different values of the alignment error $\Delta\theta$ and for a constant current of I = 20 A ($\varphi_F \approx 6$ mrad). The results are reported in Fig. 5.16 together with the theoretical prediction obtained from Eq. (5.6.8). This confirms the good agreement between the theoretical model and the measurements.

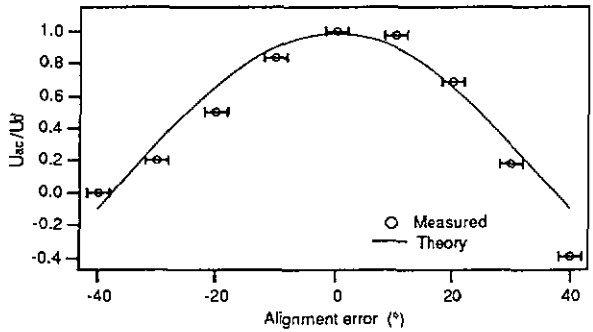

Figure 5.16 Measured relative ac voltage U_{ac}/U_0' versus loop alignment error $\Delta\theta$.

The error for the determination of $\Delta\theta$ is $\pm 2°$ as already explained in Section 5.6.1. One sees that an alignment error of the quarterwave loop results also in a reduction of the sensitivity to the Faraday effect.

Effects of the polarization cross-coupling

As already explained in Section 3.2.2, perturbing interference due to cross-coupled light is eliminated for a low coherence source. To prove this fact experimentally one can apply the same procedure as for the case whith a coherent source. For different values of the retardation error ΔR and of the alignment error $\Delta\theta$, one perturbs the hi-bi fiber by heating it in order to produce changes of the time delay difference τ. The measurements showed clearly that the detected voltage does not change when the hi-bi fiber is heated. Therefore, a low coherence source makes the reciprocal reflection interferometer practically useful.

5.7. Experimental investigations of the non-reciprocally phase modulated reflection interferometer

As already point out in Section 3.2.2, the coupler in the reflection interferometer produces an unwanted phase shift which perturbs the Faraday phase measurement. This can be avoided if the interference between the two orthogonal output modes takes place before the coupler by inserting a linear polarizer as shown in Fig. 3.7. As a consequence, a non-reciprocal phase modulation becomes necessary in order to get optimum sensitivity to the Faraday effect. In this section, the principle of the internal non-reciprocal phase modulation is experimentally demonstrated and applied to measure the Faraday effect.

5.7.1. Experimental set-up and signal processing

In this experiment the same low coherence source as in Section 5.6.2 was used. The experimental set-up is shown in Fig. 5.17.

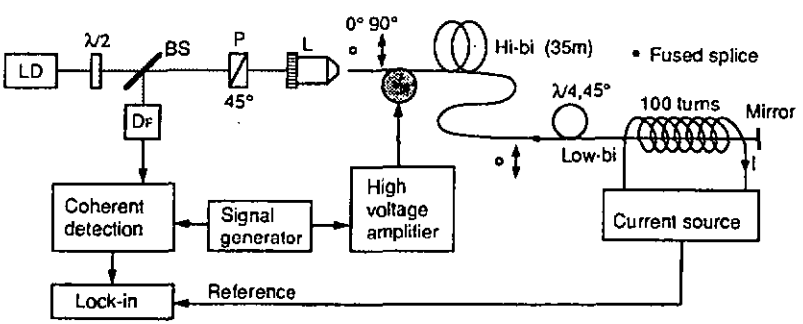

Figure 5.17 Experimental set-up. LD: multimode laser-diode ($\lambda = 780$ nm, $\Delta\lambda = 3$ nm), P: Glan-Thomson polarizers, BS: beam splitter cube, D_F: silicon photodiode detector, L: low-bi microscope objective, I: electrical current.

In the previous section the spectrum of the multimode laser source was monitored during the measurements. It was observed that the spectrum of the source remained stable, therefore it was no longer necessary to monitor it. The all-fiber phase modulator consists of 20 turns of hi-bi fiber wound around a piezoceramic (PZT) cylinder of 32 mm diameter. The other optical elements in the interferometer are the same as in Section 5.6.2.

Assuming that the orientations of the different polarizing elements are correct, we are nearly in the ideal case described in Section 5.3.2. Therefore the detected signal is given by Eq. (5.3.14). The Faraday phase is recovered using coherent detection. The principle of the signal processing is described in detail in Section 4.6.2. After coherent detection the output signal is expressed by Eq. (4.6.7), that is

$$U(t) = U_0 J_1(\Delta\phi_0)\sin\varphi(t), \tag{5.7.1}$$

where the non-reciprocal phase $\varphi(t)$ is now

$$\varphi(t) = 4\varphi_F(t) = 4VNI(t)\,. \tag{5.7.2}$$

For small values of the Faraday effect ($\varphi(t) \leq 0.1$ rad, i.e. $I \leq 170$ A for a 100 turn current coil and $\lambda = 780$ nm) one can assume that $\sin\varphi(t) \approx \varphi(t)$. Like for the Sagnac interferometer, maximum sensitivity is obtained for $J_1(\Delta\phi_0) = \max$, i.e. for $\Delta\phi_0 \approx 1.8$ with $J_1(\Delta\phi_0) \approx 0.58$. Moreover, the sensitivity to fluctuations of $\Delta\phi_0 = 2\phi_0\sin(\omega_m T/2)$ vanishes if one works at the maximum of J_1, which provides immunity against fluctuations of ϕ_0, ω_m and T. For $\omega_m T/2 \approx \pi/2$ the required phase modulation ϕ_0 is minimum and the immunity of the demodulated signal against fluctuations of ω_m and T is even further improved. Using $T = n2L/c$ one gets for the optimum length of the hi-bi fiber

$$L = c/4nf_m. \tag{5.7.3}$$

In our experiment the modulation frequency imposed by the all-fiber modulator was $f_m = 845$ kHz. With $n = 1.5$ one gets from Eq. (5.7.3) $L = 59.2$ m for the optimum length. However, for practical reasons the fiber loop length was only 35 m, which yields $\sin(\omega_m T/2) \approx 0.8$. In the experiment the highest obtainable amplitude of the non-reciprocal phase modulation was $\Delta\phi_0 \approx 1$ rad. This non-optimum phase modulation resulted in a reduction of the signal to noise ratio of about 3 dB, which was acceptable for measurements.

5.7.2. Non-ideal elements and noise limitations

The effects of the non-ideal elements are essentially the same as for the Sagnac interferometer and are described in detail in Section 4.6.3. The principal difference is that in the Sagnac interferometer the cross-coupled light is principally eliminated by the linear output polarizer, whereas in the reflection interferometer it is eliminated thanks to the low coherence of the source. The effects of a non-ideal quarterwave loop have been experimentally investigated and are reported in Sections 5.7.4 and 5.7.5.

The detected signal is similar to the one obtained with the Sagnac interferometer, therefore the effects of the noise are also similar. A detailed description of these effects is given in Section 4.6.4.

5.7.3. Faraday affect measuremant

Figure 5.18 shows the measured demodulated signal (Faraday signal) versus the 75 Hz ac electrical current for a lock-in integration time of $T_i = 30$ ms, which corresponds to about 1 Hz detection bandwidth. The measured slope, or sensitivity, is $S_I \approx 0.0185$ mV/A. The detected optical power is approximately 6 μW. The signal to noise ratio is defined as the ratio of the detected electrical power at $2f_m$ and the electrical noise power at f_m (see Section 4.6.4). For 1 Hz detection bandwith the signal to noise ratio at the detector output is about 100 dB. The shot-noise limited detection condition was not achieved. The minimum detectable phase φ_{min} due to the detected noise is given by Eq. (4.6.14), namely $\varphi_{min} = [J_2(\Delta\phi_0)/J_1(\Delta\phi_0)]SNR^{-1/2}$. The amplitude of the non-reciprocal phase modulation is $\Delta\phi_0 \approx 1$ rad. The resulting minimum detectable phase is then $\varphi_{min} \approx 3$ μrad, which corresponds to a minimum detectable current of $I_{min} \approx 2.5$ mA for a 100 turn current coil and a Verdet constant of $V \approx 3$ μrad/A. The measured voltage noise at the demodulated output is about 0.3 μV/√Hz corresponding to a current noise of about 15 mA in 1 Hz detection bandwith, which is 6 times larger than the predicted value. This means that the demodulation stage introduces a certain amount of noise. This problem could be overcome by using improved electronics. The rms voltage error, after demodulation, is obtained from the linear fit to the measured values, namely $\delta U = \sigma_u\sqrt{1-r^2}$. This yields $\delta U \approx$ 3.7 μV, which corresponds to a rms current error of $\delta I \approx 0.2$ A. The expected error due to the measured noise is 13 times smaller than the actual error of 0.2 A. This is mainly due to fluctuations of the optical power, and to voltage and current reading errors.

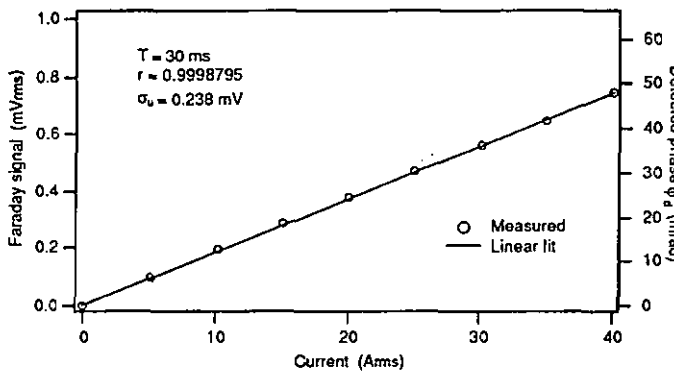

Figure 5.18 Demodulated voltage versus electrical current.

5.7.4. Effects of non-ideal quarterwave loop

The effects of the non-ideal retardation and the non-ideal alignment of the quarterwave loop have already been investigated out in Section 5.6.2. However, it is interesting to measure these effects with the modulated version of the reflection interferometer.

Effects of quarterwave loop retardation error

The coherent detection provides an output signal which is proportional to the amplitude of the component at the modulation frequency f_m. From Eq. (5.4.5) and assuming a small Faraday phase ($4\varphi_F < 0.1$ rad) one gets for the demodulated voltage

$$U(t) = U_0 4VNI(t)\cos\Delta R = U_0'(t)\cos\Delta R \,. \tag{5.7.4}$$

This expression is the same as the one obtained for the unmodulated reflection interferometer (see Eq.(5.6.6)). The relative signal U/U_0' has been measured using the same experimental conditions as in Section 5.6.2. The results are reported in Fig. 5.19 together with the theoretical prediction obtained from Eq. (5.7.4).

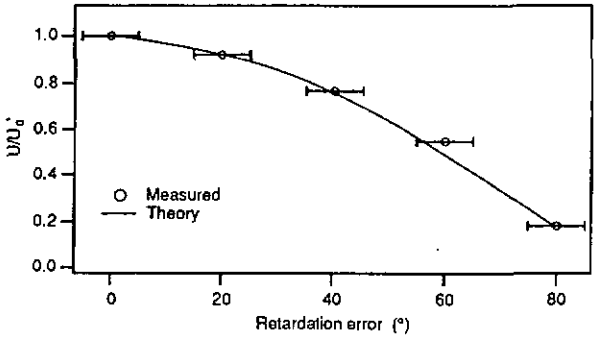

Figure 5.19 Relative demodulated voltage U/U_0' versus the loop retardation ΔR.

Here again one has a good agreement between the theoretical model and the measurements. The conclusions are the same as in Section 5.6.2.

Effects of non-ideal alignment of the quarterwave loop

Applying the previous procedure one gets for the demodulated voltage

$$U(t) = U_0 4VNI(t)\cos 2\Delta\theta = U_0'(t)\cos 2\Delta\theta \,. \tag{5.7.5}$$

This expression is the same as the one obtained for the unmodulated reflection interferometer (see Eq.(5.6.8)). The relative signal U/U_0' has been measured using the same experimental conditions as in Section 5.6.2. The results are reported in Fig. 5.20 together with the theoretical prediction obtained from Eq. (5.7.5).

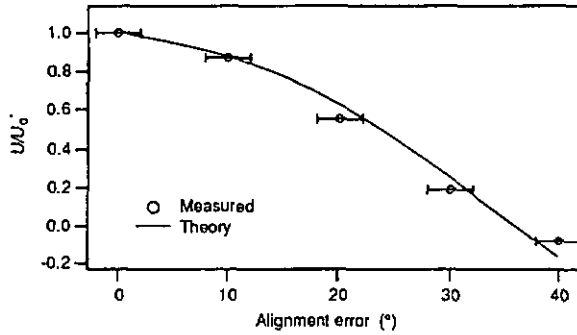

Figure 5.20 Relative demodulated voltage U/U_0' versus the misalignment error $\Delta\theta$.

The good agreement between the theoretical model and the measurements is confirmed and the conclusions are the same as in Section 5.6.2

5.7.5. Effects of the polarization cross-coupling

Like for the unmodulated case (see Section 5.6.2), no perturbing interference due to cross-coupled light will arise if a low coherence source is used. Applying the same procedure as for the case whith a coherent source, the measurements showed clearly that the detected voltage does not change when the hi-bi fiber is perturbed, confirming the theoretical previsions. Therefore, a low coherence source makes the modulated reciprocal reflection interferometer practically useful for industrial current sensors.

5.7.6. Effects of the temperature

Measurements of the temperature effects in the Sagnac interferometer have shown that problems arise due to technological reasons, such as glue points in the sensing coil etc. Therefore it was not worthwhile to proceed to new temperature measurements as long as these technological problems were not solved.

5.7.7. Conclusions

The principle of the fiber reflection interferometer using internal non-reciprocal modulation has been successfully demonstrated. The effects of non-ideal quarterwave loop have been experimentally investigated and show good agreement with the theoretical predictions. The principal effect of a quarterwave loop retardation error or misalignment error is a reduction of the sensitivity for the Faraday effect. The use of a low coherence source is necessary to get immunity to external perturbations acting on the hi-bi fiber which connects the sensor coil to the electronics at ground level.

6. COMPARISON OF THE SAGNAC INTERFEROMETER AND THE RECIPROCAL REFLECTION INTERFEROMETER

In this chapter the Sagnac current sensor (see Fig. 3.5) and the modulated reflection interferometer (see Fig. 3.7) are compared. Both are reciprocal and are therefore sensitive to the Faraday effect, whereas other polarization perturbing effects arising in the interferometer are eliminated to a large amount. One has to compare the two types of interferometer for the same sensitivity to the electrical current, therefore it is assumed that the sensing coil in the reflection interferometer has half the number of turns of the coil in the Sagnac interferometer. For this reason the theoretical investigations have been performed with N = 20 number of turns for the Sagnac interferometer (see Chapter 4) and N = 10 for the reflection interferometer (see Chapter 5).

6.1. Principal characteristics

The principal characteristics of the Sagnac and the reflection configuration are compared in Table 6.1. These two configurations provide the same modulated detector signals, therefore the same signal processing can be used for both configurations.

	SAGNAC TYPE	REFLECTION TYPE
Detected phase	$\varphi_d = 2\varphi_F = 2VNI$	$\varphi_d = 4\varphi_F = 4VNI$
Number of turns of the sensing coil for the same sensitivity	N = 20	N = 10
Number of $\lambda/4$ loops	2	1
Coupler type	polarization maintaining	no special requirement (polarization maintaining is better)
Principle of the non-reciprocal modulation	optical phase modulation	retardation modulation
Minimum number of splices (pigtailed source)	10	5
Hi-bi fiber length for the same modulation frequency (1 MHz)	100 m	50 m

Table 6.1 Principal characteristics of the Sagnac and the reflection type interferometer.

Table 6.1 shows that for similar performances the reflection configuration requires half the number of splices, half the length of low-bi and hi-bi fiber, and only one quarterwave loop. Therefore, the manufacturing is simpler for the reflection configuration than for the Sagnac configuration. The smaller number of splices and elements in the interferometric part reduces also the risk of errors due to non-ideal elements and alignments. Therefore, the cost for the current sensor using the reflection configuration is likely to be lower than for the Sagnac version. On the other hand, the Sagnac configuration has the advantage that the essential parts are commercially available. It is possible to have on a single integrated optic chip the polarizer, the loop coupler and the phase modulator. With the reflection configuration, the coupler and the polarizer can also be integrated on the same chip, but, the birefringent modulator has to be oriented at 45 ° with respect to the polarizer. It is therefore not possible, or very difficult, to integrate it on the same chip together with the coupler and the polarizer. If an integrated optic birefringence modulator is used, an additional splice is required. The use of a piezoelectric stretcher permits to have an all-fiber birefringence modulator without cutting the hi-bi fiber. However, it is difficult to modulate efficiently the PZT element at a resonance frequency of 1 MHz. A high voltage driving is required to obtain an efficient birefringence modulation. It is always possible to increase the length of the hi-bi fiber in order to decrease the optimum modulation frequency. However, this means that the advantage of the shorter hi-bi fiber in the reflection configuration is lost.

6.2. Effects of non-ideal elements and temperature

These effects have been theoretically analyzed in the previous chapters. For most of these effects the resulting error is lower than 0.1 ‰. It was therefore not possible to measure them for an experimental comparison of the two configurations. The only effects giving rise to detectable errors are the temperature dependence of the quarterwave loops. These effects were smaller than the ones due to the temperature behavior of the sensing coil (due to technological problems at the time being) and it was therefore not possible to make comparative measurements between the two configurations. Therefore, the following analysis is essentially based on the theoretical results.

The error due to the non-ideal sensing coil, e.g. bent and twist fiber, are the same for both configurations, as shown in Figs. 4.4 and 5.3. For a twisted rate of 10 turns/m and a coil diameter of 345 mm this error amounts to about 3 ppm for a current of about 10 kA, which is negligible for current sensor applications.

For the Sagnac configuration with a 345 mm diameter coil using 20 turns of a twisted fiber with 10 turns/m the effects of the temperature due to the sensing coil give rise to an error which oscillates between 0 ppm and 30 ppm (see Fig. 4.5) in the temperature range of –40 °C to 80 °C. Under the same conditions, but with a 10 turn coil, the error for the reflection configuration oscillates between –30 ppm and +30 ppm (see Fig. 5.4). Though these errors are negligible for current sensing applications, it appears that the Sagnac configuration is by a factor of two less sensitive to temperature changes of the sensing coil than the reflection configuration.

The effects of non-ideal quarterwave loops are similar for both configurations. A retardation error of 1° or an alignment error of 1° give rise to a phase error of 0.61 %. This is acceptable for most current sensing applications.

The temperature dependence in the range of –40 C° to +80 C° of the quarterwave loop with 90° retardation results in an error of about 1.2 ‰ for both configurations. For the Sagnac configuration retardation errors of 2° are acceptable, if they are symmetrically distributed, e.g. one loop 88° (or 92°) and the other 92° (or 88°). The reflection configuration is more sensitive to retardation errors of the quarterwave loop; for example an error of 1° gives rise to a detected phase error of about 2.2 ‰ in the temperature range of –40 °C to 80 °C (see Fig. 5.5). This could be a problem for high precision current sensor applications.

7. CONCLUSIONS

In this work, Sagnac and reciprocal reflection interferometers for the detection of the Faraday effect have been theoretically and experimentally investigated. The principal goal of this research was to compare this two reciprocal configurations in order to point out their fundamental properties for the detection of the Faraday effect.

The fiber optic Sagnac interferometer is well known for its application as a gyroscope. It is only sensitive to non-reciprocal effects, such as the Sagnac effect or the Faraday effect. Therefore it is a good candidate for current sensing applications. This idea was already successfully applied by several authors [Fer82, Lei86, Don88, Nic88]. In this work, the Sagnac current sensor was obtained by modifying the minimum reciprocal configuration of the fiber gyroscope in order to be sensitive to the Faraday effect. For this purpose, two quarterwave loops are inserted to obtain circular polarizations in the sensing coil from the linear polarizations of the hi-bi fiber in the rest of the Sagnac interferometer. This is necessary to get optimum interferometric detection of the Faraday effect. A fiber sensing coil exhibiting very low linear birefringence is connected between the two loops. The design and the interpretation of the results requires a thorough understanding of the different polarization phenomena arising in the interferometer. For this purpose a theoretical model, based on the Jones calculus, has been developed. This model provides an efficient tool to simulate and to understand the non-trivial behavior of the modified Sagnac interferometer. The effects caused by the non-ideal elements in the interferometer have been theoretically and experimentally investigated. It appears that the developed theory and the experimental results are in good agreement.

An all-fiber Sagnac current sensor has been realized and successfully tested. Fiber optic elements, such as all-fiber quarterwave loops, all-fiber polarizers, polarization maintaining fiber couplers and pigtailed laser sources, have been used. The sensing coil had the form of a helix around the electrical conductor. This helical coil had been used previously in a fiber optic current sensor working in transmission and using heterodyne detection. The geometrical torsion of the helix provides an elegant way to compensate the perturbing effects of the bend-induced linear birefringence.

An other all-fiber Sagnac current sensor based on a commercial fiber optic gyroscope has been realized and tested. The 100 m long fiber of the gyroscope was cut in the middle of its length and then spliced to the quarterwave loops. A 20 turn fiber coil with a diameter of $2R = 345$ mm was used. The ultra-low birefringence fiber, which has a diameter of $2r = 80$ µm, was mechanically twisted at the rate of 10 turns/m. Perfect linearity between the detected Faraday phase shift and the 75 Hz ac current was measured from 10 A to 800 A. The detected phase noise amounts to about 10 µrad/$\sqrt{\text{Hz}}$, which is equivalent to a detected current noise of 0.1 A/$\sqrt{\text{Hz}}$. Very good stability and temperature behavior have been obtained. Some problems remain at low temperatures ($\leq 0°$ C) due to technological problems in the realization of the sensing coil. This "gyro-current sensor" shows how the development of fiber optic current sensors can benefit from the well established fiber optic gyroscope technology.

To the best of our knowledge, it is for the first time in this work that a truly reciprocal reflection interferometer is reported. This interferometer looks like one half of a Sagnac interferometer.

The reflection interferometer uses two co-propagating orthogonal modes which are reflected at the end of the fiber sensing coil, rather than two counter-propagating modes of the same polarization, as in the case of the Sagnac interferometer. The sensing coil is connected to the ground level by a polarization maintaining hi-bi fiber. Between the sensing coil and the hi-bi fiber a quarterwave loop transforms the two orthogonal linear polarizations into orthogonal circular polarizations and vice-versa. The combination of the hi-bi fiber, the quarterwave loop and the mirror results in a perfectly balanced reciprocal interferometer. After a total round trip in the interferometer the only phase shift between the two polarizations is caused by the Faraday effect. The reflected light is detected at the output arm of a fiber coupler. The effects of polarization cross-coupling due to non-ideal elements, such as the sensing coil, the quarterwave loop, the hi-bi fiber, etc, are eliminated by using a low coherence source. Non-reciprocal phase modulation is necessary to get optimum detection of the Faraday phase shift. This non-reciprocal modulation is performed by an all-fiber birefringent modulator. Like for the fiber gyroscope, efficient non-reciprocal modulation is obtained for a modulation frequency equal to 2/T, where T is the time of flight for a total round trip. To be independent of the polarization properties of the coupler, the two reflected orthogonal modes are made to interfere before this coupler. This is achieved by inserting a linear polarizer between the coupler and the modulator.

Like for the Sagnac configuration, a theoretical model based on the Jones calculus and taking into account the coherence of the light, has been developed. This model has been used to evaluate the effects of non-ideal elements and of the temperature. Here again, theoretical and experimental results are in good agreement.

A first reflection interferometer without non-reciprocal modulation has been realized. Optimum sensitivity to the Faraday effect was obtained by introducing a 90° phase shift between the two linear input polarizations, using a quarterwave plate. Two different laser sources have been used with this interferometer. The first source was a single-mode laser diode, delivering highly coherent light. With this source, the perturbing effects of coherent polarization cross-coupling have been experimentally verified. The measurements are in good agreement with the theory. The second source was a multimode laser diode exhibiting a coherence length of about 200 μm. With this low coherence source it was shown experimentally that the perturbations due to polarization cross-coupling are eliminated. Good agreement with the theory is obtained. The sensing element was formed of a piece of straight fiber of ultra-low birefringence type. The magnetic field was produced by a 100 turn solenoid. Perfect linearity between the detected Faraday phase shift and the 75 Hz ac current was measured from 0 A to 40 A. The detected current noise amounts to about 0.02 A/$\sqrt{\text{Hz}}$. These theoretical and experimental investigations confirmed the necessity to use a low coherence source in order to get good signal stability with the reflection configuration.

The purpose of the second reflection interferometer was to experimentally demonstrate the principle of the non-reciprocal modulation. A low coherence laser diode was used. The phase modulation was obtained by winding the hi-bi fiber around a piezo-ceramic cylinder. The sensing element was again a straight fiber. The Faraday effect has successfully been measured using coherent detection. Perfect linearity between the detected Faraday phase shift and the 75 Hz ac current was measured from 0 A to 40 A. The detected current noise amounts to about 0.015 A/$\sqrt{\text{Hz}}$. Effects of non-ideal elements in the interferometer have also been measured and are in good agreement with the theory. Here again, good signal stability was achieved thanks to the low coherence of the source.

From the comparison between the Sagnac and the reflection configuration it appears that, for similar performance, the second needs less fiber optic elements and half the number of splices. This is an important advantage for the industrial production of current sensors. The modulated detector signals are identical for the Sagnac and the reflection configuration. This permit to use the same electronic signal processing for both configurations. The effects of non-ideal elements are similar for both configurations. However, the temperature effects due to the quarterwave loop are more critical for the reflection configuration than for the Sagnac interferometer.

To conclude, the possibility to use the Sagnac and the reciprocal reflection configurations for current sensing has been successfully demonstrated, and their basic properties and limitations are completely understood from the theoretical point of view.

ACKNOWLEDGMENTS

I would like to express my gratitude to Prof. R. Dändliker, director of this thesis. His commitment to this work and his encouragement have been of invaluable help to me.

Special thanks go also to Dr. H. Brändle, Prof. Ph. Robert and Prof. N. De Rooij for the interest they expressed in critically reviewing my thesis as members of the jury.

Furthermore, I wish also to thank MM. K. Hug and C. Berthoud for their experimental help, Dr. J. Nehring and J. Morel for many useful discussions and my brother R. Frosio for his helpful corrections of my English.

Finally, I would like to thank all my family, my colleagues, the technical assistants and the secretarial staff of the Institut de Microtechnique, who made it possible to realize this work in a pleasant atmosphere.

Part of this research was performed in close collaboration with the Research Center of ABB, at Baden-Dättwil. The research project was supported by the CERS (Commission pour l'encouragement de la recherche scientifique).

REFERENCES

[Ann87] V. Annovazzi-Lodi, S. Donati, "Fiber current sensors for HV-lines", SPIE Vol. 798 Fiber optic sensor II), 270-274 (1987.

[Azz77] R. M. A. Azzam, "Elipsometry and polarized light", North-Holland, Amsterdam 1977.

[Bar81] A. Barlow et al., "Birefringence and polarization mode-dispersion in spun single mode fibers", Appl. Opt. 20, 2962-2968 (1981).

[Bar85] A. J. Barlow, "Optical-fiber birefringence measurement using a photo-elastic modulator", J. Lightwave Technol., LT-3, 135 (1985).

[Bir88] T. A. Birks, P. Morkel, "Jones calculus analysis of single-mode fiber Sagnac reflector", Appl. Opt. 15, 3107-3113 (1988).

[Bor59] M. Born & E. Wolf, "Principles of Optics", Pergamon Press, Oxford 1959.

[Bus89] S. P. Bush, D. L. Mazzoni, K. Cho, C. C. Davis, "A fiber optic heterodyne sensor for linear birefringence or polarization rotation effects", LEOS '89 Proceedings, Orlando, 89CH2641-9, (1989) 267.

[Dän92] R. Dändliker, "Rotational effects of polarization in optical fibers", in Anisotropic and nonlinear optical waveguides (Ed.: G. Stegemann and C. Someda, Elsevier, Amsterdam, 1992).

[Don88] S. Donati, V. Annovazzi-Lodi, T. Tambasso, "Magneto-optical fiber sensor for electrical industry: analysis of performance", IEE Proceedings 135 , 372 (1988).

[Eze82] S. Ezekiel, "Fiber-Optic Rotation Sensors. Tutorial Review", in Fiber-Optic Rotation Sensors (Ed.: S. Ezekiel and H. J. Arditty, Springer Verlag, Berlin, 1982), 2-26.

[Fer82] P. Ferdinand, J.-L. Lesne, "Induced Circular Birefringence and Ellipticity Measurement in a Faraday Effect Fiber Ring Interferometer", in Fiber-OpticRotation Sensors (Ed.: S. Ezekiel and H. J. Arditty, Springer Verlag, Berlin, 1982), 2-26.

[Fro89] G. Frosio, "All-fiber adjustable retardation plate", EFOC Proceedings, Amsterdam (IGI Europe a Division of Information Gatekeepers, Boston, USA), 350-355 (1989).

[Fro92] G. Frosio, "All-fiber Sagnac current sensor", Opto 92 Proceedings, Paris, 560-564 (1992).

[Gia82] T. G. Giallorenzi et al., "Optical fiber sensor technology", J. Quantum E. **QE-17**, 626-665 (1982).

[Hay82] S. Haykin, "Amplitude Modulation Systems", in Communication Sytems (John Wiley&Sons, 1982), chapter 3.

[Jon41] R. C. Jones, "A new calculus for the treatment of optical systems. I. Description and discussion of the calculus", J. Opt. Soc. Am. **31**, 488-493 (1941).

[Kam81] I. P. Kaminow, "Polarization in optical fibers", J. Quantum El. **QE-17**, 15-22 (1981).

[Kam82] I. P. Kaminow, "Polarization-maintaining fibers", in Fiber-Optic Rotation Sensors (Ed.: S. Ezekiel and H. J. Arditty, Springer Verlag, Berlin, 1982), 169-177.

[Ker86] A. D. Kersey, D. A. Jackson, "Current sensing utilizing heterodyne detection of the Faraday effect in single-mode optical fiber", J. Lightwave techn., LT-34, 640-643 (1986).

[Ker89] A. D. Kersey, M. A. Davis, " All-fiber Faraday-rotation current sensor with remote laser-FM based heterodyne detection", in Optical fiber sensors (Ed.: H. J. Arditty, J. P. Dakin, R. Th. Kersten, Springer -Verlag Berlin, Heidelberg 1989), 285-290.

[Lei86] P. A. Leilabady, A. P. Wayte, M. Berwick, J. D. C. Jones and D. A. Jackson, "A pseudo-reciprocal fiber-optic Faraday rotation sensor: current measurement and data communication applications", Optics commun., 59, 173-176 (1986).

[Li87] L. Li, J. Qian, D. N. Payne, "Miniature multi-turn fiber current sensor", J. Opt. Sensors, 2, 25-33 (1987).

[May89] F. Maystre and A. Bertholds, "Magneto-optic Current-Sensor Using a Helical-Fiber Fabry-Perot Resonnator", Optics Lett. **14**, 587-589 (1989).

[Nic88] P.-A. Nicatti et al.,"Stabilized current sensor using Sagnac interferometer", J. Phys. E. **21**, 791-796 (1988).

[Pal85] E. D. Palik (ed.), "Handbook of optical constants", (Academic Press,1985).

[Pap80] A. Papp, H. Harms, "Magneto-optical current transformers", Appl. Opt. 19, 3729-3745 (1988).

[Ras79] S. C. Rashleigh, R. Ulrich, "Magneto-optic current sensing with birefringent fibers", Appl. Phys. Lett. 34, 768-770 (1979).

[Ren88] Z. B. Ren, Ph.-A. Robert, P.-A. Paratte, "Temperature dependence of bend- and twist-induced birefringence in a low birefringence fiber", Optics Lett. 13, 62-64 (1988).

[Ren89] Z. B. Ren, Y. Wang, Ph-A. Robert, "Faraday rotation and its temperature dependence measurements in low-birefringence fiber", J. Lightwave Technol., LT-7, 1275-1278 (1989).

[Ros65] B. Rossi, "Optics", (Addison-Wesley Co., 1965).

[Ros84] J. Ross, "The rotation of the polarization in low birefringence monomode optical fibers due to geometric effects", Optical and Quantum Electr. 16, 455-461 (1984).

[Smi78] A. M. Smith, "Polarization and magneto-optic properties of single mode optical fiber", Appl. Opt. 17, 52-57 (1978).

[Ulr79] R. Ulrich, A. Simon, "Polarization optics of twisted single-mode fibers", Appl. Opt. 18, 2241-2251 (1979).

[Ulr80] R. Ulrich, S. C. Rashleigh, and W. Eickhoff, "Bending induced birefringence in single-mode fibers", Opt. Lett. 5, 273 (1980).

[Ulr82] R. Ulrich, "Polarization and depolarization in the fiber optic gyroscope", in Fiber-Optic Rotation Sensors (Ed.: S. Ezekiel and H. J. Arditty, Springer Verlag, Berlin, 1982), 52-77.

[Var83] M. P. Varnham, A. J. Barlow, D. N. Payne, K. Okamoto, "Polarimetric strain gauges using high birefringence fibre", Electronics Lett. 19, 699-700 (1983).

[Voi08] W. Voigt, "Magneto-und Electro-Optik", (Teubner Publishing, Leipzig 1908).